

2015

Beam-plasma interactions and Langmuir turbulence in the auroral ionosphere

<https://hdl.handle.net/2144/16310>

Boston University

BOSTON UNIVERSITY
COLLEGE OF ENGINEERING

Dissertation

**BEAM-PLASMA INTERACTIONS AND LANGMUIR TURBULENCE
IN THE AURORAL IONOSPHERE**

by

HASSANALI AKBARI

B.S., University of Tehran, 2009
M.S., Boston University, 2013

Submitted in partial fulfilment of the
requirement for the degree of
Doctor of Philosophy

2015

Approved by

First Reader

Joshua L. Semeter, PhD
Professor of Electrical and Computer Engineering

Second Reader

Meers M. Oppenheim, PhD
Professor of Astronomy

Third Reader

Min-Chang Lee, PhD
Professor of Electrical and Computer Engineering

Fourth Reader

P. Robert Kotiuga, PhD
Associate Professor of Electrical and Computer Engineering

Acknowledgments

Several people need to be thanked for their contributions to this thesis. I need to acknowledge my advisor, Prof. Semeter, who provided me with amazing research opportunities and greatly contributed to my personal growth. I would like to thank Prof. Oppenheim and Prof. Lee for their valuable discussions and Prof. Kotiuga for serving on my defense committee. I would like to thank Dr. Nicolls at SRI International for his help with the experimental results from the Poker Flat incoherent scatter radar; and Dr. Guio for his help with the simulation results.

My thanks are not complete without acknowledging the love and support of my parents, Ebrahim and Maliheh Akbari, to whom I dedicate this work.

**BEAM-PLASMA INTERACTIONS AND LANGMUIR TURBULENCE
IN THE AURORAL IONOSPHERE**

HASSANALI AKBARI

Boston University, College of Engineering, 2015

Major Professor: Joshua L. Semeter, PhD, Professor of Electrical and Computer Engineering

ABSTRACT

Incoherent scatter radar (ISR) measurements were used in conjunction with plasma simulations to study two micro-scale plasma processes that commonly occur in the auroral ionosphere. These are 1) ion acoustic turbulence and 2) Langmuir turbulence.

Through an ISR experiment we investigated the dependence of ion acoustic turbulence on magnetic aspect angle. The results showed a very strong aspect angle sensitivity which could be utilized to classify the turbulence according to allowable generation mechanisms and sources of free energy.

In addition, this work presents results that led to the discovery of a new type of ISR echo, explained as a signature of cavitating Langmuir turbulence. A number of incoherent scatter radar experiments, exploiting a variety of beam and pulse patterns, were designed or revisited to investigate the Langmuir turbulence underlying the radar echoes. The experimental results revealed that Langmuir turbulence is a common feature of the auroral ionosphere. The experimental efforts also led to uncovering a relationship between Langmuir turbulence and one type of natural electromagnetic emission that is

sometimes detected on the ground, so-called “medium frequency burst”, providing an explanation for the generation mechanism of these emissions.

In an attempt to gain insights into the source mechanism underlying Langmuir turbulence, 1-dimensional Zakharov simulations were employed to study the interactions of ionospheric electron beams with a broad range of parameters with the background plasma at the F region peak. A variety of processes were observed, ranging from a cascade of parametric decays, to formation of stationary wave packets and density cavities in the condensate region, and to direct nucleation and collapse at the initial stage of the turbulence.

The simulation results were then compared with the ISR measurements where inconsistencies were found in the spectral details and intensity of the simulated and measured Langmuir turbulence echoes, suggesting the possibility that the direct energy for the turbulence was provided by unstable low-energy (5 – 20 eV) electron populations produced locally in the F region of the ionosphere rather than by electron beams originating from the magnetosphere.

Contents

1	Introduction	1
1.1	Main Contributions of this Thesis	3
1.2	Terminology	5
1.3	Thesis Organization	8
2	Background	11
2.1	The Earth's Plasma Environment	11
2.1.1	The Ionosphere	11
2.1.2	The Magnetosphere	14
2.2	Plasma Waves and Instabilities	16
2.2.1	General Treatment of a Warm Plasma	17
2.2.2	Ion Acoustic Waves and Langmuir Waves	22
2.3	Incoherent Scatter Radar (ISR) Technique	25
2.3.1	The Physics of Incoherent Scattering	25
1.	Scattering by Electrons	25
2.	The Concept of Bragg Scattering	32
3.	Ion Line Spectrum	37
2.3.2	Incoherent Scatter Radar Signal Processing	40
1.	Range-Time Diagram	40
2.	Autocorrelation Function	45
3.	Phased-Array ISRs and Pulse Coding Techniques	51

2.4 Naturally Enhanced Ion Acoustic Lines (NEIALs)	55
2.5 Beam-Plasma Interactions and Langmuir Turbulence	61
2.5.1 Beam-Plasma Interactions	61
2.5.2 Langmuir Turbulence	69
2.6 Ionospheric Modification Experiments	75
3 Naturally Enhanced Ion Acoustic Lines	76
3.1 Experimental Results	78
3.2 Discussions	90
3.3 Summary and Conclusions	94
4 Langmuir Turbulence: Experimental Results	96
4.1 March 23, 2007 Experiment: Cavitating Langmuir Turbulence in the Auroral Ionosphere	96
4.2 March 23, 2007 Experiment: Discussions	102
4.3 Further Experimental Results on ISR echoes	105
1. Echoes on the Edge of E region Ionization Enhancements	105
2. Simultaneous Enhancements in the Ion Line and the Plasma Line Channels	107
3. Localization of the Echoes in Thin Layers	107
4. Correlation of the Radar Echoes with Natural Electromagnetic Emissions	108
5. Asymmetric Plasma Line Spectra: Evidence for Existence of other Wave Modes	112

4.4 Propagation Effects on Saturation of Langmuir Waves	115
5 Langmuir Turbulence: Zakharov Simulations	123
5.1 Zakharov Equations	124
5.2 Simulation Results	129
5.2.1 Dynamics of Langmuir Turbulence	129
1. Simulation One: $\frac{n_b}{n_0} = 30 \times 10^{-7}$ and $E_b = 125 \text{ eV}$	130
2. Simulation Two: $\frac{n_b}{n_0} = 60 \times 10^{-7}$ and $E_b = 125 \text{ eV}$	138
3. Simulation Three: $\frac{n_b}{n_0} = 150 \times 10^{-7}$ and $E_b = 500 \text{ eV}$	140
4. Summary and Conclusions of Section 5.2.1	149
5.2.2 Suprathermal Electrons as the Source for the ISR Echoes	151
1. Ion Line Spectra: ISR Measurements	152
2. Ion Line Spectra: Simulations and Comparison with Measurements	154
3. Summary and Conclusions of Section 5.2.2	159
6 Summary, Conclusions, and Future Directions	161
6.1 Summary and Conclusions	161
6.2 Future Directions	163
References	166
Curriculum Vitae	180

List of Figures

2.1	Density profile of the electron and the main ion and neutral species composing the ionosphere.	13
2.2	Schematic of the earth's magnetosphere	15
2.3	The earth's auroral region. Aurora predominantly originates from the E and the F regions of the high-latitude ionosphere	17
2.4	Scattering from a single electron	26
2.5	Scattering from a population of electrons	29
2.6	The top panel shows the incoherent scatter spectrum which consists of the ion line and the plasma lines. The bottom panel zooms in the ion line, where the superposition of the two ion acoustic shoulders appears in the form of a single double-humped shape. The frequency axis is the offset frequency relative to the radar transmitting frequency	31
2.7	Bragg scattering by a periodic structure consisting of weakly reflective planes	33
2.8	Dependence of the shape of the ion line spectrum on the plasma parameters	38
2.9	Poker Flat incoherent scatter radar (PFISR) located in Fair Banks, Alaska	40
2.10	Range-time diagram of ISRs	41
2.11	Range-time diagram of ISRs.	43
2.12	Range-time diagram of ISRs	44
2.13	Range-time diagram of ISRs: averaging over many radar pulses	48
2.14	An example of the ion line spectra as a function of altitude measured by an ISR	49
2.15	An example of the range-time-intensity plot measured by an ISR. The enhanced signal below 200 km represents enhanced E region ionization due to energetic (keV) electron precipitations.	50

2.16	An example of a volumetric image of the ionosphere using the phased-array PFISR. The plot shows the ion temperature as a function of the three spatial dimensions	52
2.17	A set of pulses that compose a four bit alternating code (AC)	54
2.18	An example of the range-time plot from the ion line channel measurements. The enhanced echoes from 100 (km) to 600 (km) are produced by destabilized ion acoustic waves and are called naturally enhanced ion acoustic lines (NEIALs)	56
2.19	The typical form of NEIALs in the frequency domain. Here the down-shifted shoulder, corresponding to the ion acoustic waves propagating away from the radar, is enhanced above the thermal level	57
2.20	An example of an unstable one-dimensional electron distribution function consisting of background thermal electrons and an electron beam. The positive slope of the distribution function leads to growth of plasma waves.	63
2.21	Quasilinear diffusion: simulation results from <i>Muschiatti</i> [1990] showing the evolution of an electron distribution function (top) and plasma wave intensity (bottom). Numbers on the curves are times (in milliseconds) after the start of the simulation. It can be seen that once the plasma waves grow to higher intensities they react back on the distribution function to flatten the positive slope and remove the source of free energy	64
2.22	An electron distribution function measured by instruments on board of a sounding rocket at altitude of ~ 250 (km). The distribution function consists of a plateau implying that the quasilinear diffusion has stabilized the distribution function at higher altitudes	65
2.23	Nonlinear wave-wave interactions have been proposed as a plausible mechanism that can stabilize electron beam distributions against the quasilinear diffusion	67
2.24	Three-wave coalescence of an ion acoustic wave (W_1) and a Langmuir wave (W_2) to produce a product Langmuir wave (W_3). The equations are the dispersion relations for the ion acoustic mode and the Langmuir mode	68
2.25	Five regimes of linear parametric instability for a monochromatic, plane Langmuir wave with the approximate boundaries derived for the plasma parameters considered in this work. These include. I: parametric decay instability; II: modulational instability; III: subsonic modulational instability; IV: supersonic modulational instability; and V: modified decay instability	71

2.26	Panels a, b, and c show a cascade of parametric decays from the wave number at which the energy has been injected by the electron beam to smaller wave numbers. Panel d represents features that do not follow the linear dispersion relations for the ion acoustic and Langmuir waves. These are signatures of highly nonlinear features (cavitons) that can be produced during the turbulence	73
3.1	PFISR beam positions overlain on one frame recorded by a narrow-field camera on 01 March 2011. The magnetic zenith beam is filled in, the separation between beams is one degree (after <i>Dahlgren et al.</i> [2013])	79
3.2	Sequential all sky camera samples showing auroral activity associated with a substorm poleward expansion on 01 March 2011. The nominal position of the PFISR beam cluster (Figure 3.1) is indicated in red	80
3.3	Range-time plot of received power in the ion line channel for three of the radar beams (see Figure 3.1) during a period when the substorm expansion crossed through the PFISR beams. Mentioned in parenthesis are angles with respect to the magnetic zenith beam	82
3.4	Line plots of relative occurrence of NEIALs during a 90-second period starting at 10:05:20 UT for all beams of the 01 March 2011 experiment. Mentioned in parenthesis are angles with respect to magnetic field line at 500 km	83
3.5	Samples of normalized PFISR power spectra corresponding to Figure 3.3, computed using only 5-second integration and 71 radar pulses. Panel a shows the pre-event thermal backscatter. The remaining panels exhibit various types of enhancements in the ion acoustic lines. The time stamps correspond to the start time of the integration	84
3.6	Radar beams configuration on top of one frame of an all sky camera (March 23, 2007 experiment). The magnetic zenith beam is filled-in	86
3.7	Similar to Figure 3.3, range-time plot of received power in ion line channel for five of the radar beams in Figure 3.6. Mentioned in parenthesis are angles with respect to the magnetic zenith beam. In the top panel, three bursts of coherent echoes are labeled (echo 3 refers to the whole enhanced received power extended from 100 to 600 km), which are tracked in subsequent panels. Echoes similar to echo 1 appear in all panels while echoes similar to echo 3 only appear in the top three panels	86
3.8	Ion line spectra computed from measurements within the first and third echoes in the top panel of Figure 3.7. In the right panel, the apparent shift of the spectrum toward negative frequencies corresponds to upward plasma velocity of ~ 660 m/s.	89

4.1	(a) Received radar power in the ion line channel for the magnetic zenith beam. Three intervals of coherent scatter are identified and numbered. (b) Vertical cuts from the power plot in Figure 4.1a. Blue: At a time during the scattering event 1. Red: During the thermal scattering interval between the event 1 and 2. (SNR values are not range corrected)	98
4.2	Representative narrow-field (11 degree diagonal field of view) images of dynamic auroral forms associated with (a) event 1, (b) event 2, and (c) event 3 in Figure 4.1a. White circles represent the location and approximated 3 dB beamwidth of the radar beam. Exact 3 dB beamwidth is not a circle. (Images taken from <i>Semeter et al.</i> [2008])	98
4.3	Ion line spectra computed from measurements within the (a) first, (b) second, and (c) third scattering events of Figure 4.1a. (SNR values are not range corrected)	100
4.4	Blue: Ion acoustic spectrum for scattering event 1 (averaged over the scattering layer). Red: Ion acoustic spectrum for the thermal scattering interval between event 1 and 2 (averaged between 200 km and 270 km)	100
4.5	(a and b) Down- and up-shifted plasma line measurements, respectively, from scatter events 1. (c) Blue and red: horizontal cuts from Figures 4.5a and 4.5b, respectively, averaged over 200-km and 250-km altitude; showing the presence of two peaks in the plasma line spectra. (Negative frequencies are folded on top of the positive frequencies.)	101
4.6	PFISR observations of anomalous ion line spectra from (a) naturally and (b) heater wave produced Langmuir turbulence. Figure 4.6a corresponds to the data shown in Figure 4.3a. Figure 4.6b was recorded during an active ionospheric modification experiment using the High Power Auroral Stimulation facility on 17 March 2007	104
4.7	Received radar power in the ion line channel as a function of altitude and time, showing occurrences of coherent scatters just outside of periods of E region ionization enhancement due to energetic (keV) electron precipitation (left, 20 February 2012; right, 27 January 2012)	106
4.8	(a) Ion line power profile from alternating codes, showing localization of the turbulence in two thin layers. (b) Ion line power spectrum corresponding to Figure 4.8a, integrated between 4.5 and 5.33 min (data from 5 April 2012)	108
4.9	(a) Ion line power profile: occurrence of the coherent scatter at 11:20:08 UT, 23 March 2007. (b) Spectrogram of natural electromagnetic emissions accompanying the auroral activity, recorded with the base antenna at Toolik Lake (plot taken	

	from <i>Bunch et al.</i> [2008]). The blue and the orange bars specify the time of the features in each panel	110
4.10	A sequence of all-sky camera images recorded from Fort Yukon, AK. The image sample times are indicated by vertical black lines in Figure 4.9a, and the PFISR location is indicated by a red circle in Figure 4.10	111
4.11	Similar to Figure 4.9: (a) ion line power profile and (b) spectrogram of natural electromagnetic emissions. For convenience the time interval of three coherent scatters are marked by orange bars in both panels. (Data from 5 April 2012)	112
4.12	Panel a: ion line range-time-intensity (RTI) plot derived from a separate one-baud-length pulse that accompanied AC. The time axis is shown in minutes as well as in 16-second intervals (records) starting at 6:04:35 (UT). Coherent echoes are originating from thin layers close to the F region peak (~250 (km)). Panel b: up- (blue) and down-shifted (red) plasma line spectra produced by long pulse measurements for record 16 in Panel a. The spectra are averaged over a 70-km range gate centered at 290 (km)	114
4.13	(a) Ion line power profile from the alternating codes, showing the localization of turbulence in two thin layers. (b) Background electron density profile averaged over the incoherent scatter measurement period marked by the blue bar in the left panel. Shaded area represents the statistical accuracy of the measurements (one standard deviation). The two horizontal bars show the location of the two layers with respect to the background density (Data from 17 March 2012)	118
4.14	Similar to Figure 4.13, (a) another example of the double-layer profile observed in the ion line channel, and (b) locations of the layers with respect to the background electron density (Data from 5 April 2012)	118
5.1	The left and right panels show the evolution of the electric field and the ion density perturbations, respectively, as a function of time and wave number for the beam parameters of $\frac{n_b}{n_0} = 30 \times 10^{-7}$ and $E_b = 125 \text{ eV}$ which has been applied at time $t = 0 \text{ ms}$	132
5.2	Normalized density fluctuations of Figure 5.1 in real space as a function of time. S_1 and S_2 are the ion acoustic waves produced by the first and the second PDI in Figure 5.1	133
5.3	The same data as shown in Figure 5.1 but for a broader range of wave numbers and intensities to illustrate the presence of the beam modulation and three-wave coalescence products	135

5.4	Averaged frequency behavior of the electric field and density perturbations in Figure 5.3. Products waves of the PDI, beam modulations, and the three-wave coalescence are observed	137
5.5	Similar to Figure 5.1, the left and right panels show the evolution of the electric field and the ion density perturbations, respectively, as a function of time and wave number for the beam parameters of $\frac{n_b}{n_0} = 60 \times 10^{-7}$ and $E_b = 125 \text{ eV}$ which has been applied at time $t = 0 \text{ ms}$	139
5.6	Normalized density fluctuations of Figure 5.5 in real space as a function of time: showing the formation of stationary density cavities following the transfer of energy to the condensate	140
5.7	The evolution of the turbulence in k space for electron beam parameters $\frac{n_b}{n_0} = 150 \times 10^{-7}$ and $E_b = 500 \text{ eV}$	141
5.8	Development of the turbulence (beam parameters $\frac{n_b}{n_0} = 90 \times 10^{-7}$ and $E_b = 500 \text{ eV}$) in the wave number-frequency domain. Top and bottom panels correspond to the electric field and density perturbations, respectively, for four consecutive periods of the turbulence. Dashed white curves are the theoretical dispersion curves for the Langmuir and ion-acoustic waves	142
5.9	Normalized density fluctuations of Figure 5.8 in real space as a function of time.	145
5.10	Normalized density fluctuations in real space as a function of time; showing the formation of cavitons through the cycle of nucleation-collapse-dissipation . . .	146
5.11	Normalized density fluctuations seen in Figure 5.9 in logarithmic scale	148
5.12	Evolution of the ratio of the electrostatic to thermal energy density (W) for the waves with the highest electrostatic energy for the simulation shown in Figures 5.7, 5.9, and 5.11	149
5.13	Examples of ion line spectra measured by the PFISR. Each spectrum, including those with different colors in panel c, corresponds to different times	153
5.14	Evolutions of the electric field magnitude (left) and ion density perturbations (right) as a function of time and wave number. The electron beam has been applied at time $t = 0 \text{ (ms)}$. White dashed lines show the PFISR detecting wave number	155

- 5.15 Panel a shows the averaged frequency behavior of density perturbations in Figure 5.14b once the quasi-steady state has been reached. Panel b is similar to panel a, but for a simulation run with a higher input energy to the system. Panel c, shows horizontal cuts through panel b at wave numbers 11, 19, and 38 (m^{-1}) (shown by white dashed lines in panels a and b), modeling the spectra that would be obtained if the turbulence was detected by the EISCAT VHF, PFISR, and the EISCAT UHF radars, respectively 158

List of Abbreviations

EISCAT	European incoherent scatter radar
ISR	incoherent scatter radar
MF Burst	medium frequency burst
MI	modulational instability
NEIAL	naturally enhanced ion acoustic line
PDI	parametric decay instability
PFISR	Poker Flat incoherent scatter radar
SNR	signal to noise ratio
UT	universal time
UV	ultraviolet

Chapter 1

Introduction

The ionosphere is a region of earth upper atmosphere that extends in altitude from 50 km to about 1000 km. The main characteristic of this region is that it is ionized by solar radiation. In other words, the ionosphere is a plasma; and as such can affect and be affected by electromagnetic waves. This property links the ionosphere to a wide range of applications, such as electromagnetic wave propagation around the earth and communication systems. In addition to the technological aspects, the ionosphere is host to a variety of complex processes many of which are fundamental topics in plasma physics. The ionosphere, and in general the plasma environment surrounding the earth, is, therefore, often regarded as an unbounded laboratory of plasma physics that deserves focused investigations.

A variety of methods have been employed to study ionospheric processes. These include in-situ measurements of fields, waves, and particles with instruments on board of rockets and satellites and ground-based remote sensing methods that utilize radars, LIDARs, and optical instruments. Incoherent scatter radars (ISRs) are the most powerful ground-based tools that have been developed to study the ionosphere. ISRs transmit electromagnetic pulses at VHF or UHF frequencies, i.e. at frequencies that are much higher than the maximum ionospheric plasma frequency, toward the ionosphere. A large portion of the transmitted electromagnetic energy penetrates through the ionosphere and is lost into space, however, a very small portion of the energy gets scattered off random fluctuations

of electrons in the plasma and returns to the radar site where it can be detected. The frequency spectrum of the scattered radiation, the ISR spectrum, is of great importance as it contains information on the bulk properties of the scattering plasma. This information is accessible once the measured ISR spectrum is fitted to a theoretical model via a nonlinear least square method. The outputs of the fitting process are estimates of the plasma parameters such as electron density, electron temperature, ion temperature, collision frequency, ion composition, and the line of sight ion flow velocity.

The theoretical models for the frequency spectrum of the scattered signal have been developed by many authors [*Fejer, 1960; Hagfors, 1961; Evans, 1965; Farley, 1996*]. Such models are often developed based on a set of assumptions on the state of the plasma. One of the most common assumptions is that the plasma is in thermal equilibrium consisting of electron and ion populations that can be described by Maxwellian distributions. Such assumptions, however, are commonly violated at high latitudes where interactions between the ionosphere and the magnetosphere result in a very dynamic plasma environment that consists of sources of free energy and a variety of micro-scale plasma processes and instabilities. In such conditions the assumption of thermal equilibrium in the standard ISR fitting procedure is no longer valid and if used may result in significant errors in derivation of the plasma parameters. Therefore, it is of great practical importance to identify such processes, understand the underlying physics, and ultimately advance the theoretical models to account for the new physics.

Micro-scale plasma instabilities are examples of such plasma processes. Instabilities are

significant in that 1) they are indicators of the presence of interesting and yet often not fully understood dynamics and 2) they are, under proper conditions, easily identifiable through the bold and distinctive signatures they produce in ISR spectra. Their detection with ISRs, therefore, provides a unique opportunity to expand the current understanding on these and other closely related topics in space/plasma physics. The two plasma instabilities that can be identified with ISRs at high latitudes and are subjects of this thesis are 1) low-frequency ion acoustic turbulence and 2) high-frequency Langmuir turbulence, both of which are universal processes in plasmas and have been seen to occur in many plasmas from planetary ionospheres and foreshocks, to solar wind plasma, and to laboratory plasmas. Their occurrence in the high-latitude ionosphere is highly relevant to other topics such as electric currents and electron beams, wave-particle interactions, acceleration mechanisms for charged particles, and in general magnetosphere-ionosphere interactions.

This thesis presents new experimental results on ion acoustic turbulence and Langmuir turbulence in the high-latitude ionosphere and discusses their implications under the context of magnetosphere-ionosphere interactions.

1.1 Main Contributions of this Thesis

This work places emphasis on the capability of incoherent scatter radars (ISRs) as powerful remote sensing tools for studying the plasma environment around the earth. It is shown how careful investigations of anomalies in incoherent scatter radar data may

provide detailed information on micro-scale plasma processes and instabilities in the ionosphere as well as provide insights into the magnetospheric energy sources and magnetosphere-ionosphere interactions in general [Akbari and Semeter, 2014; Akbari *et al.*, 2012; 2013; 2015a; 2015b].

Through an ISR experiment for the first time we investigate the dependence of low frequency ion acoustic turbulence on magnetic aspect angle. The results are somewhat unexpected and show a very strong aspect angle sensitivity. The sensitivity was found to depend on both altitude and spectral morphology, providing a means of classifying the results according to allowable generation mechanisms and sources of free energy. The results showed that during dynamic geophysical conditions, such as the substorm intervals studied in the experiment, more than one of the generation mechanisms proposed to explain NEIALs may be simultaneously at work [Akbari *et al.*, 2014].

This thesis, moreover, discovers a new type of echoes in incoherent scatter radar data and identifies them as signatures of Langmuir turbulence in the F region ionosphere [Akbari *et al.*, 2012]. The results immediately connect the ISR data to in-situ measurement of waves and particles in the ionosphere and to the similar processes observed in the solar wind, bridging the ISR community to the rocket and satellite communities and to the solar wind community. This work further discovers a connection between the Langmuir turbulence echoes and a type of electromagnetic radiation on the ground, the medium frequency (MF) burst. The connection supports one out of the four

generation mechanisms that have been proposed to explain MF burst [Akbari *et al.*, 2013].

To identify the source of free energy underlying the ISR Langmuir turbulence echoes, we employ plasma simulations. The dynamics of Langmuir turbulence and the five regimes of the linear parametric instabilities are studied with Zakharov simulations and the simulation results are compared to the experimental results. It is concluded that the source of free energy is most likely provided by unstable suprathermal (< 40 eV) electron populations rather than magnetospheric origin electron beams with energies of hundreds of eV. In the light of the discussions that suggest collisionally produced suprathermal electron populations most likely lack unstable features, the simulation results predict that a local acceleration mechanism for electrons in the F region auroral ionosphere is possibly responsible for the turbulence [Akbari *et al.*, 2015a].

1.2 Terminology

The work presented in this thesis borrows concepts and terminology from two separate branches of science, radar and plasma physics. It, therefore, is necessary to define some of the terms that are widely used throughout this thesis.

Langmuir wave or mode: refers to a natural longitudinal mode that exists in plasmas and concerns oscillations of electrons. Langmuir waves have frequencies close to the plasma frequency, which is in the range of several MHz for ionospheric plasmas.

Ion acoustic wave or mode: refers to another natural longitudinal mode that exists in plasmas and concerns oscillations of ions. Ion acoustic waves have frequencies generally in the range of kHz for ionospheric plasmas.

Plasma instability: in the context of this thesis plasma instability refers to a process, involving one or more plasma waves, during which the waves grow exponentially to high intensities due to the presence of a positive feedback mechanism. Plasma instabilities require a source of free energy that provides the energy for the growth of the waves.

Langmuir turbulence: in general, plasma turbulence refers to the state where plasma waves are simultaneously enhanced over a broad range of wave numbers and frequencies. Langmuir turbulence is one example of plasma turbulence and involves Langmuir and ion acoustic waves and their nonlinear interactions.

Cavitons: are referred to nonlinear features in plasmas, produced in strong Langmuir turbulence. Cavitons consist of small scale (< 1 meter) stationary ion density cavities in which intense Langmuir waves are trapped.

Incoherent scatter spectrum: refers to either the analytical, measured, or simulated spectrum of an incoherently scattered signal as a function of wave number and frequency. It is possible to visualize every possible wave mode of plasmas in this spectrum.

Incoherent scatter radar (ISR) spectrum: refers to the incoherent scatter spectrum obtained by an ISR. The spectrum only represents plasma wave activities at a single wave number and is often confined to a limited frequency band. Radars often utilize multiple

receiver bands shifted in frequency in order to detect different frequency components of the ISR spectrum.

Ion line channel: refers to the radar receiving channel or frequency band centered at the radar transmitting frequency. The bandwidth of this channel is suitable for detecting ion acoustic waves and therefore the intensity of the signal in this channel represents the intensity of ion acoustic waves in the plasma.

Plasma line channels: refer to two radar receiving channels or frequency bands shifted to lower (down-shifted plasma line channel) and higher (up-shifted plasma line channel) frequencies by the plasma frequency from the radar transmitting frequency. The bandwidths of these channels are suitable for detecting Langmuir waves and therefore the intensity of the signal in these channels represent the intensity of Langmuir waves in the plasma.

Naturally enhanced ion acoustic lines (NEIALs): refers to anomalous enhancements in intensity of the signal received in the ion line channel of ISRs. The enhancements represent intensification of ion acoustic waves by plasma instabilities.

Zakharov equations: refers to a couple of coupled nonlinear partial differential equations that provides the mathematical framework that is often used to simulate the interactions of Langmuir waves and ion acoustic waves, i.e. Langmuir turbulence.

MF Burst: short for medium frequency burst, is one type of natural electromagnetic radiation associated with auroral activities that is often observed on the ground.

Suprathermal electrons: refers to electrons with energies that are higher than the thermal energy level of the bulk electrons. In the context of this thesis, suprathermal energies refer to energies from several eV to one hundred eV.

Soft electron precipitations: refers to electron precipitation events predominantly consisting of electrons with energies of hundreds of eV. Soft electron precipitations are defined in oppose to hard or energetic electron precipitations that refer to precipitating electrons with energies greater than 1 keV.

1.3 Thesis Organization

The organization of this thesis is as follow: Chapter 2 begins with a short introduction describing the plasma environment around the earth. The earth's ionosphere, magnetosphere, and their connections at high latitudes are briefly discussed. The concept of plasma waves, two important modes of plasma that are closely relevant to the research presented in this thesis, i.e. Langmuir and ion acoustic modes, and the concept of plasma instabilities are then visited. Theory of incoherent scattering and incoherent scatter radars are later introduced. Finally, two examples of plasma turbulence, i.e. Langmuir turbulence and ion acoustic turbulence, their detection by incoherent scatter radars, and the topic of naturally enhanced ion acoustic lines (NEIALs) are introduced.

Chapter 3 is devoted to the topic of NEIALs. Different generation mechanisms for NEIALs are discussed. Results from an ISR experiment is then presented where aspect

angle dependence of NEIALs is used to distinguish different generation mechanisms and sources of free energy for NEIALs.

In Chapter 4, ISR experimental results are presented that led to discovery of a new type of echo in ISR data. The experimental data are followed by a discussion section that identifies the discovered echoes as signatures of Langmuir turbulence in the ionosphere. Next, results of an extensive search in ISR database are presented where more examples of the echoes are identified. Connections between the radar echoes, i.e. Langmuir turbulence, and a type of electromagnetic radiation, i.e. MF burst, and their relation with soft (< 500 eV) electron precipitations are discovered and discussed.

Chapter 5 is devoted to numerical simulations of Langmuir turbulence. Zakharov equations are described and are employed to simulate ionospheric Langmuir turbulence as would be produced by magnetospheric origin electron beams. Dynamics of the turbulence for many sets of beam parameters are described and their signatures in ISR data are compared to the experimental results. In the light of this comparison the source of free energy for the observed ISR echoes is discussed and it is concluded that a local accelerating mechanism in the auroral F region is most likely at work.

Summary and conclusions of this work are presented in Chapter 6 along with a discussion on the possible future directions.

Experimental and simulation results presented in Chapters 3-5 have been published in five journal articles in Geophysical Research Letters and Journal of Geophysical

Research-Space Physics. References to the journal articles can be found in the References Section of this thesis.

Chapter 2

Background

This chapter reviews concepts that are necessary in order to follow the research presented in this thesis. This review begins with a brief description of the plasma environment surrounding the earth, i.e. the ionosphere and the magnetosphere. Plasma wave modes present in warm magnetized plasmas, in particular ion acoustic and Langmuir waves, and the concept of plasma instability and turbulence are then discussed. Chapter 2 then goes on to introduce the concept of incoherent scattering and incoherent scatter radars (ISRs). Low frequency ion acoustic turbulence and its signature in ISR data, i.e. naturally enhanced ion acoustic lines (NEIALs), is then discussed. Beam-plasma interactions, Langmuir turbulence, and ionospheric heating experiments are the final topics introduced in this chapter.

2.1 The Earth's Plasma Environment

2.1.1 The Ionosphere

The earth's upper atmosphere is constantly ionized by solar radiation. Solar radiation at ultraviolet (UV) and X-Ray wavelengths have enough energy to detach electrons from neutral atoms and produce free electrons for a short period of time before they are captured by nearby positive ions. The ionization has a profile as a function of altitude and maximizes in a region called the ionosphere, which extends from 80 km to about 1000

km in altitude. At the peak of the ionization, at about 300 km, the number of electrons and ions is still negligible compared to the number of neutral atoms, however, the amount of produced free electrons is sufficient to affect electromagnetic wave propagation. The ionosphere, therefore, is of great practical importance in fields such as radio wave propagation and communication systems.

The dynamics in the ionosphere are somewhat complicated. While the neutral atmosphere is ionized by solar radiation another process, called recombination, works in the opposite direction to reduce the number of ions and free electrons. Recombination works since the negatively charged electrons and positively charged ions are attracted to each other by the Coulomb force and, therefore, are willing to combine and form a neutral atom. Recombination itself is a function of many parameters such as temperature and density. For instance, at lower altitudes recombination accelerates due to the increase in the plasma density, which results in electrons and ions being closer to each other. The balance between the ionization and recombination rates determines the electron density profile of the ionosphere.

This profile is shown in Figure 2.1. In this figure different species of ions are shown. The ionospheric ion composition is a function of altitude that is to a great extent determined by the neutral composition.

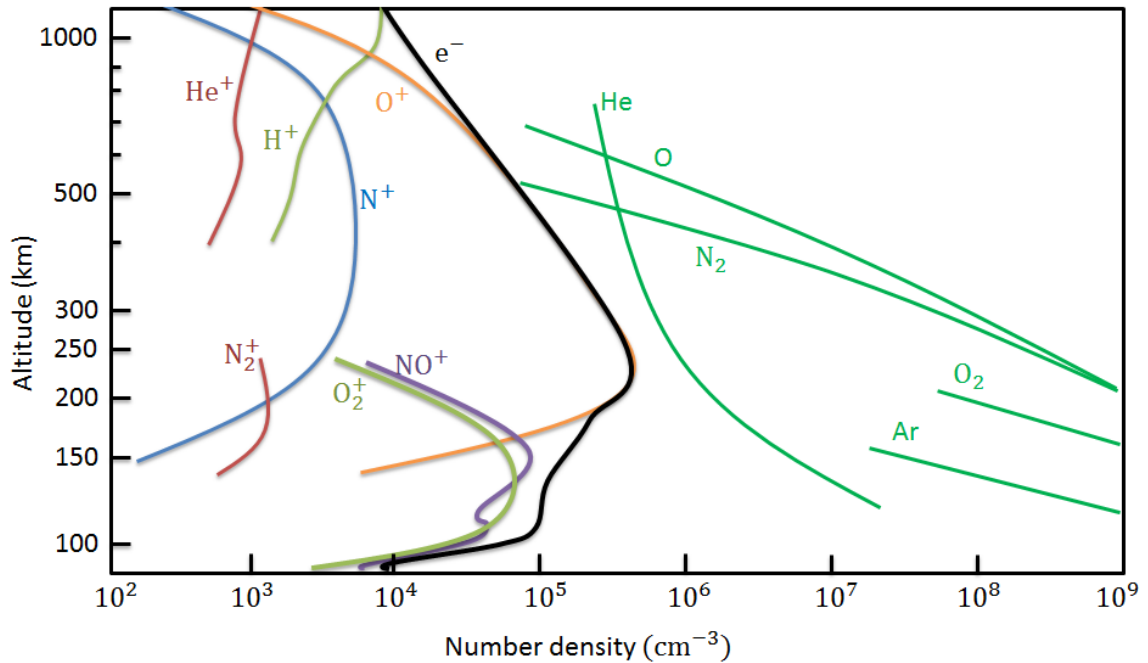


Figure 2.1. Density profile of the electron and the main ion and neutral species composing the ionosphere. (From *Kelley* [1989])

Historically, the ionosphere was discovered and named in layers. The layers have somewhat different characteristics and are produced by solar radiation at different frequency bands. The innermost layer, the D layer, extends from 50 km to 90 km above the surface of the earth. This layer is ionized by a combination of Lyman series-alpha hydrogen radiation, solar hard X-Rays, and cosmic rays and is predominantly composed of O_2^+ , N_2^+ , and NO^+ . The recombination rate in the D region is high and as a result this layer disappears during the night. Enhanced absorption of radio waves by the D region during the day may result in disturbance of distant AM radio broadcast.

The E and F layers that extend from 90 km to 120 km and 120 km to about 1000 km, respectively, are the next two layers of the ionosphere. While the E region is mainly ionized by solar soft X-Ray and far ultraviolet radiations, the F region is mainly ionized by solar extreme ultraviolet. The E layer often disappears at night due to disappearance of the ionization sources and high recombination rate. The F layer, however, remains during the night due to the lower recombination rate in this layer.

2.1.2 The Magnetosphere

The earth's magnetosphere is a plasma region surrounding the ionosphere where charged particles are subject to magnetic and electric forces that are much greater than the force exerted by gravity. The ions and free electrons in the magnetosphere have origins in the ionosphere and the solar wind. In spite of its name, the magnetosphere is not a sphere. Its shape is determined as a result of interactions between the earth dipolar magnetic field, interplanetary magnetic field, and the solar wind plasma. The boundary of the magnetosphere is called the magnetopause, located as far as 10-12 earth radii on the day side (the side facing the sun) and as far as 200 earth radii in the tail region (magnetotail) in the night side. The schematic of the magnetosphere, including the magnetopause and the magnetotail, is shown in Figure 2.2.

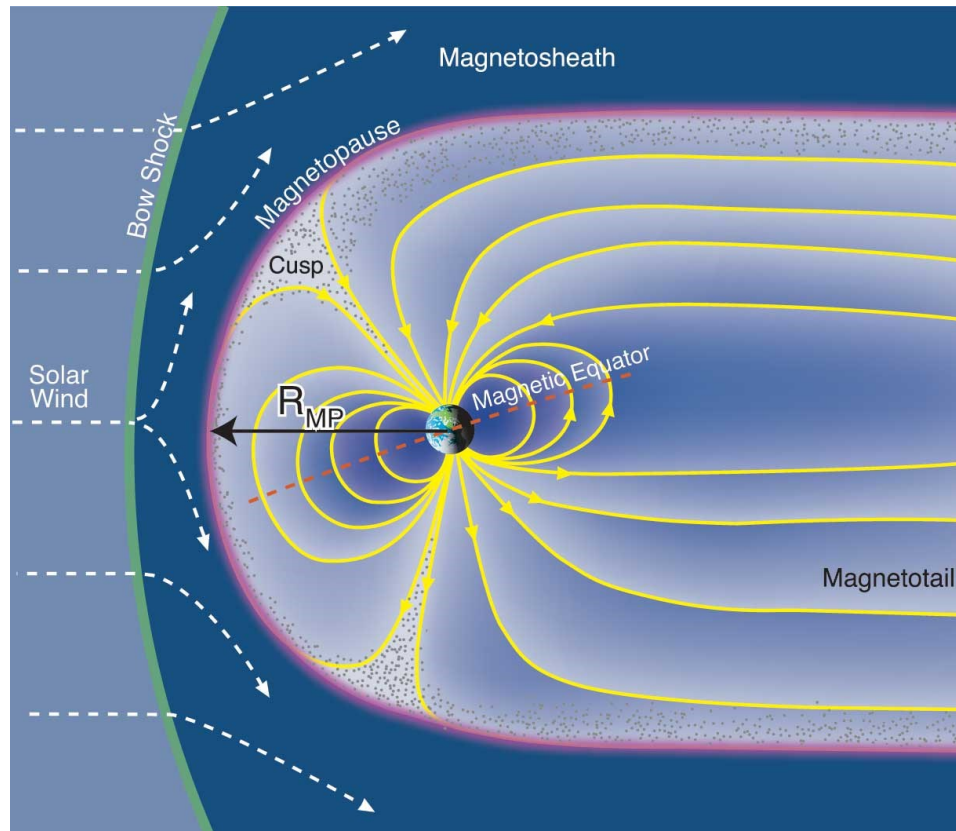


Figure 2.2. Schematic of the earth's magnetosphere. (Credit Fran Bagenal and Steve Bartlett)

As the solar wind approaches a planet that has a well-developed magnetic field (such as Earth, Jupiter and Saturn), the particles are deflected by the Lorentz force. The magnetosphere causes the particles to travel around the planet rather than bombarding its atmosphere or surface. However, at high latitudes interactions of the earth's magnetic field and the interplanetary magnetic field result in the appearance of a pair of neutral points on the day side, one in each hemisphere, where the magnetic field is zero. These cusp points provide the possibility for the solar wind particles to directly enter the ionosphere without ever crossing magnetic field lines. Moreover, distortions of the

earth's magnetic field by the solar wind sometimes lead to a rapid reconfiguration of the magnetic field in the magnetotail region where a process called magnetic reconnection may occur in which a large amount of magnetic energy may be impulsively released in the form of acceleration of electrons and ions. The accelerated particles follow the earth's magnetic field lines and precipitate into the ionosphere where they collide with the dense neutral atmosphere of the earth, creating ionization and light that is known with the name aurora or the northern light (shown in Figure 2.3).

In the dynamic environment of the auroral region a variety of processes occur that are interesting topics in plasma physics; processes whose investigation provides deep insights into fundamental interactions that occur universally in cosmic plasmas. Examples of such processes are wave-particle interactions, plasma instabilities, and turbulence. These are the focus of this thesis.

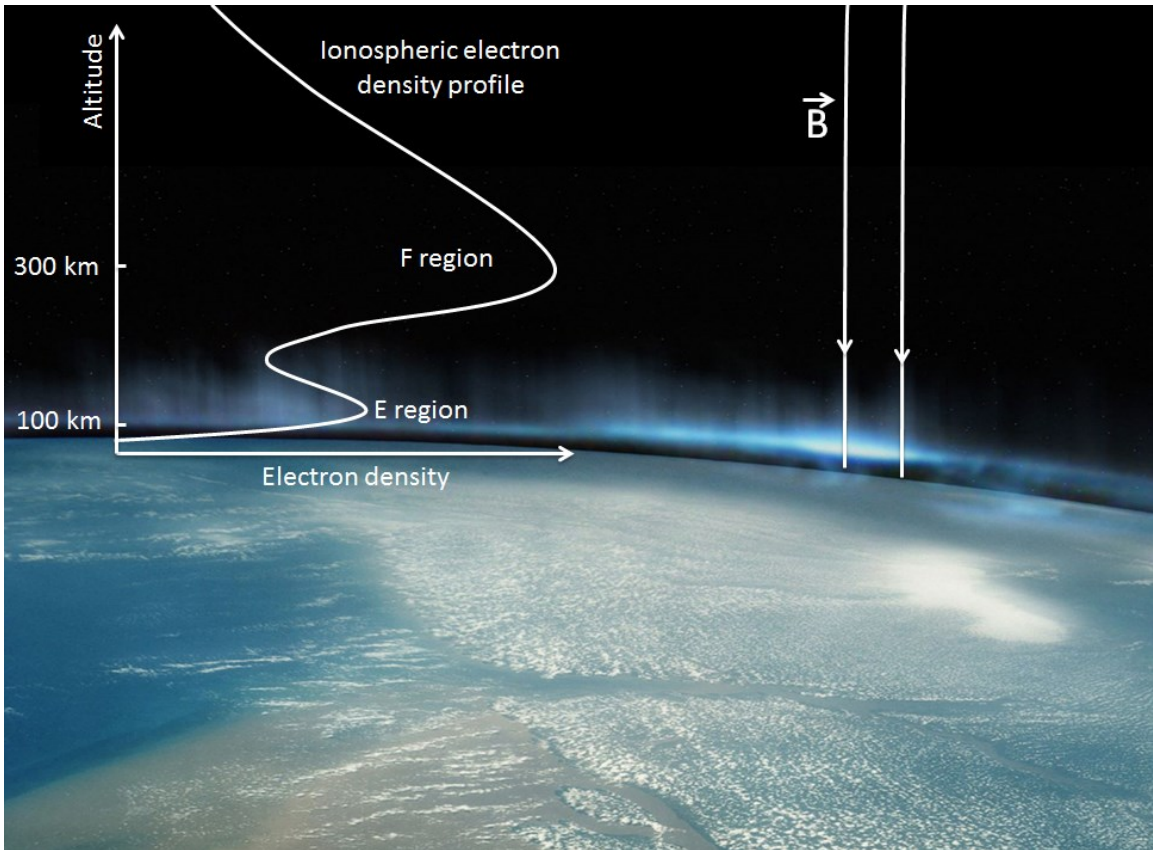


Figure 2.3. The earth's auroral region. Aurora predominantly originates from the E and the F regions of the high-latitude ionosphere. (Credit International Space Station)

2.2 Plasma Waves and Instabilities

2.2.1 General Treatment of a Warm Plasma

A plasma wave is an interconnected set of particles and fields that propagate in a periodically repeating fashion. The presence of charge particles with different masses and energies, together with the presence of external magnetic fields in plasmas, creates a

complex system that can support a variety of wave modes that do not exist in free space. Waves in plasmas can be classified as electromagnetic or electrostatic according to whether there exists an oscillating magnetic field. Plasma waves can further be classified based on the oscillating species (i.e. electrons or ions) and based on whether they propagate in an unmagnetized plasma or based on their propagation direction in a magnetized plasma. Plasma wave modes are often uniquely identified by their dispersion relation, which is the relation between the frequency (ω) and the wave number (k) of the wave mode. In what follows, we provide a background on the standard procedure that is often followed in order to derive the dispersion relations for various wave modes and introduce the two modes of plasma that are relevant to the research presented in this thesis. This section is not meant to be inclusive. Interested readers are referred to standard plasma physics text books (e.g. *Chen* [1984]) for detailed discussions.

Interactions of charged particles and fields, which plasma waves are a specific form of, are governed by the Boltzmann equation and the Maxwell's equations. The Boltzmann equation (equation 2.1) determines how the distribution of particles in physical space and velocity space evolves over time in the presence of a force acting on the particles.

$$\frac{\partial f(r,v,t)}{\partial t} + \mathbf{v} \cdot \frac{\partial f(r,v,t)}{\partial \mathbf{r}} + \frac{F}{m} \cdot \frac{\partial f(r,v,t)}{\partial \mathbf{v}} = \left(\frac{\partial f}{\partial t} \right)_C \quad (2.1)$$

In this equation $f(r, v, t)$ represents the distribution of a population of particles (i.e. electrons or ions) as a function of the three physical (spatial) components $r = (x, y, z)$, the three velocity components $\mathbf{v} = (v_x, v_y, v_z)$, and time t . In this equation F is the force

acting on the particles, m is the mass of the particles, and $\left(\frac{\partial f}{\partial t}\right)_c$ is the time rate of change of f due to collisions. Also symbols $\frac{\partial}{\partial r}$ and $\frac{\partial}{\partial v}$ stand for gradients in spatial (physical) space and velocity space, respectively, and are given by:

$$\frac{\partial}{\partial r} \equiv \frac{\partial}{\partial x} \hat{x} + \frac{\partial}{\partial y} \hat{y} + \frac{\partial}{\partial z} \hat{z} \equiv \nabla \quad (2.2)$$

$$\frac{\partial}{\partial v} \equiv \frac{\partial}{\partial v_x} \hat{x} + \frac{\partial}{\partial v_y} \hat{y} + \frac{\partial}{\partial v_z} \hat{z} \equiv \nabla_v \quad (2.3)$$

$f(r, v, t)$ means that the number of particle per m^3 at position r and time t with velocity components between v_x and $v_x + dv_x$, v_y and $v_y + dv_y$, and v_z and $v_z + dv_z$ is $f(r, v, t) dv_x dv_y dv_z$. If we ignore the term due to collisions and further assume that the force F is purely electromagnetic, equation 2.1 takes the form:

$$\frac{\partial f(r, v, t)}{\partial t} + v \cdot \frac{\partial f(r, v, t)}{\partial r} + \frac{q}{m} (E + v \times B) \cdot \frac{\partial f(r, v, t)}{\partial v} = 0 \quad (2.4)$$

This is called the Vlasov equation. The derivation and the meaning of the Vlasov equation can be found in plasma physics text books (e.g. *Chen* [1984], Chapter 7) in sections that discuss the kinetic theory of plasma.

Motion of charged particles, in turn, may lead to generation of electric current J and accumulation of electric charge ρ . These are given by:

$$\rho = \sum_j q_j n_j = \sum_j q_j \iiint f_j(r, v, t) dv_x dv_y dv_z \quad (2.5)$$

$$J = \sum_j q_j n_j v_j = \sum_j q_j \iiint f_j(r, v, t) v dv_x dv_y dv_z \quad (2.6)$$

Where subscript j represents different populations or species of charged particles (i.e. electrons and ions) and n and q are the number density and electric charge of each species. According to the Maxwell's equations (equation 2.7–2.10) accumulation of electric charge and current generate electric and magnetic fields which, in turn, modifies the electromagnetic force that acts on the particles in the Vlasov equation.

$$\nabla \times \mathbf{E} = \frac{-\partial \mathbf{B}}{\partial t} \quad (2.7)$$

$$\nabla \times \mathbf{B} = \mu_0 \mathbf{J} + \frac{1}{c^2} \frac{\partial \mathbf{E}}{\partial t} \quad (2.8)$$

$$\nabla \cdot \mathbf{E} = \frac{\rho}{\epsilon_0} \quad (2.9)$$

$$\nabla \cdot \mathbf{B} = 0 \quad (2.10)$$

The Vlasov equation and the Maxwell's equations are, therefore, self-consistent equations that describe evolution of particles and fields where particles produce fields as they move along their trajectories and the fields cause the particles to move in those exact trajectories. These equations can be used to identify various wave modes of plasma and derive their dispersion relations.

This approach that takes into account the distributions of electrons and ions in velocity space is called the kinetic theory. Kinetic theory is very successful in describing a variety of plasma processes; however, the level of complexity in this approach limits the extent of analytical solutions that one can derive. Moreover, this approach is often computationally highly expensive. In many cases, the Vlasov equation can be replaced by its moments, the continuity equation and the equation of motion for particles. This approach provides simplifications that enable one to treat the equations analytically and

derive the dispersion relations. Reducing the Vlasov equation to its moments is based on the fluid theory of plasma physics and fluid mechanics in which the identity of the individual particles is neglected as electron and ion populations move as a whole in a form of fluids. In the fluid theory, assuming a constant Maxwellian distribution in velocity, the distribution is uniquely described by a single number, temperature, through averaging. This approach is sufficiently accurate to describe the majority of plasma physics processes.

The lowest moment of the Vlasov equation is obtained by integrating equation 2.4 with respect to velocity, i.e. $\iiint (\text{equation 2.4}) dv_x dv_y dv_z$. It can be shown that the first moment yields

$$\frac{\partial n(r,t)}{\partial t} + \nabla \cdot (nu) = 0 \quad (2.11)$$

Where $n(r, t) = \iiint f(r, v, t) dv_x dv_y dv_z$ is the number density for the corresponding fluid and $u(r, t)$ is the averaged fluid velocity by definition. This equation means that the total number of particles in a volume can change only if there is a net flux of particles across the surface that bounds the volume.

The next moment of the Vlasov equation is obtained by multiplying equation 2.4 by mv and integrating with respect to velocity. This yields the fluid equation of motion that describes the flow of momentum.

$$mn(r, t) \left[\frac{\partial u(r,t)}{\partial t} + (u \cdot \nabla)u \right] = qn(E + u \times B) - \nabla P \quad (2.12)$$

In the above equation ∇P is the Stress Tensor that takes into account the thermal motions of the particles relative to the fluid velocity. This term represents the pressure gradient force in thermodynamics. For the wave modes whose existence depends on the presence of this term, an additional equation (equation of state in thermodynamics) is needed that relates P to n and, therefore, a closed system of equations with equal number of equations and unknowns is derived (see Chapter 3 of *Chen* [1984]).

2.2.2 Ion Acoustic Waves and Langmuir Waves

Of all the wave modes supported in magnetized plasmas, two are relevant to this thesis. These are the ion acoustic mode and the Langmuir mode. The ion acoustic wave is a longitudinal oscillation of ions where the much faster electrons are simply following the lead of heavy ions. The ion oscillations appear as a result of competition between the Coulomb force in the momentum equation and ions' inertia. This wave mode is similar to the acoustic waves in neutral gasses with the difference that the positively charged ions mainly interact through electric fields rather than through collisions. By combining the equation of motion, the continuity equation, and the equation of state for the ion and the electron fluids together with the third Maxwell's equation (equation 2.9) and following the standard methods of plasma physics (see Chapter 4 of *Chen* [1984]), it is straight forward to show that in the long wave length limit the waves propagating in the direction of the background magnetic field lines (or propagating in an unmagnetized plasma),

follow the dispersion relation $\omega^2 = C_s^2 k^2$ where $C_s = \sqrt{\frac{Z k_B T_e + 3k_B T_i}{M}}$ is called the speed of sound in the plasma. Here $Z, k_B, T_e, T_i,$ and M are charge of the ion, Boltzmann constant, electron temperature, ion temperature, and ion mass.

In contrast to the ion acoustic waves, Langmuir waves are rapid oscillations of electrons in plasmas. The frequency of the oscillations is high and therefore the dynamics of the much heavier ions can be entirely ignored and the ion density can be assumed uniform. This is because the ions are not able to respond in the time scale relevant to this mode due to their inertia. Again, by combining the equation of motion, the continuity equation, and the equation of state for the electron fluid (under the assumption of stationarity for the ions) together with the third Maxwell's equation, it is straight forward to derive the simplified dispersion relation for Langmuir waves: $\omega^2 = \omega_p^2 + 3k^2 v_e^2$ where $\omega_p = \sqrt{\frac{ne^2}{m\epsilon_0}}$ is the plasma frequency and $v_e = \sqrt{\frac{k_B T_e}{m}}$ is the electron thermal speed (see Chapter 4 of *Chen [1984]*). Here $n, e, \epsilon_0, m,$ and T_e are electron density, electron charge, permittivity of free space, electron mass, and electron temperature, respectively. In a magnetized plasma and for Langmuir waves propagating with angle θ with respect to the magnetic field lines an additional terms appears in the dispersion relation and the dispersion relations takes the form $\omega^2 = \omega_p^2 + 3k^2 v_e^2 + \Omega_e^2 \sin^2(\theta)$ where Ω_e is the electron gyro frequency [*Dysthe, 1978*]. However, observations presented in this thesis involve Langmuir waves that propagate near parallel to the magnetic field lines and therefore this term can be safely ignored.

In reality, the frequency of the waves that appear in dispersion relations is complex and in the form of $\omega = \omega_r + i\omega_i$ where the imaginary part determines the growth rate or damping of the wave mode as a function of wave number. Any solution of the dispersion relation, for which $\omega_i < -|\omega_r|$ is regarded as a heavily damped oscillation. The term *wave* is used to refer to those weakly damped solutions for which $-|\omega_r| < \omega_i < 0$. On the other hand, the condition $0 < \omega_i$ refers to an instability; which means that in the presence of a source of free energy the wave exponentially grows in amplitude to an extent where secondary effects take over and quench the growth. Instabilities require existence of a positive feedback mechanism to operate.

The required free energy for instabilities may appear in a variety of forms such as magnetic configuration, anisotropic plasma pressure, streaming of plasma particles with respect to each other, etc. In the next sections two types of instabilities that often happen in the ionosphere, i.e. streaming instabilities, which may lead to ion acoustic turbulence, and bump-on-tail instability, which may lead to Langmuir turbulence, are introduced. Before, however, the concept of incoherent scattering and incoherent scatter radars (ISRs) are introduced in the next section.

2.3 Incoherent Scatter Radar (ISR) Technique

2.3.1 The Physics of Incoherent Scattering

1. Scattering by Electrons

Scattering from random thermal fluctuations in a plasma is the basic theory behind a powerful remote sensing technique called incoherent scattering. In ionospheric studies, incoherent scatter radars (ISRs) employ this technique to measure time variation of a single component of the spatial Fourier transform of the electron density fluctuations. Incoherent scatter radars send powerful signals to the ionosphere at a transmitting frequency that is very large compared to the plasma frequency. Most of the power penetrates through the ionosphere and is lost in space. A very small fraction of the power, however, gets scattered by the charged particles in the ionosphere. The scattering occurs in every direction and only a portion of the scattered signal that propagates to the radar site can be measured. Of particular interest is the frequency spectrum of the measured signal (the ISR spectrum) as it contains quantitative information on the bulk properties of the plasma.

Imagine a single electron at the origin of the coordinate system that is being illuminated by an incident electromagnetic wave E_i . The equation of motion for the electron yields $m \frac{\partial u(0,t)}{\partial t} = -eE_i(0,t)$. From the electrodynamics theory we know that an oscillating electron radiates electromagnetic fields. For this electron the radiated, or scattered, field

E_s at point r_s is given by $E_s(r_s) = \frac{-e\mu_0}{4\pi r_s^3} r_s \times [r_s \times \frac{\partial u(0,t')}{\partial t}]$ where $t' = t - \frac{r_s}{c}$ is the

retarded time and c is the speed of light. By combining the two equations we can derive an expression that relates the scattered field to the incident field:

$$|E_s(r_s, t)| = \frac{e^2 \mu_0 \sin \theta}{4\pi r_s m_e} |E_i(0, t')| = \frac{r_e}{r_s} \sin \theta |E_i(0, t')| \quad (2.13)$$

Where $r_e = \frac{e^2 \mu_0}{4\pi m_e}$ is the classical electron radius and θ is the angle between E_i (at the origin) and r_s . The geometry is illustrated in Figure 2.4.

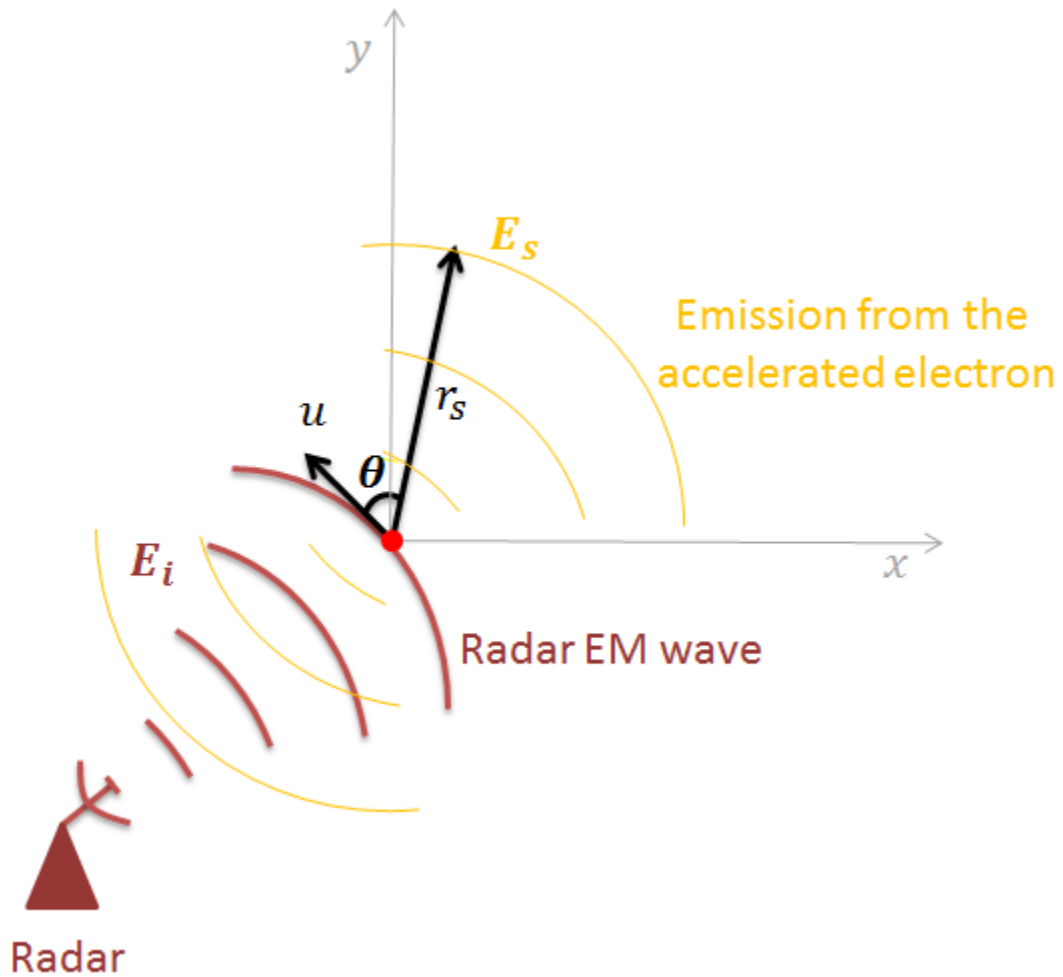


Figure 2.4. Scattering from a single electron.

The scattering of the radar's electromagnetic wave by the ionosphere arises from a collection of electrons rather than a single electron. In this case the total scattered signal is simply the sum of scattered signals from individual electrons in the volume that is being illuminated by the radar's electromagnetic pulse. The shape of this volume is determined by the radiation pattern of the radar and the length of the transmitted pulse. Imagine such a volume of plasma (V) centered at point R and assume that the radar is located at the origin of the coordinate system (see Figure 2.5). The frequency of the incident electromagnetic wave is so high (hundreds of MHz) that the ions cannot contribute to the scattering. That is because the heavy ions cannot be accelerated in such short time scales due to their high inertia. Therefore, the scattering arises only from the electrons. In this geometry the size of the volume is negligible compared to the distance between the radar and the center of the volume. In addition, since the intensity of the scattered signal is very low compared to the intensity of the incident wave we can 1) safely ignore multiple scatterings within the volume and 2) reasonably assume that the intensity of the incident radiation in the volume is not affected by the scattering and is constant in the entire volume (Born approximation). Therefore, we can conclude that the amplitude of the scattered signal from each individual electron in the volume is equal. What is not equal, however, is the phase of the scattered signal from individual electrons. The phase component is critical as it determines whether the scattered signals for different electrons are added constructively or destructively.

In order to keep track of the phase components consider the schematic in Figure 2.5. Consider the scattering by a particular electron at point r_p with respect to the center of the

volume V (i.e., the electron is at $\vec{R} + \vec{r}_p$). If the radar pulse at the origin has the phase $e^{-j\omega_0 t}$ then the scattered signal from this particular electron at the location of the radar is $e^{-j\omega_0 t} e^{\frac{j2\pi}{\lambda} 2|\vec{R} + \vec{r}_p|}$. Considering $|\vec{r}_p| \ll |\vec{R}|$ we can assume \vec{R} and $\vec{R} + \vec{r}_p$ are parallel and in the direction of \hat{R} . Now defining wave number $\vec{k} \equiv \frac{4\pi}{\lambda} \hat{R} = 2\vec{k}_{radar}$ and using equation 2.13 we can write the scattered signal at the location of the radar by a single electron located at point $\vec{R} + \vec{r}_p$:

$$E_{scatter,p}(t) = \frac{r_e}{R} E_0 e^{-j(\omega_0 t + \vec{k} \cdot \vec{r}_p + \vec{k} \cdot \vec{R})} \quad (2.14)$$

Now, assuming that the total number of N electrons with the distribution $N(\vec{r}, t)$ exist in the volume V the total scattered signal due to this distribution is given by:

$$\begin{aligned} E_{scatter}(t) &\approx \sum_{p=1}^{N_s} \frac{r_e}{R} E_0 e^{-j[\omega_0 t + \vec{k} \cdot \vec{r}_p(t')]} = \frac{r_e E_0}{R} e^{-j\omega_0 t} \sum_{p=1}^{N_s} e^{-j\vec{k} \cdot \vec{r}_p(t')} \\ &= \frac{r_e E_0}{R} e^{-j\omega_0 t} \int_V N(\vec{r}, t') e^{-j\vec{k} \cdot \vec{r}} d^3r = \frac{r_e E_0}{R} e^{-j\omega_0 t} N(k, t') \end{aligned} \quad (2.15)$$

Note that in equation 2.15, the phase term due to $\vec{k} \cdot \vec{R}$ is constant and, therefore, is removed. Also in this equation t' is an appropriately retarded time and $N(k, t')$ is the spatial Fourier transform of the electron density distribution $N(\vec{r}, t')$. The time variation of the electron density distribution reflects the fact that the electrons are continuously moving and redistributing themselves in new positions.

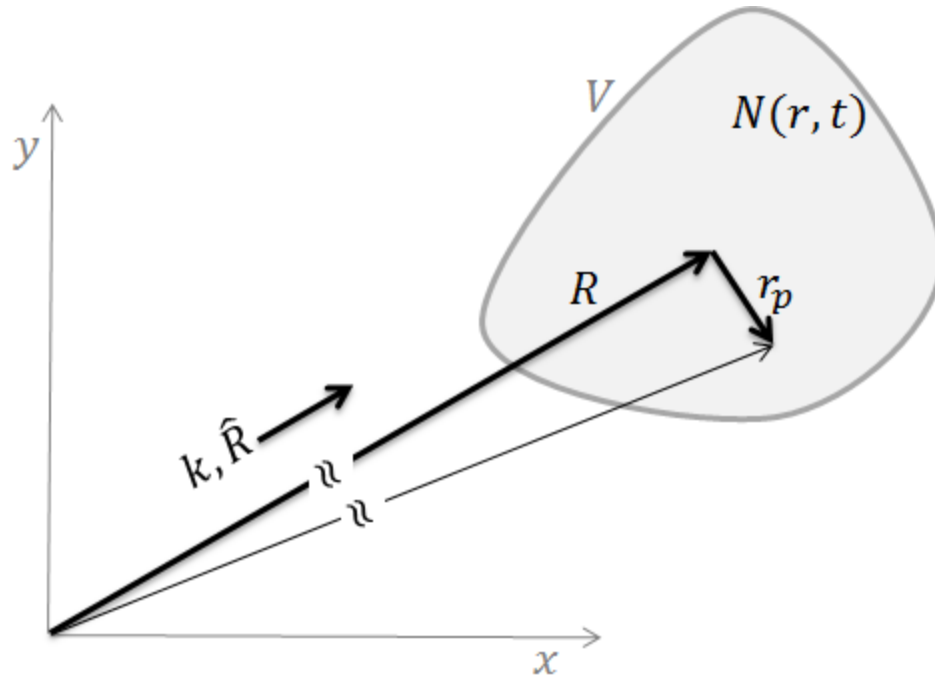


Figure 2.5. Scattering from a population of electrons.

Equation 2.15 reveals an important point. The scattered signal is proportional to a single component ($k = 2k_{radar} = \frac{4\pi}{\lambda} \hat{R}$) of the spatial Fourier transform of the electron distribution function. This point can be clearly understood under the concept of Bragg scattering that will be discussed shortly. Before leaving this discussion, however, it is important to note that the scattered signal derived in equation 2.15 is a stochastic signal that arises from many random contributions from a large number of electrons. According to the Central Limit Theorem of probability this signal is, in fact, a Gaussian random variable whose entire information is contained in its power spectrum or equivalently its autocorrelation function. Derivation of the power spectrum of the scattered signal is not straightforward and requires assumptions on the properties of the plasma (for instance on

the presence of a background magnetic field and collisions and on the distributions of electrons and ions in the velocity space). Such discussions are beyond the scope of this introductory section and are not included here. Figure 2.6, however, illustrates the power spectrum for a simple case of no collisions, no background magnetic field, and Maxwellian distributions for electrons and ions. The spectrum is continuous in frequency and consists of three sharp peaks that are called the ion acoustic line and the Langmuir lines. For the detailed derivation of the ISR spectrum readers are referred to *Hagfors* [2003].

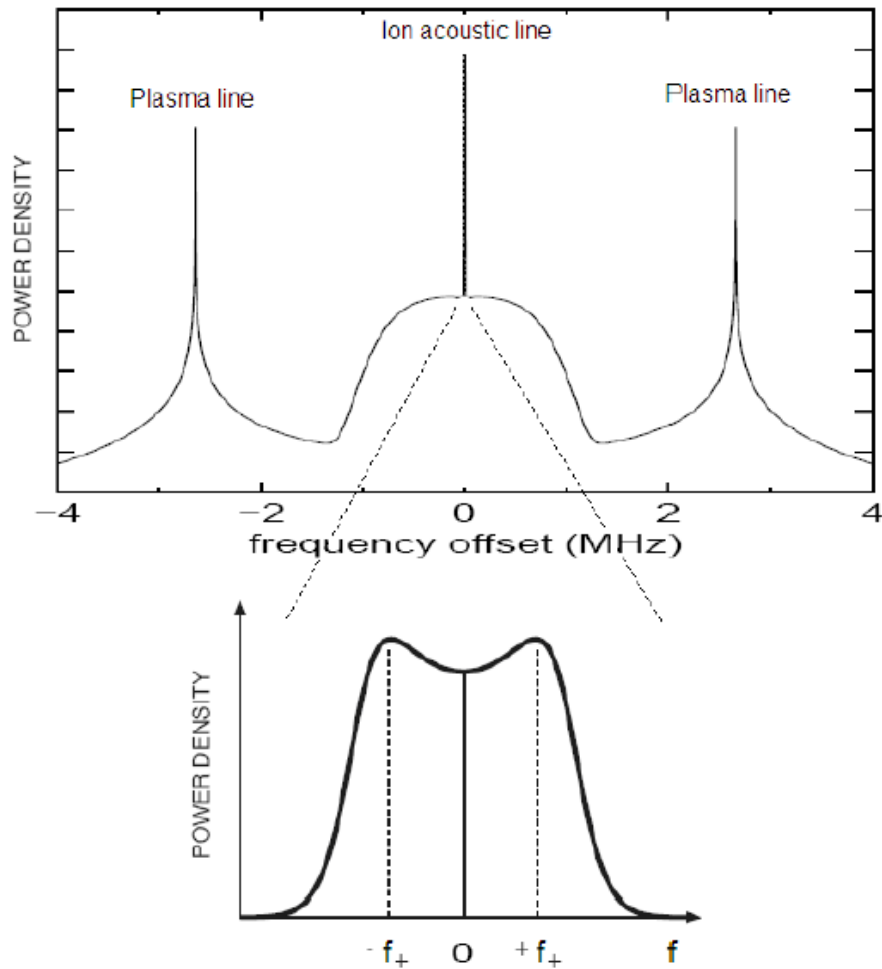


Figure 2.6. The top panel shows the incoherent scatter spectrum, which consists of the ion line and the plasma lines. The bottom panel zooms in the ion line, where the superposition of the two ion acoustic shoulders appears in the form of a single double-humped shape. The frequency axis is the offset frequency relative to the radar transmitting frequency. (Plot from *Diaz* [2008])

2. The Concept of Bragg Scattering

The presence of the sharp peaks in the ISR spectrum and the correlation of the scattered signal with one component of the spatial Fourier transform of the electron density fluctuations in the scattering volume (equation 2.15) can be understood through the concept of Bragg scattering. Consider a periodic structure consisting of a large number of weakly reflective planes that are separated by distance d . This is shown in Figure 2.7. For the simplest case, assume that the structure is being illuminated by an electromagnetic radiation that propagates in the direction perpendicular to the planes. Due to the weak reflectivity of the planes the radiated signal suffers small attenuation as it propagates through the structure. If we further neglect multiple reflections between the planes, the total reflected signal by the periodic structure consists of contributions from individual planes where different planes give rise to signals with same intensities but different phases.

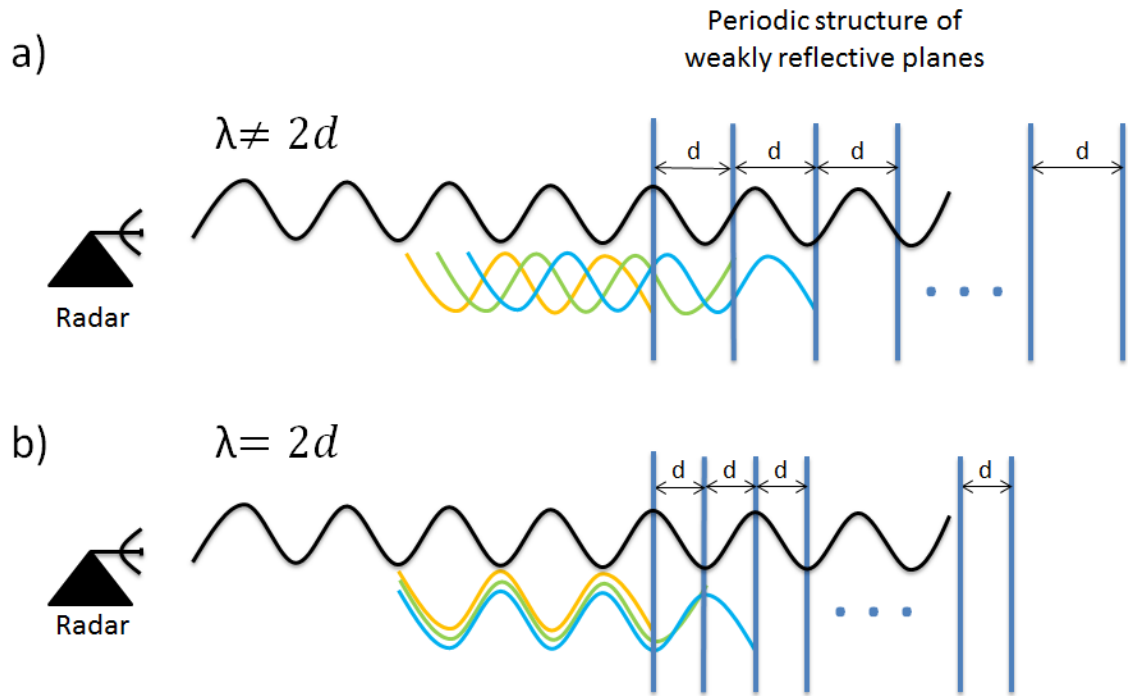


Figure 2.7. Bragg scattering by a periodic structure consisting of weakly reflective planes.

In general, the total scattering by the structure suffers from destructive interference of signals from different planes and the total scattered signal remains relatively weak. This is the case in Figure 2.7a. However, if the condition $\lambda = 2d$ is met, it can be shown that all the components from individual planes add constructively and the net scattered signal is strong. This is the case in Figure 2.7b. This condition ($\lambda = 2d$) is called the Bragg condition and the scattering is called the Bragg scattering. If many periodic structures with different separations between their planes are being simultaneously illuminated by an electromagnetic wave, the scattering, predominantly, arises from the periodic structure that satisfies the Bragg condition.

In plasmas, density waves act similar to the weakly reflective structures. In a sinusoidal wave each peak of the waveform represents a region of higher electron density (higher reflectivity), whereas each valley of the waveform represents a region of lower electron density (lower reflectivity). Plasma waves, therefore, organize the electrons in space and provide the possibility for them to scatter electromagnetic waves more efficiently. Thus, even though it is the electrons that scatter the radar wave it appears as if the scattering arises from the plasma waves.

Now consider equation 2.15. This equation represents the correlation between the scattered signal and one component of the spatial Fourier transform of the electron density fluctuations. The electron density fluctuations at any given time can be decomposed into its spatial Fourier components. Once the time variability of the fluctuations is considered, and this time variability is decomposed into temporal Fourier components, the electron density fluctuations appear as propagation of the spatial Fourier components in the form of waves (see *Hagfors* [2003]). Equation 2.15, therefore, means that only those waves (plasma waves) that satisfy the Bragg condition ($k = 2k_{\text{radar}} = \frac{4\pi}{\lambda} \hat{R}$ in Figure 2.5 or $\lambda = 2d$ in Figure 2.7) cause the scattering. This is the reason that it is often said that incoherent scatter radars observe wave activities at a single wavelength (wave number).

At the early years of developing the incoherent scatter radar theory, it was thought that the scattering is due to charged particles that move entirely incoherently in the illuminated volume; thus the term *incoherent scattering* was used. However, soon the role of plasma

waves and the coherence they cause on the motion of charged particles was discovered. Today, although it is known that the scattering is in fact, to some degree, coherent, for historic reasons the term *incoherent scattering* is still used to refer to the theory. Note that for sufficiently high radar frequencies where the probing wavelength falls below the Debye length of the plasma, the scattering would be purely incoherent since plasma waves do not exist at such small wavelengths [Evans, 1969].

A variety of plasma waves are continuously excited over a broad range of wavelengths by the thermal motions of ions and electrons. Unlike the periodic structures shown in Figure 2.7 such plasma waves are not stationary and their peaks and valleys propagate with the phase velocity $v_\phi = \frac{\omega}{k}$. Plasma waves, therefore, scatters the radar pulse at different frequencies than the radar transmitting frequency due to the Doppler effect. The change in frequency due to a relative velocity Δv between a transmitter and a receiver is $\Delta f = \frac{\Delta v}{c} f_0$ where f_0 and c are the transmitting frequency and the speed of light. In incoherent scattering this frequency shift appears twice since plasma waves once appear as receivers and later as transmitters. Inserting the phase velocity in this equation and noting $k = 2k_{radar} = \frac{4\pi}{\lambda}$ and $f_0 = \frac{c}{\lambda}$ we have:

$$\Delta f = 2 \frac{\Delta v}{c} f_0 = 2 \frac{\omega}{c} f_0 = \frac{\omega}{2\pi} \quad (2.16)$$

Which means that the frequency shift due to the Doppler effect is exactly equal to the frequency of the scattering plasma wave. Moreover, the plasma waves that propagate toward the radar cause positive Doppler and thus positive frequency shifts and the plasma

waves that propagate away from the radar cause negative Doppler and thus negative frequency shifts.

Under the condition where the radar wavelength is large compared to the Debye length (a situation that holds for the ISR measurements from the ionosphere) three electrostatic modes of plasma can cause scattering; these are the ion acoustic mode, the whistler mode, and the Langmuir mode; each producing a pair of enhanced peaks or lines in the ISR spectrum [Landau, 1946; Gross, 1951; Bernstein, 1958; Salpeter, 1960 and 1961; Perkins and Salpeter 1965]. The existence of the lines due to the whistler mode depends on the presence of the magnetic field and these lines disappear when the radar takes measurements in directions near parallel to the magnetic field lines. In such cases the spectrum only consists of the Langmuir and ion acoustic lines; thus explaining the spectrum seen in Figure 2.6.

The phase velocity of the ion acoustic waves is small and therefore the two ion lines are closely located to the radar transmitting frequency. Furthermore, ion acoustic waves are highly Landau damped in the ionosphere, which causes the ion lines to broaden in frequency. The superposition of the two ion acoustic lines, therefore, appears as a single double humped shape, which is simply called the ion line (Bottom panel of Figure 2.6) [Evans, 1969]. The phase velocity of Langmuir waves, on the other hand, is considerable and as a result the Langmuir lines are out shifted by a few Mega Hertz from the radar transmitting frequency. Incoherent scatter radars employ receiver channels tuned at the frequency of the three lines to detect the scattered signals from the corresponding waves

separately. The channels are called the ion line channel and the up-shifted and down-shifted plasma line channels. Intensity of the received signal in each channel monitors the amplitude of the corresponding plasma waves in the ionosphere.

3. Ion Line Spectrum

Even though Langmuir waves are weakly damped the intensity of the plasma lines is low due to the low level of thermal excitation for Langmuir waves. Therefore, most ISRs are unable to detect plasma lines when the ionosphere is in thermal equilibrium. Plasma lines, however, can be detected if Langmuir waves are subject to plasma instabilities that might occur in the presence of a proper source of free energy. Once detected the location of the plasma lines (close to the plasma frequency $\omega_p = \sqrt{\frac{ne^2}{m\epsilon_0}}$) provides an accurate estimate of the electron density.

Ion line, on the other hand, is stronger than the plasma lines and ISRs are often designed to detect this line. The details of the double-humped shape of the ion line spectrum depend on the parameters of the plasma (see Figure 2.8). For instance, the area under the spectrum, i.e. the entire power in the ion line channel, is proportional to the intensity of the scattering ion acoustic waves which, in turn, is proportional to the electron density in a plasma that is in thermal equilibrium. Also, the width of the spectrum depends on the ratio of the ion temperature to the ion mass; the peak to valley of the spectrum depends

on the ratio of the electron temperature to the ion temperature; and the overall frequency shift of the spectrum is proportional to bulk motion of plasma (Doppler effect).

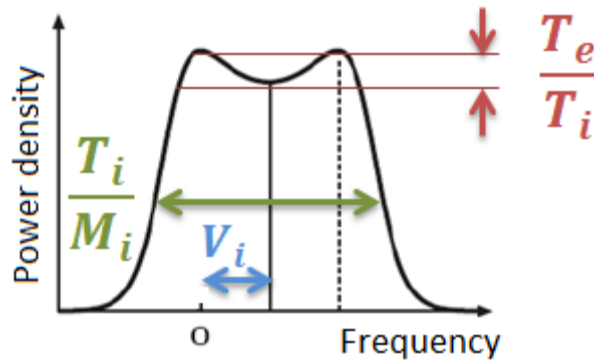


Figure 2.8. Dependence of the shape of the ion line spectrum on the plasma parameters.

Once measured, a nonlinear least square fitting procedure is used to fit the ion line spectrum to the theoretical model and derive the bulk plasma parameters in the ionosphere. The dependence of the shape of the ion line spectrum on the plasma parameters, however, is not one-to-one and changes in different plasma parameters may cause similar changes on the shape of the spectrum. Therefore, in practice, the fitting procedure is not ideal and it is not possible to derive all the plasma parameters that could potentially be derived. The fitting procedure often relies on ionospheric models to provide estimates of the ion composition and collision frequencies in order to remove some ambiguity in the fitting process.

Before leaving this section, it is important to mention once more that the theoretical spectra are often derived by imposing assumptions on the state of the plasma. The plasma is often assumed to be in thermal equilibrium consisting of electrons and ions with

Maxwellian distributions. Such assumptions, however, are commonly violated in the dynamic environment of high latitude ionosphere. For instance, at high latitudes the distribution of ions in velocity can deviate from Maxwellian due to the presence of intense (~ 100 mV/m) DC electric fields that often exist on the edge of energetic electron precipitations [Lockwood *et al.*, 1987]. In the same regions the presence of magnetic field aligned electric currents may lead to the ion acoustic instability [Foster *et al.*, 1988] during which the intensity of ion acoustic waves grow to very high values. In such cases, the measure ISR spectrum deviates from the double-humped shape shown in Figure 2.8 and any attempt to fit the measured ISR spectrum to the double-humped theoretical model may result in significant errors in deriving the plasma parameters.

The first ISR was constructed in 1958 in Jicamarca, Peru and since then there have been several incoherent scatter radar constructed around the planet, including: Arecibo, Puerto Rico; Sondrestrom, Greenland; EISCAT, Norway; Millstone Hill, Massachusetts, Poker Flat ISR, Alaska; and Resolute Bay ISR, Canada. The radar experimental results presented in this work have been obtained by the Poker Flat ISR (PFISR), which is shown in Figure 2.9 together with the main parameters of the radar.

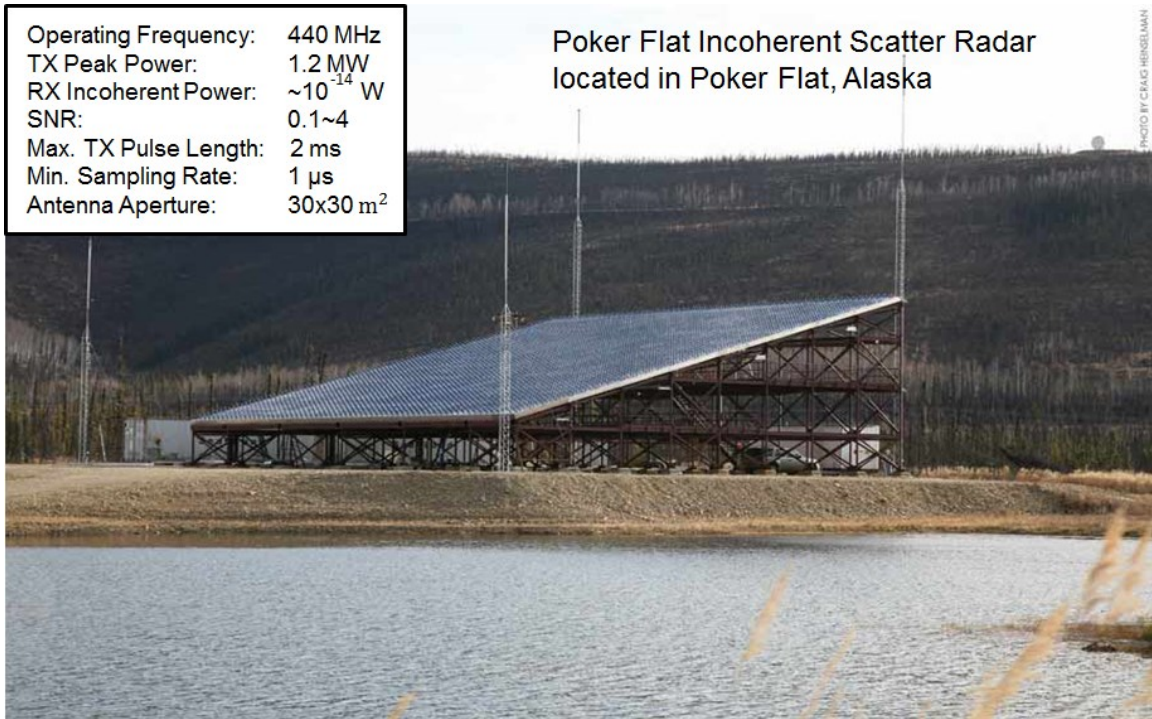


Figure 2.9. Poker Flat incoherent scatter radar (PFISR) located in Fair Banks, Alaska.
(Photo by Craig Heinselmann)

2.3.2 Incoherent Scatter Radar Signal Processing

1. Range-Time Diagram

In the previous section the theory of incoherent scattering was briefly mentioned. It was mentioned that the information on the plasma parameters is confined in the frequency spectrum of the scattered signal. Measuring this spectrum via incoherent scatter radars, however, is not straightforward and requires employment of sophisticated signal processing methods. Figure 2.10 illustrates a simple schematic of ISRs operation in a

format that is often called the range-time diagram. ISRs transmit electromagnetic pulses toward the ionosphere that propagate in range (distance) with the speed of light (c). This propagation is represented by the tilted lines in the range-time diagram that has a slope $m = \pm c$. Note that ISRs do not necessarily transmit pulses vertically (90 degrees elevation angle) with respect to the surface of the earth and the transmission direction may have any elevation angle. For any given elevation angle α , range and altitude have a simple relation in the form $altitude = range \times \sin \alpha$. For simplicity here we consider the case of 90 degrees elevation angle.

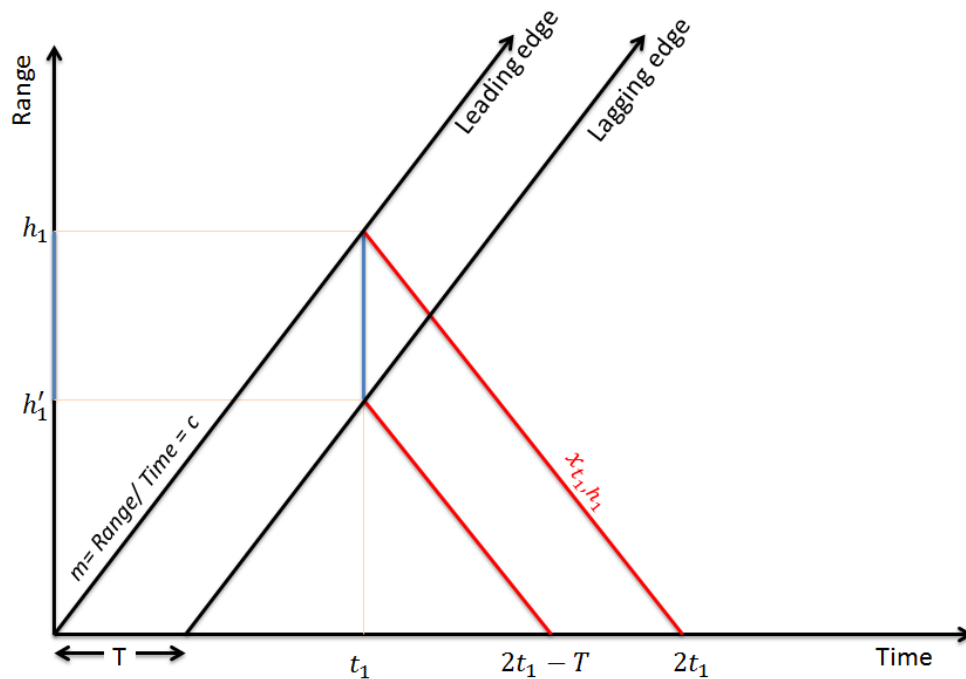


Figure 2.10. Range-time diagram of ISRs.

At any given time $t = t_1$ after the start of the transmission of a pulse, the leading edge (or the onset of the pulse) reaches to the altitude $h_1 = ct_1$ and the lagging edge (or the offset

of the pulse) reaches to the altitude $h'_1 = c(t_1 - T)$, where T is length of the transmitted pulse. At this moment the entire plasma confined in the volume defined by h_1, h'_1 , and the angular width of the main lobe of the radiation pattern of the radar is being illuminated by the radar pulse and thus causes scattering. For simplicity assume that the angular width of the main lobe of the radiation pattern is sufficiently small that we can approximate the geometry as one-dimensional. Let us define the scattered signal from a single altitude h_1 at time t_1 as x_{t_1, h_1} . This signal propagates towards the radar with the speed of light and is detected in a single digital sample at time $2t_1$. Similarly, scattered signals from other altitudes in the range h_1 to h'_1 propagate downward and get to the radar at earlier times. For instance the scattering from the lagging edge of the pulse is detected at time $2t_1 - T$.

By the time $t_2 = t_1 + \frac{T}{2}$ the pulse has propagated to higher altitudes with the leading edge at $h_2 = c\left(t_1 + \frac{T}{2}\right)$ and the lagging edge at $h'_2 = c\left(t_1 - \frac{T}{2}\right)$; whereas scattered signal x_{t_1, h_1} has propagated downward to altitude h'_2 . At this time, x_{t_1, h_1} adds to the instant scattering of the lagging edge at h'_2 , that is x_{t_2, h'_2} . The two scattered signals continue to propagate downward to the radar site and will be detected simultaneously in a single digital sample at time $2t_1$. This is shown in Figure 2.11. By investigating Figure 2.11 and applying the same argument but for intermediate times between t_1 and $t_2 = t_1 + \frac{T}{2}$ it is straight forward to show that the digital sample received at time $2t_1$ contains contributions not only from the two altitudes $h_1 = ct_1$ and $h'_2 = c\left(t_1 - \frac{T}{2}\right)$ but also from

the entire range of altitudes in between; that is the entire altitude range that is covered by half of the pulse. No further contribution can occur at altitudes below h'_2 since at time $t_2 = t_1 + \frac{T}{2}$ the radar pulse has entirely propagated to higher altitudes and no longer covers the plasma at lower regions. This coarse range resolution (that corresponds to the spatial extent of half of the pulse) causes ambiguity in identifying the exact range of an infinitely small target that is located between h_1 and h'_2 and contributes to the sample received at time $2t_1$. This ambiguity can be mathematically described through a concept called the *ambiguity function* [Farley 1969; Sulzer, 1986; Lehtinen and Häggström, 1987; Lehtinen and Huuskonen, 1996].

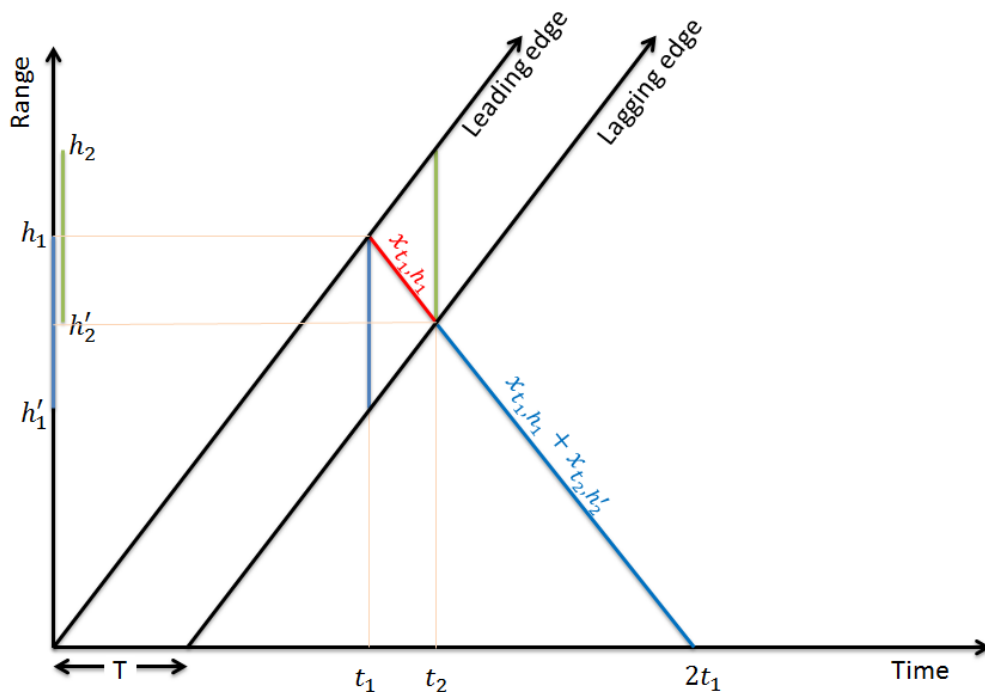


Figure 2.11. Range-time diagram of ISRs.

The scattering occurs continuously as the radar pulse continues to propagate in the ionosphere. However, ISRs, like any other digital system, measure digital samples of continuous signals. This is shown in Figure 2.12. By investigating this figure it can be seen that sample t_{i+1} originates from a scattering volume that is higher in altitude by $c \frac{\Delta t}{2}$ relative to the scattering volume that contributes to the received sample at time t_i . Here Δt is the radar sampling interval. The consecutive samples measured by the radar, therefore, represents not only the time variations in the plasma but also the range or altitude variations of the center of the scattering volume. This is the concept that enables ISRs to provide in-range measurements from the ionosphere.

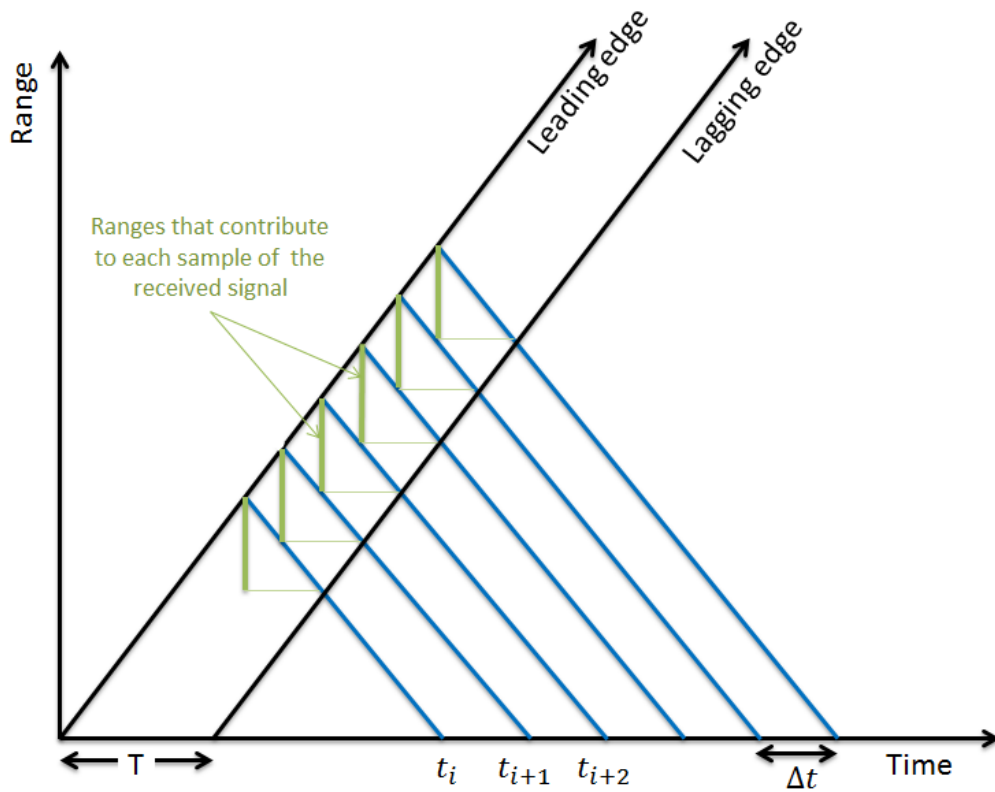


Figure 2.12. Range-time diagram of ISRs.

2. Autocorrelation Function

As mentioned before, the information on the bulk plasma parameters are contained in the shape of the ion line spectrum, i.e. the double-humped spectrum shown in Figure 2.8. ISRs, in fact, measure the autocorrelation function of the received signal, which is the inverse Fourier transform of the incoherent scatter spectrum. The autocorrelation function of a square-integrable signal $x(t)$ is defined as:

$$ACF(x(t)) = R_{xx}(\tau) \equiv \int_{-\infty}^{+\infty} x(t)x^*(t - \tau)dt \quad (2.17)$$

Where the operator $*$ means complex conjugate and τ is called the time lag or simply lag. The power spectral density and the autocorrelation function of a signal are related according to the relations:

$$S(x) = \int_{-\infty}^{+\infty} R(\tau)e^{-j2\pi f\tau}d\tau \quad (2.18)$$

$$R(\tau) = \int_{-\infty}^{+\infty} S(f)e^{j2\pi f\tau}df \quad (2.19)$$

For discrete stochastic signals, such as the incoherent scatter radar signal, the discrete autocorrelation function is defined as:

$$ACF(x[n]) = R_{xx}(l) \equiv \langle x[n]x^*[n - l] \rangle \quad (2.20)$$

Where $\langle \rangle$ represents ensemble averaging over many realizations of the stochastic process $x[n]$ and l is the discrete lag.

The length of the autocorrelation function of a signal (the time span during which the autocorrelation function is non zero) is called the correlation time. For the ISR signal in the ion line channel the correlation time is the time after which motions of plasma particles that are involved in generating ion acoustic waves are no longer correlated with those in the beginning of the time span. For the ionospheric F region plasma this correlation time is of the order of hundreds of microseconds. Therefore, for typical ISR experiments, 330 or 480 microsecond pulses are often used in order to measure the autocorrelation function for lags as large as the correlation time.

In Figure 2.12, assuming x_i is the signal received at time t_i from a volume of plasma centered at altitude h_i , the zeroth lag ($l = 0$) of the autocorrelation function for the corresponding altitudes is $x_i x_i^*$. Since x_i is associated with an ambiguity function the zeroth lag is also, inevitably, associated with a similar ambiguity function. Similarly, we can calculate the higher lags of the discrete autocorrelation function according to $R_{xx}(l = n\Delta t) \approx \langle x_i x_{i+n}^* \rangle$. Deriving the higher lags, however, become more complicated because of the fact that samples x_i and x_{i+n} do not correspond to the same range and scattering plasma. Consider an ISR experiment in which a 480 μs pulse is used and the scattered signal is sampled every 30 μs . Considering the speed of light, the length of the ambiguity function for each sample (the spatial extent of half of the pulse) is 72 km. Now for $t_{i+1} = t_i + 30 \mu s$, we have $h_{i+1} = h_i + 4.5 \text{ km}$ and in general $h_{i+n} = h_i + n \times 4.5 \text{ km}$. Therefore, the ambiguity functions of two consecutive samples have 67.5 – km in common.

If we assumed that the motions of electrons and ions at different altitudes are to a good degree independent from each other (since charged particles in different locations are subject to independent and uncorrelated forces), signals originating from different ranges are, essentially, uncorrelated and would produce zero contributions to the lags of the autocorrelation function. Therefore, once two received samples (x_i and x_{i+n}) in Figure 2.12 are used to calculate a lag of the autocorrelation function, only the portion of the plasma that the two samples have in common contributes to the lag and, as such, the ambiguity function of the corresponding lag is defined by the common volume. In this ISR experiment, the length of the ambiguity function of each lag decrease by 4.5 km relative to the previous lag. As a result, while a 72-km long plasma contributes to the zeroth lag only a 4.5-km long plasma contributes to the fifteenth lag. This causes unwanted weights on the amplitude of the different lags and causes errors in measuring the autocorrelation function. A number of methods have been introduced in order to increase the accuracy of the autocorrelation function measurements, however, a detailed understanding of this topic requires mathematical approaches to the concept of ambiguity functions and such discussions are beyond the scope of this introductory section. Interested readers are referred to *Farley* [1969], *Sulzer* [1986], *Lehtinen* and *Hägström* [1987], and *Lehtinen* and *Huuskonen* [1996].

In deriving the autocorrelation function of the ISR received signal one issue was ignored and that is the ensemble averaging over many realizations that is a part of the definition of the autocorrelation function. In practice ISRs transmit multiple pulses and the scattered signals from individual pulses and from the same altitudes are averaged in order to

measure the average behavior of the plasma (the autocorrelation function). This is shown in Figure 2.13. In ISR experiments averaging over hundreds of pulses is often required.

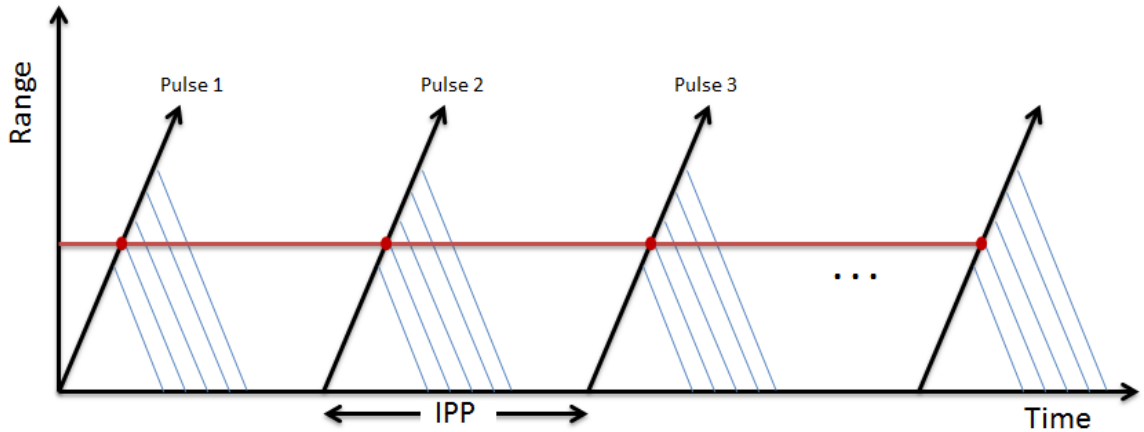


Figure 2.13. Range-time diagram of ISRs: averaging over many radar pulses.

In Figure 2.13 the term *IPP* refers to inter pulse period. *IPP* cannot be arbitrarily small. In order to transmit the next pulse one must wait until the previous pulse has completely left the ionosphere, otherwise, both pulses would contribute to radar's received signal at any given time. This, in turn, causes ambiguity in the origin of the received signal. In practice, the intensity of the scattered signal from above ~ 800 km is so small that this altitude can be practically considered as the end of the ionosphere. Moreover, *IPP* cannot be arbitrarily large since the entire averaging period should be short compared to the timescales in which the ionosphere changes in order to meet the assumption that the stochastic process remains stationary.

Figure 2.14 shows an example of what an ISR measures. This plot (produced by averaging over several minutes during which hundreds of pulses of length $480 \mu s$ have

been sent) shows the ion line spectra as a function of altitude. Horizontal cuts of this figure at any altitude produce the double-humped ion line spectra that resemble the theoretical spectra. It is seen that the offset frequency of the two humps increases at higher altitudes. This increase in the width of the spectrum corresponds to the decrease in the ion mass and increase in the ion temperature at higher altitudes.

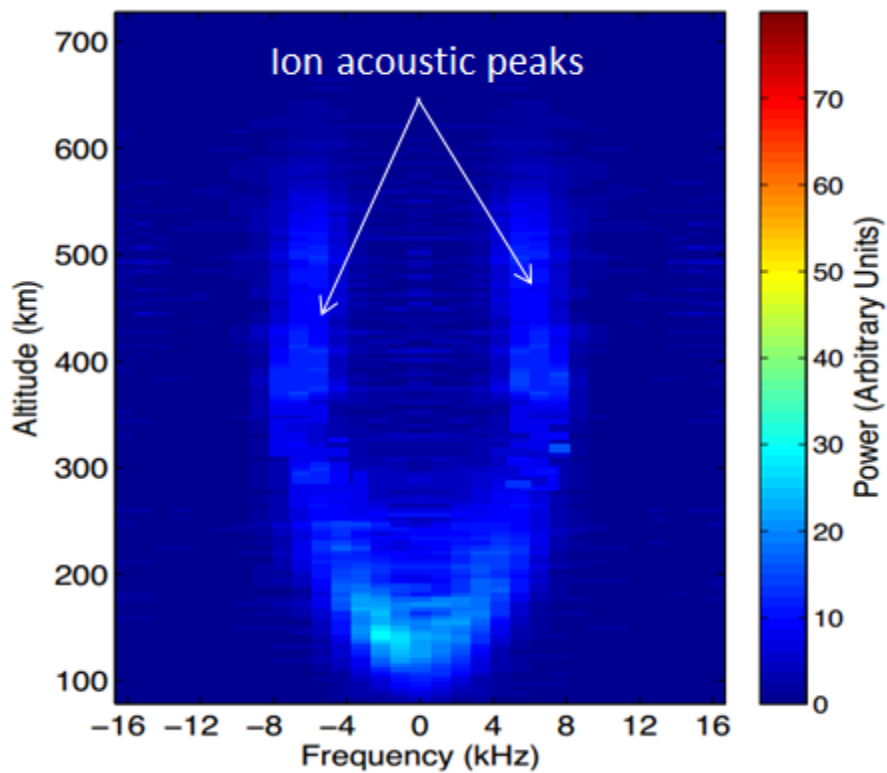


Figure 2.14. An example of the ion line spectra as a function of altitude measured by an ISR.

By integrating the power spectral density with respect to frequency one can derive the intensity of the scattered signal as a function of altitude. By repeating this process at different times one can produce the range-time-intensity plot shown in Figure 2.15. As

mentioned before the intensity of the signal in the ion line channel represents the intensity of the ion acoustic waves that cause the scattering; which, in turn, in a plasma that is in thermal equilibrium is proportional to plasma density. Similar plots can also be produced for each of the plasma line channels.

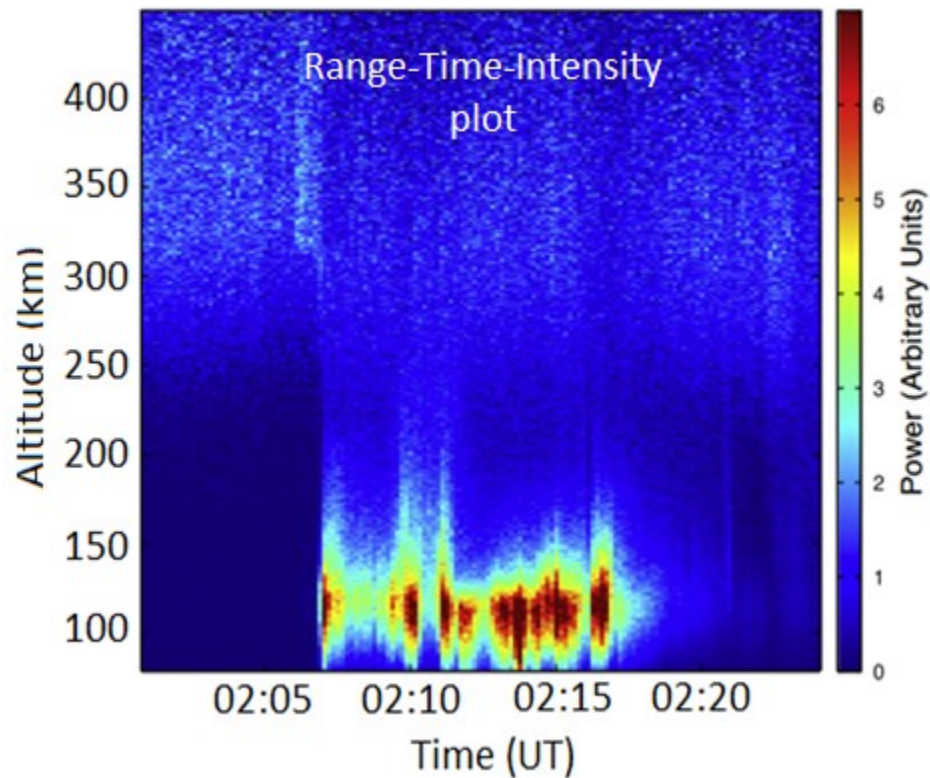


Figure 2.15. An example of the range-time-intensity plot measured by an ISR. The enhanced signal below 200 km represents enhanced E region ionization due to energetic (keV) electron precipitations. (Plot from *Michell et al.* [2014])

3. Phased-Array ISRs and Pulse Coding Techniques

Phased-array ISRs, for instance the Poker Flat ISR (PFISR) that is built based on the advanced modular incoherent scatter radar (AMISR) technology, are capable of electronically steer the pointing direction of the main lobe of the radar's radiation pattern in time scales of milliseconds. This enables the radar to transmit a single pulse in a specific direction, receive the scattered signal, and rapidly transmit the next pulse in a different direction. Employing multiple transmission directions, or radar beams enables the radar to produce volumetric maps of the plasma parameters in the ionosphere. An example of such volumetric maps is shown in Figure 2.16 that shows the ion temperature as a function of the three spatial dimensions. Employing many radar beams (directions), however, expectedly leads to a tradeoff. Because of the variability of the ionosphere and the need to meet the stationarity requirement during the averaging period, the maximum averaging period in each direction is limited. For a fixed averaging interval, thus a fixed number of transmitted pulses, an increase in the number of radar beams results in a decrease in the number of pulses that are sent in each direction. This, in turn, leads to a lower statistical accuracy of measurements and a lower signal to noise ratio. In a practical ISR experiment a variety of such tradeoffs exists and needs to be addressed.

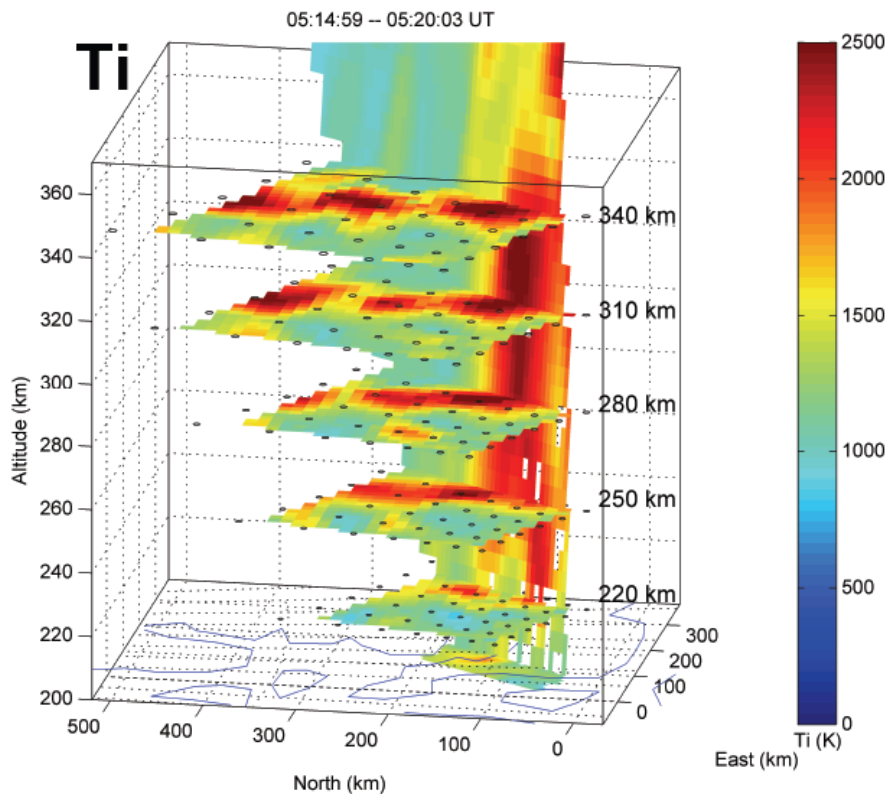


Figure 2.16. An example of a volumetric image of the ionosphere using the phased-array PFISR. The plot shows the ion temperature as a function of the three spatial dimensions. (Plot from *Perry et al.*, [2015])

It was discussed before that the length of the ambiguity function, that is determined by the length of the pulse, and not the sampling rate determines the range resolution of ISR measurements. This means, the longer the pulse, the coarser the range resolution. On the other hand, the transmitted pulse needs to be longer than the plasma correlation time in order to measure the ISR spectrum. A variety of complex pulse coding techniques have been developed in order to increase the range resolution and yet measure the entire ion line spectrum. In such techniques, the transmitted long pulses are phase or amplitude

coded and the received signals are subject to post processing and decoding. Some pulse coding methods that are often used in ISR experiments are Alternating codes [Lehtinen and Haggstrom, 1987; Sulzer, 1993], Barker Codes, and multi-pulse coding [Farley, 1972].

Figure 2.17 shows a set of pulses that compose a four bit alternating code. In an ISR experiment a full cycle of alternating code (in this example a full cycle includes 8 pulses) are send. A careful processing of the received signals from the transmitted cycle, each weighted by ± 1 coefficients, is then used to achieve a better range resolution. The basic idea is to add and subtract scattered signals from each pulse of the cycle in a way that all except one of the bits cancel each other's contributions, leaving only a small fraction of the pulse that effectively contributes to the received signal. For instance, adding all eight pulses in Figure 2.17 with +1 coefficients results in cancelation of all but the first bit. Employing different sets of coefficients should also lead to a similar effect but for different bits of the code. Note that the presented picture here is greatly oversimplified. In fact, the cancelation needs to happen in the domain of ambiguity functions for different lags of the autocorrelation function. The true processing underlying such pulse compression techniques requires detailed considerations that are beyond the scope of this thesis; interested readers are referred to Sulzer [1986], Lehtinen and Haggström [1987], and Lehtinen and Huuskonen [1996].

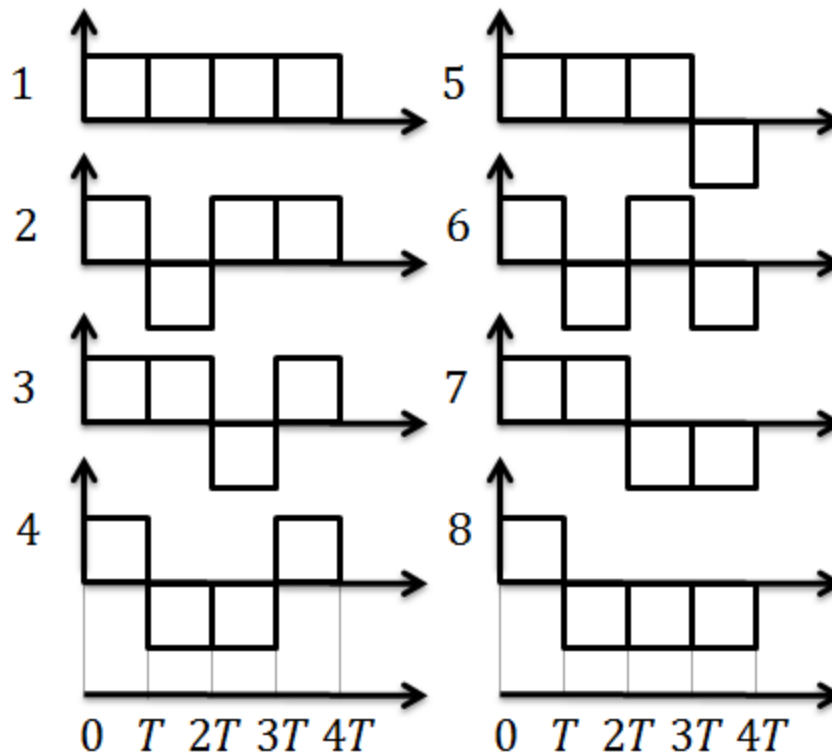


Figure 2.17. A set of pulses that compose a four bit alternating code (AC).

A portion of the ISR results presented in this thesis is obtained by employing a 16-bit alternating code (full cycle includes 32 pulses). In such experiments 480-microsecond pulses, each composed of 16 bits (each bit is 30 microsecond long), provide a range resolution of 4.5 km. The finer range resolution that is obtained by employing coded pulses comes with a price. The usage of coded pulses produces clutter (unwanted signal that is produced during post signal processing). Clutter, in turn, reduces the signal to noise ratio and decreases the statistical accuracy of coded pulse measurements relative to a simple uncoded long pulse.

2.4 Naturally Enhanced Ion Acoustic Lines (NEIALs)

Incoherent scatter radars (ISRs) are designed to sense the weak thermal fluctuations in the ionospheric plasma, and as such are highly sensitive to plasma instabilities and the coherent structures they produce. At high latitudes, the presence of free energy in a variety of forms commonly drives the ionosphere out of stability. ISR measurements of the ion and plasma lines from these regions, therefore, occasionally show characteristics not accounted for in standard ISR theory (e.g., *Foster et al.*, [1988], *Michell and Samara*, 2010, *Akbari et al.*, [2012, 2014]). In the ion line measurements, for radar beam directions close to parallel to the magnetic field lines, sometimes strong echoes appear that are enhanced by orders of magnitude above the thermal level. Figure 2.18 shows an example. Here the received radar power in the ion line channel is shown as a function of time and altitude. Strong echoes can be seen between 100 (km) and 600 (km). The echoes are often up to 4–5 orders of magnitude more intense than the signals from a thermal plasma, short-lived (lasting for tens of seconds), and consist of intensity variations with sub-second times scales.

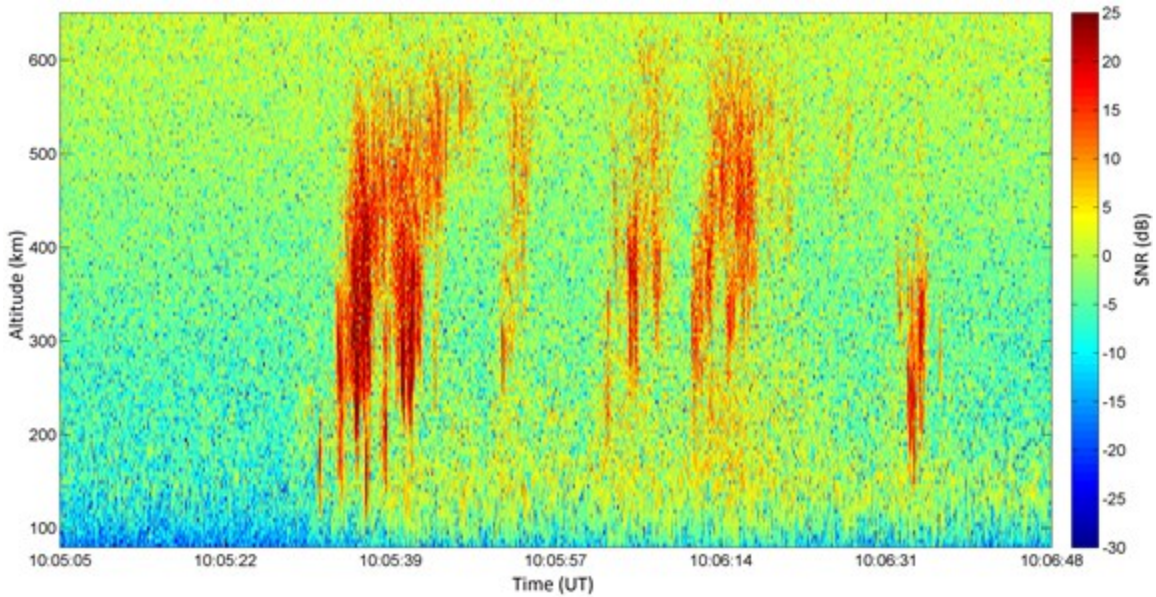


Figure 2.18. An example of the range-time plot from the ion line channel measurements. The enhanced echoes from 100 (km) to 600 (km) are produced by destabilized ion acoustic waves and are called naturally enhanced ion acoustic lines (NEIALs). (Plot from *Akbari et al. [2014]*)

The echoes have a distinct signature in the frequency domain where one or both shoulders of the thermal double-humped spectrum (see Figure 2.14) are considerably enhanced. Figure 2.19 shows an example. Localization of the increased received power at the expected frequency of the ion acoustic peaks, thus, confirms that such echoes are the result of scattering by destabilized ion acoustic waves. Hence, the name ‘naturally enhanced ion-acoustic lines’ (NEIALs) has been used to refer to these echoes. The term ‘naturally’ represents the fact that the source of free energy for destabilizing the ion acoustic waves is provided by the nature. Ion acoustic waves can also be enhanced to high amplitudes and produce similar echoes in ISR data in ionospheric modification

experiments [Carlson *et al.*, 1972]. In such experiments an artificial intense electromagnetic pulse is used to derive the ionosphere out of stability rather than natural sources of energy. Sedgemore-Schulthess and St. Maurice [2001] provides a good review on NEIALs.

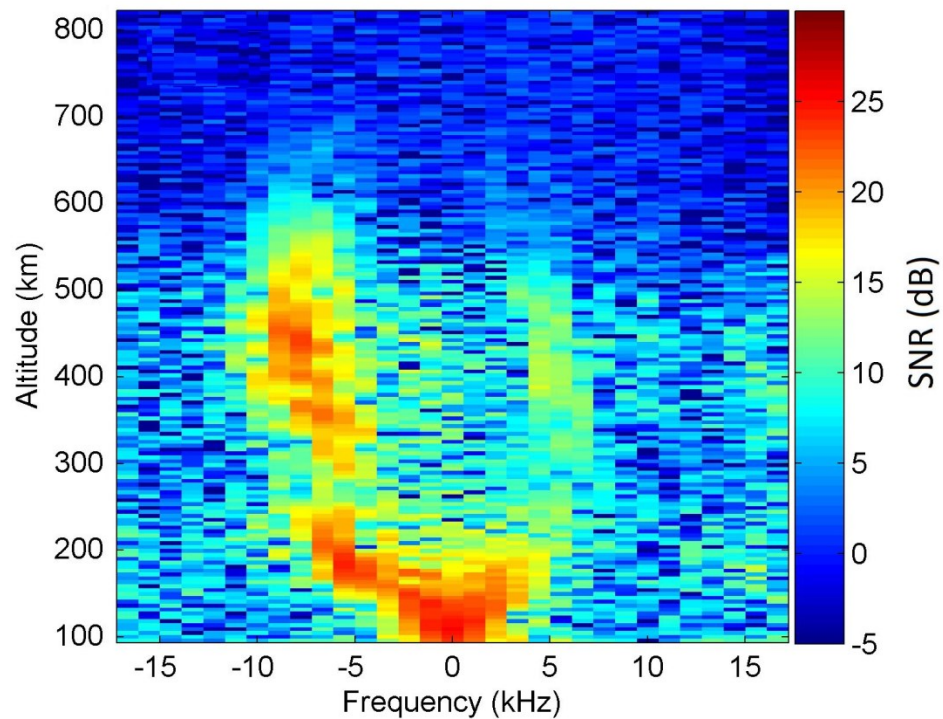


Figure 2.19. The typical form of NEIALs in the frequency domain. Here the down-shifted shoulder, corresponding to the ion acoustic waves propagating away from the radar, is enhanced above the thermal level. (Plot from Akbari *et al.* [2014])

Similar natural echoes can also be seen from the E region in radar beam directions close to perpendicular to the magnetic field lines [St.-Maurice *et al.*, 1989; Foster and Erickson, 2000]. For such cases the generating mechanism is understood to be Farley-

Buneman waves generated when ambient electron drift exceeds a threshold. The focus of this thesis is, however, NEIALs that are observed in radar beam directions close to parallel to the magnetic field lines. The importance of investigating NEIALs relies on the fact that NEIALs are signatures of a process that is linked to many phenomena in the magnetosphere-ionosphere system (such as auroral precipitations, wave-wave, and wave-particle interactions, ion outflow, and in general the dynamics of the high-latitude ionosphere) and is yet not fully understood. The main open issues regarding NEIALs are their generation mechanism and the underlying source of free energy.

Different mechanisms have been proposed to explain the destabilization of ion acoustic waves and generation of NEIALs. Proposed mechanisms are of two types (1) streaming instabilities due to relative drifts between different species of plasma particles and (2) wave-wave interactions where a destabilized primary Langmuir wave gives rise to enhanced ion acoustic waves [Forme 1993, 1999; Strømme *et al.*, 2005]. The wave-wave interaction route to destabilize ion acoustic waves will be discussed under the context of beam-plasma interactions and Langmuir turbulence in the next section. Here we briefly discuss the basic physics behind the streaming instabilities.

Streaming instabilities are one of the main categories of instabilities in plasma physics. They emerge when either a beam of charged particles or current is driven through a plasma so that the different species have different drifts relative to one another. The kinetic energy of the drifting particles provides the energy to excite waves and the oscillations grow at this expense. For a simple case consider a uniform plasma in which

the ions are stationary and the electrons have a velocity v_0 relative to the ions. If the natural frequency of oscillations in the electron fluid is ω_p , the natural frequency of oscillations for ions will be $\Omega_p = \left(\frac{m}{M}\right)^{\frac{1}{2}} \omega_p$ where m and M are the electron and ion masses, respectively. Because of the Doppler shift of the oscillations in the moving electron fluid (ω_p), these two frequencies can coincide in the stationary frame if certain condition on the drift velocity of the electrons is met. Moreover, it can be shown that the existence of oscillations in the drifting electrons decreases the total kinetic energy of the electrons to a lower amount than $\frac{1}{2} m n_0 v_0^2$ which is the total kinetic energy in the absence of any oscillations (here n_0 is the number density of electrons). Therefore, the electron oscillations can be considered to effectively have negative energy while ions oscillations have positive energy. Consequently, both electron and ion oscillations can grow together while keeping the total energy of the system constant (see Chapter 6 of *Chen* [1984]).

The scenario described above is sometimes called electron-ion streaming instability. This mechanism has been proposed to explain the enhanced ion acoustic waves seen by ISRs in the high-latitude ionosphere [*Rietveld et al.*, 1991; *Collis et al.*, 1991]. According to this mechanism, after being collisionally stopped at the F region altitudes, soft electron precipitations (precipitating electrons with energies of hundreds of eV) result in accumulation of charge, which in turn results in generation of field-aligned electric fields that accelerate thermal electrons to higher and lower altitudes. The resulting electric current due to the thermal electrons then destabilizes ion acoustic waves.

One difficulty with this mechanism, however, is that the current density that is needed to destabilize ion acoustic waves (of the order of several milliamps per square meter [Collis *et al.*, 1991]) is higher than the field aligned current densities carried by thermal electrons that have ever been directly measured via space-borne instruments in the ionosphere. However, it was later proposed that such high current densities are not, necessarily, unreasonable if the width of the current layer is small [Rietveld *et al.*, 1991; Collis *et al.*, 1991]. Assuming this model St.-Maurice *et al.* [1996] proposed intense parallel electric fields of up to a few hundred microvolts per meter with perpendicular scale of a few hundred meters or less could produce the required current needed to destabilize ion acoustic waves. It should be mentioned that using interferometric methods Grydeland *et al.*, [2003, 2004] showed that the size of the structures producing NEIALs were in fact on the order of few hundred meters in the direction perpendicular to the magnetic field lines at 500 km.

For streaming instabilities to initiate, the drifting particles do not necessarily have to be electrons. Wahlund *et al.* [1992] has proposed that different species of ions (for instance O^+ and H^+) in the ionosphere can have drifts relative to each other and that can provide the energy to destabilize the ion acoustic waves and produce NEIALs. This mechanism is often called the ion-ion two stream instability. Observations of NEIALs simultaneous with observations of bulk motion of ions in the ionosphere (ion outflows) have been used to argue in the favor of the ion-ion two stream instability model for generating NEIALs [Wahlund *et al.*, 1992]. According to this model the presence of large electric fields on the edge of auroral precipitations leads to frictional heating of ions as they move ($E \times B$

drift) through the neutral gas. The increased ion temperature leads to strong pressure gradients that, in turn, force the ions up the field lines. The different species of ions (with different masses) experience different accelerations which causes the relative drifts between the species of ions at higher altitudes. This mechanism, however, needs clarifications on the processes that can cause the relative drifts between the different species of ions in the E region of ionosphere in order to explain the NEIALs that are observed at altitudes as low as 150 (km). That is because the high rate of collisions in the E region prevents ions from having relative drifts and thus the ion-ion two stream instability might not be a valid candidate to explain the NEIALs observed in the E region.

Recently, a new mechanism has been introduced in order to explain the destabilization of ion acoustic waves in the ionosphere, which includes acceleration of electrons by ion cyclotron waves [*Bahcivan and Cosgrove, 2008*]. This mechanism, however, needs to be compared with the ISR observations to determine to what extent it is consistent with the variety of measurements.

2.5 Beam-Plasma Interactions and Langmuir Turbulence

2.5.1 Beam-Plasma Interactions

Under the context of this thesis an electron beam is defined as a population of electrons streaming in a plasma where the ratio of the velocity spread within the streaming population to the average velocity of the population is limited so that the streaming

electrons appear as a peak in the electron velocity distribution function. Figure 2.20 shows an example of a distribution function that consists of background thermal electrons and an electron beam.

A plasma wave propagating with phase velocity $v_\phi = \frac{\omega}{k}$, where ω and k are frequency and wave number of the wave, exchanges energy with the electrons that propagate with velocities $v \approx v_\phi$. While the electrons with velocities slightly greater than the phase velocity of the wave lose energy to the wave, electrons with velocities slightly lower than the phase velocity of the wave take energy from the wave causing the waves to damp. This is called Landau damping (see Chapter 7 of *Chen* [1984]). In any plasma with a stable electron distribution the number of electrons decreases with increasing energy. This is evident from the negative slope of the one-dimensional distribution function. As a result the amount of energy transferred from plasma waves to electrons is always greater than the amount of energy that is transferred from electrons to plasma waves. This situation, however, changes in the presence of an electron beam that produces a local positive slope in the one-dimensional distribution function. This provides the possibility for plasma waves to grow at the expense of the beam energy through a process called bump-on-tail instability (see Chapter 7 of *Chen* [1984]). Note that such a mechanism is different in nature from the streaming instabilities discussed in Section 2.4. That is because such a beam-plasma interaction is purely a kinetic process while streaming instabilities can be described by the fluid equations.

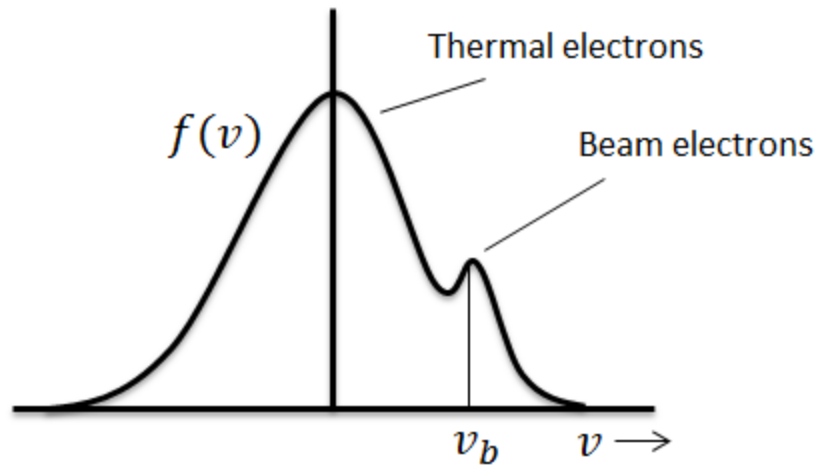


Figure 2.20. An example of an unstable one-dimensional electron distribution function consisting of background thermal electrons and an electron beam. The positive slope of the distribution function leads to growth of plasma waves.

When introducing the Vlasov equation it was mentioned that the electric field of plasma waves can modify the distribution of charged particles in physical space or velocity space. In the case of beam-plasma interactions, upon growing to high intensities the generated plasma waves may cause diffusion of beam electrons in velocity space. The diffusion occurs in the direction of flattening the positive slope and removing the source of free energy. Once the flattening happens the kinetic energy of the beam electrons is no longer available to plasma waves and the growth of the waves ceases. The theory that describes the evolution of the distribution function in the presence of plasma waves is called quasilinear theory [Vedenov *et al.*, 1962]. Figure 2.21 (from Muschiatti [1990]) presents results from a quasilinear simulation that shows the evolution of an electron

distribution function that initially appeared as a beam distribution, as the intensity of the plasma waves increases.

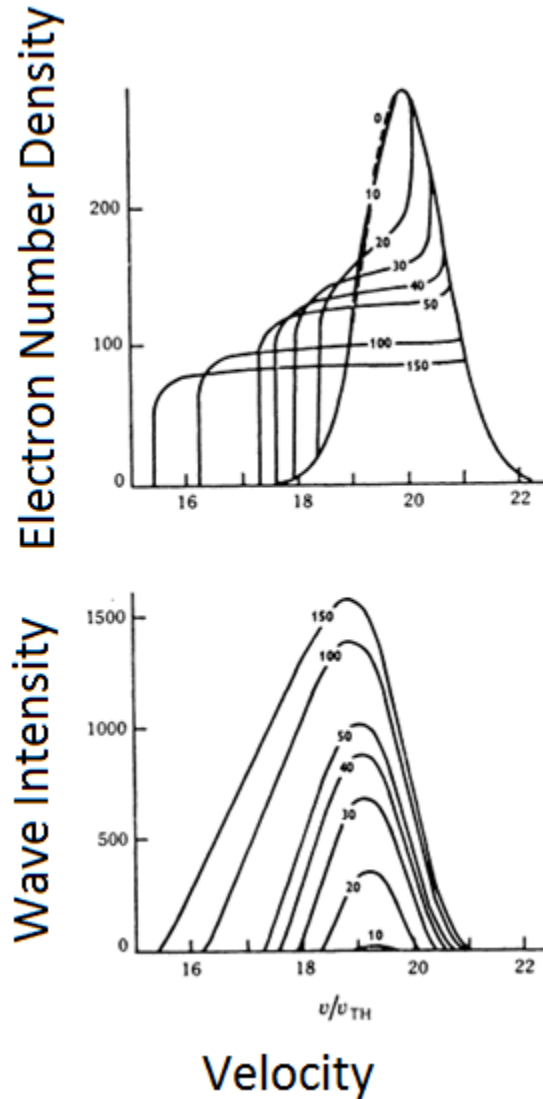


Figure 2.21. Quasilinear diffusion: simulation results from *Muschiatti* [1990] showing the evolution of an electron distribution function (top) and plasma wave intensity (bottom). Numbers on the curves are times (in milliseconds) after the start of the simulation. It can

be seen that once the plasma waves grow to higher intensities they react back on the distribution function to flatten the positive slope and remove the source of free energy.

Particle measurements with instruments on board of rockets during periods of intense electron precipitations have shown that electron distribution functions in the F region ionosphere often consist of plateaus rather than positive slopes. This implies that the electron distributions could be unstable at higher altitudes but are stabilized by the quasilinear diffusion as the electron beams continue to propagate to lower altitudes. Figure 2.22 (from *Kaufmann et al.* [1978]) shows one example of such electron distributions that was measured at altitude of ~ 250 (km).

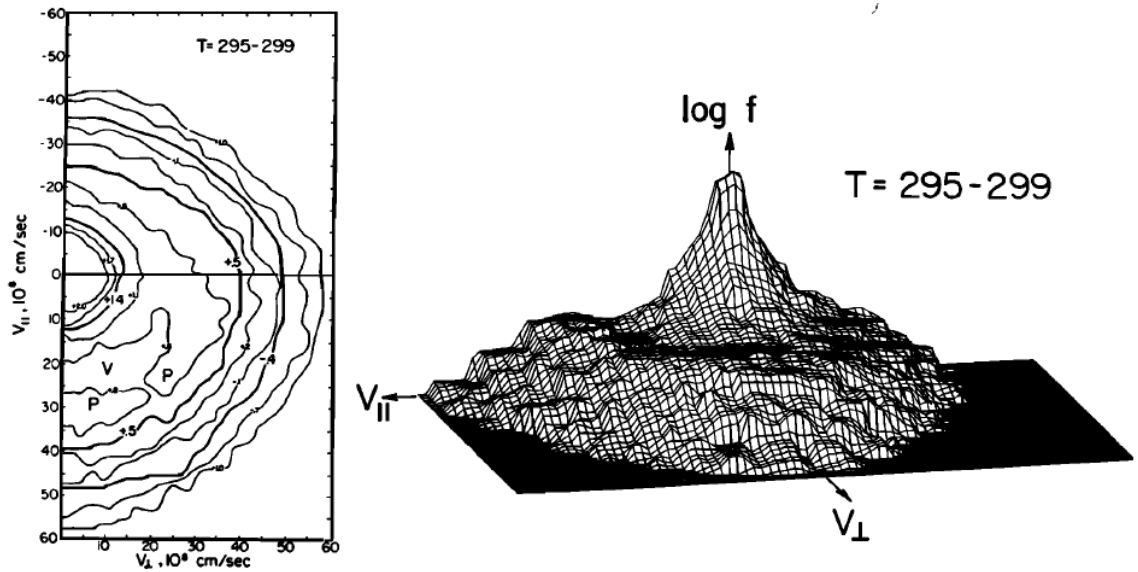


Figure 2.22. An electron distribution function measured by instruments on board of a sounding rocket at altitude of ~ 250 (km). The distribution function consists of a plateau

implying that the quasilinear diffusion has stabilized the distribution function at higher altitudes. (Plot from *Kaufmann et al.* [1978])

The quasilinear diffusion has been shown to flatten the positive slope of the electron distribution function in short time scales (see *Papadopoulos and Coffey* [1974] and references therein). This time scale is in the order of milliseconds for the plasma parameters at about 1000 km and in the order of tens of millisecond for the plasma parameters at 300 km. Stability of an electron beam (i.e. maintaining the positive slope of the distribution function) against the quasilinear diffusion as the electron beam propagates from its acceleration point (altitude of 6000–10000 km) to the F region of the ionosphere is still subject to research. Electron beam stability has also been the subject of many discussions in the context of satellite measurements of plasma waves in the solar wind (see *Muschiatti* [1990] and references therein).

Nonlinear wave-wave interactions have been proposed as a possible mechanism that can work against the quasilinear diffusion in order to stabilize the beam distribution [*Papadopoulos and Coffey*, 1974]. This mechanism is illustrated in Figure 2.23. According to this mechanism while the positive slope of the distribution function leads to intensification of plasma waves that are directly in resonance with the beam electrons at the region of positive slope (the region labeled r_1 in Figure 2.23), nonlinear wave-wave interactions may quickly remove the energy from the initial waves by transferring the energy to waves that are not directly in energy exchange with the beam particles (waves in the region labeled r_2). If the rate of energy transfer out of region r_1 by wave-wave

interactions is greater than the rate of injection of energy into region r_1 by the positive slope of the beam, waves in region r_1 cannot grow to high intensities to react back on the distribution function and plateau the positive slope. This mechanism, however, depends highly on parameters of the electron beam and background plasma and on the nature of the wave-wave interactions.

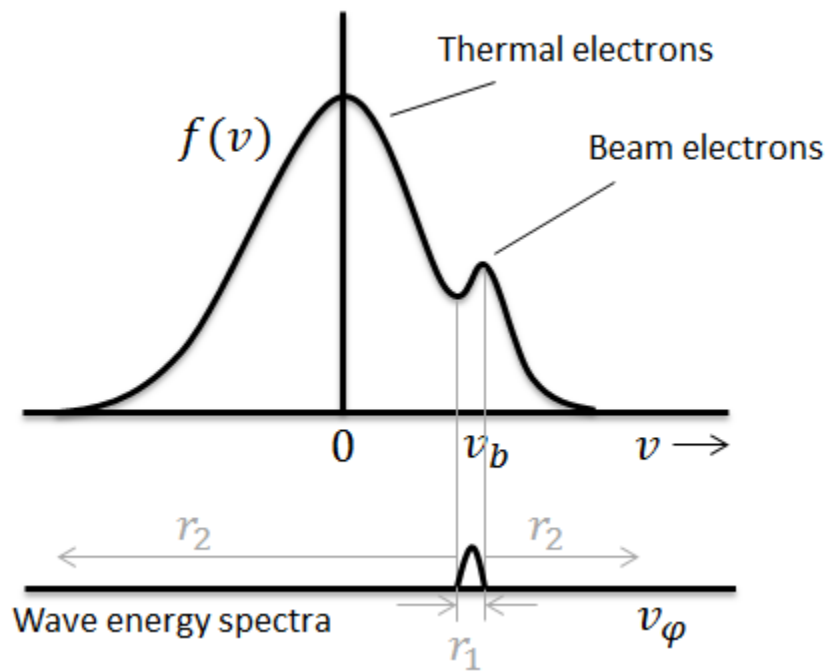


Figure 2.23. Nonlinear wave-wave interactions have been proposed as a plausible mechanism that can stabilize electron beam distributions against the quasilinear diffusion.

Any wave-wave interaction requires at least three participating waves since the conservation of energy and momentum may not be satisfied with only two waves. As an example consider a three wave interaction where a coalescence of two plasma waves W_1 and W_2 produces a new product wave W_3 ($W_1 + W_2 \rightarrow W_3$). Conservation of energy

and momentum requires $\omega_1 + \omega_2 = \omega_3$ and $k_1 + k_2 = k_3$, respectively. Rewriting the two equations in the vector form we have $\begin{bmatrix} \omega_1 \\ k_1 \end{bmatrix} + \begin{bmatrix} \omega_2 \\ k_2 \end{bmatrix} = \begin{bmatrix} \omega_3 \\ k_3 \end{bmatrix}$. Now, if on the $\omega - k$ plane the three vectors lie on dispersion curves of natural modes of plasma the interaction have a chance to proceed. This is schematically illustrated in Figure 2.24 where coalescence of an ion acoustic wave (W_1) and a Langmuir wave (W_2) can produce an additional Langmuir wave (W_3).

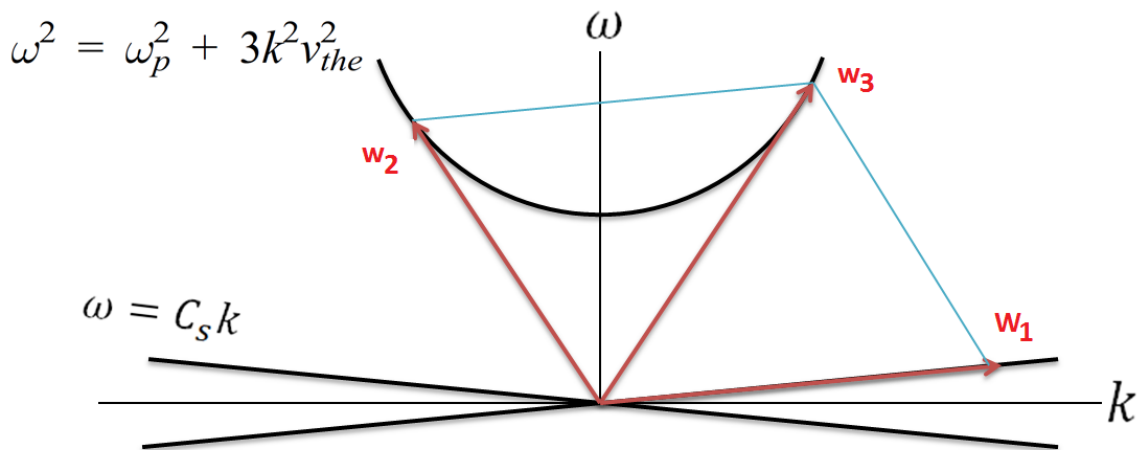


Figure 2.24. Three-wave coalescence of an ion acoustic wave (W_1) and a Langmuir wave (W_2) to produce a product Langmuir wave (W_3). The equations are the dispersion relations for the ion acoustic mode and the Langmuir mode.

Note that kinematically this interaction can go in a reverse direction where an initial Langmuir wave (W_3) decays to produce a secondary Langmuir wave (W_2) and an ion acoustic wave (W_1). This is because the conservation of energy and momentum are the

same for the forward or reverse directions. This later interaction is called the parametric decay instability (PDI), which will be discussed in details in the next sections. Whether the PDI or the three-wave coalescence may proceed depends on their growth rates and on the damping rates for each of the participating waves.

In a very simplified condition, if we assume that the three waves participating in three wave interactions are uniform plane waves, the conservation of energy and momentum can be seen consistent with the following mathematical expression:

$$A_1 e^{j\omega_1 t} e^{-jk_1 x} \times A_2 e^{j\omega_2 t} e^{-jk_2 t} = A_3 e^{j\omega_3 t} e^{-jk_3 x} \quad (2.21)$$

An important point in the above expression is the multiplication (\times), which is a nonlinear operator. Therefore, such wave-wave interactions are nonlinear in nature and thus require existence of a nonlinear mechanism in plasmas to proceed. As will be discussed in the next sections for the case of Langmuir turbulence two nonlinear mechanisms arise from the Ponderomotive force and from the dependence of the plasma frequency on the square root of electron density.

2.5.2 Langmuir Turbulence

Langmuir waves are one of the main plasma waves that will be enhanced in the presence of an electron beam. Once the amplitude of Langmuir waves reaches to high values (~ 1 V/m for the F region plasma parameters) they become unstable and may lead to Langmuir turbulence. Langmuir turbulence is a process that occurs as a result of

nonlinear interactions between Langmuir waves and ion acoustic waves (or ion density perturbations in general). In plasmas the refractive index inversely depends on plasma density. An existing density depression, therefore, forms a region of higher refractive index, which tends to refract the Langmuir waves and thus modify the distribution of their energy in space. On the other hand, the electric field of the Langmuir waves affects the ion density perturbations through its Ponderomotive force, which tends to push the plasma out of the regions of high electric field intensity. As a result of this positive feedback instabilities emerge that lead to strong responses in the electric field and the density perturbations. Such interactions of Langmuir waves and ion density perturbations are thought to exist in a variety of natural and laboratory plasmas covering a huge range of plasma parameters (over 23 orders of magnitude of plasma density, 4 orders of magnitude in electron temperature, and over 15 orders of magnitude in electric field amplitude) [Robinson, 1997]. The free energy for Langmuir turbulence in the ionosphere can be provided by energetic electrons streaming into the ionosphere from the magnetosphere.

The interactions of Langmuir waves and ion density perturbations include the phenomena of linear parametric instabilities as well as the completely nonlinear phenomenon of caviton formation and wave collapse. It was originally shown by Zakharov *et al.* [1985] that parametric instabilities of a monochromatic Langmuir wave are of 5 different types, each with its own threshold, growth rate, and operating regime on the intensity-wave number space. The 5 instabilities are (1) the parametric decay instability (PDI), (2) modulational instability (MI), (3) subsonic MI, (4) supersonic MI, and (5) the modified

decay instability. The applicability regimes of each of these instabilities are shown in Figure 2.25. In this figure $W = \frac{\epsilon_0 |E|^2}{4n_e k_B T_e}$ is the ratio of the electrostatic energy to the plasma thermal energy and k is the wave number. Other quantities are: E , slowly varying envelope of the electric field; ϵ_0 , permittivity of free space; n_e , electron density; k_B , Boltzmann constant; T_e , electron temperature; m_e , electron mass; m_i , ion mass; and λ_D , Debye length. For detailed discussion of the instability regimes readers are referred to the *Robinson [1997]* review paper.

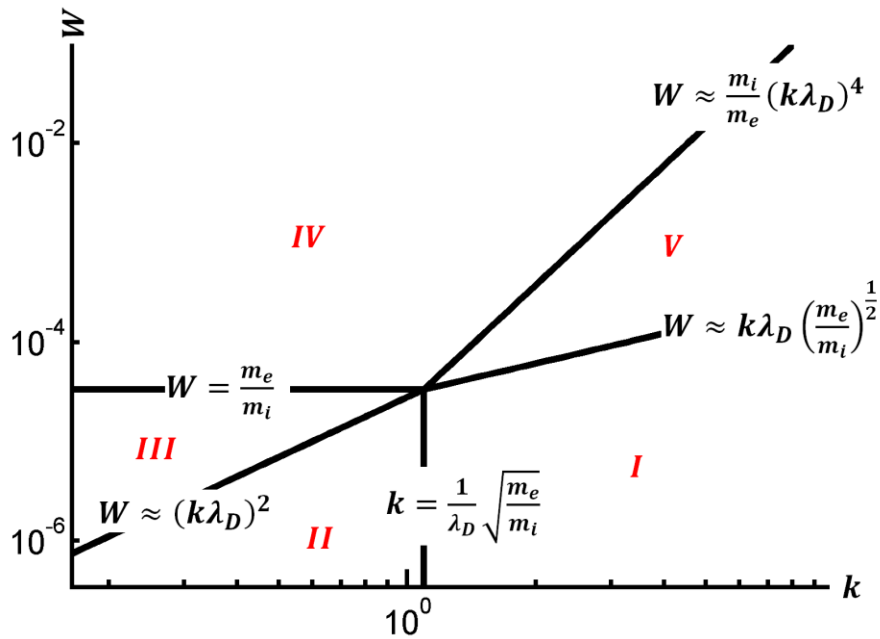


Figure 2.25. Five regimes of linear parametric instability for a monochromatic, plane Langmuir wave with the approximate boundaries derived for the plasma parameters considered in this work. These include. I: parametric decay instability; II: modulational instability; III: subsonic modulational instability; IV: supersonic modulational instability; and V: modified decay instability.

For the typical parameters of the background plasma and electron beams applicable to the ionosphere the initially enhanced Langmuir waves generally fall into the first region where the PDI is the dominant process. As was introduced in Figure 2.24 parametric decay instability is a three-wave process by which a mother Langmuir wave $L_1(\omega_1, \vec{k}_1)$ decays into a daughter Langmuir wave $L_2(\omega_2, \vec{k}_2)$ and an ion acoustic wave $S(\Omega, \vec{K})$. The process happens in three dimensions and the product waves may propagate with angles relative to the mother wave, provided the frequency and wave number matching conditions are met. However, it can be shown that the waves with the highest growth rate are those that satisfy the following conditions: $\vec{K} \approx 2\vec{k}_1 - k^* \hat{k}$ and $\vec{k}_2 \approx -\vec{k}_1 + k^* \hat{k}$ where \hat{k} is a unit vector in the direction of \vec{k}_1 ; which means that the main product Langmuir and ion acoustic waves propagate anti parallel and parallel to the mother wave, respectively. Here $k^* = \frac{2}{3\lambda_D} \left(\eta \frac{m_e}{m_i} \right)^{\frac{1}{2}}$, $\eta = \frac{T_e + 3T_i}{T_e}$, and m_e , m_i , T_e , T_i , and λ_D are electron mass, ion mass, electron temperature, ion temperature and Debye length, respectively. Note that $|\vec{k}_1|$ is larger than $|\vec{k}_2|$ by k^* . Therefore the PDI transfers the Langmuir energy to smaller wave numbers. Upon growing to high intensities the daughter Langmuir wave (L_2) may become unstable and produce its own product waves, transferring energy to yet lower wave numbers. This is shown in Figure 2.26a.

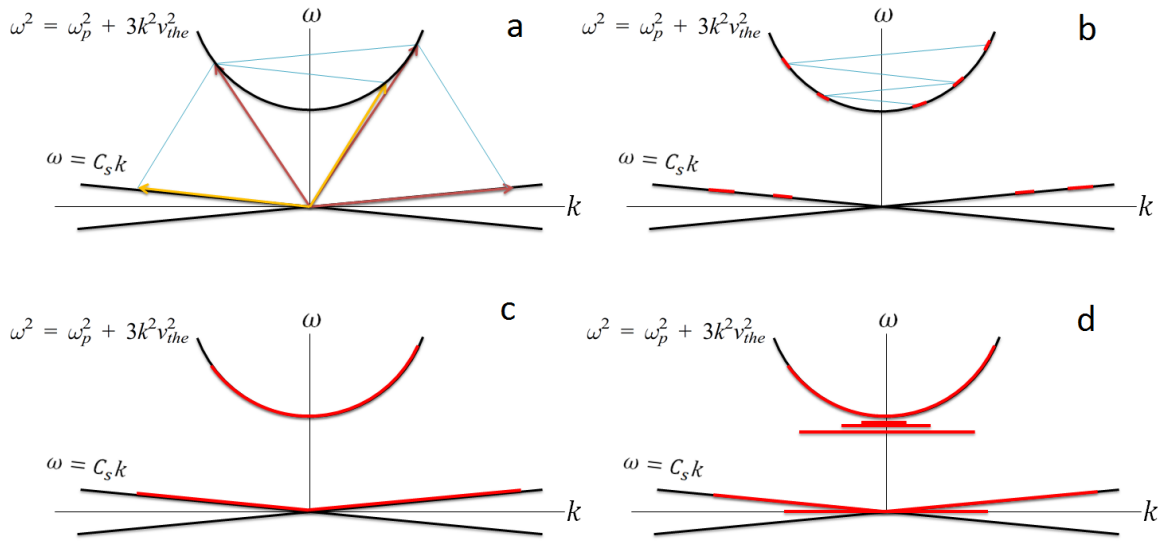


Figure 2.26. Panels a, b, and c show a cascade of parametric decays from the wave number at which the energy has been injected by the electron beam to smaller wave numbers. Panel d represents features that do not follow the linear dispersion relations for the ion acoustic and Langmuir waves. These are signatures of highly nonlinear features (cavitons) that can be produced during the turbulence.

Provided there is enough input energy a cascade of PDIs may occur, transferring energy to smaller wave number in each step (see Figure 2.21b). This cascade may continue until the last produced Langmuir wave reaches to sufficiently low wave numbers where the PDI can no longer satisfy the frequency and wave number matching conditions. In terms of the regions shown in Figure 2.25, the last produced Langmuir wave leaves the PDI region and enters the MI region. Note that the products of individual PDIs may broaden in frequency and ultimately cover a broad range of frequencies and wave numbers (Figure 2.21c).

Modulational Instabilities are four-wave processes by which two Langmuir quanta $L_1(\omega_1, k_1)$ produce a Langmuir quantum $L_2(\omega_1 + \Omega, k_1 + K)$ and a Langmuir quantum $L_3(\omega_1 - \Omega, k_1 - K)$ via exchange of an ion sound quantum $S(\Omega, \vec{K})$. According to the mathematical expression $\sin(k + K) + \sin(k - K) = 2 \sin(k) \sin(K)$ it can be shown that MIs lead to the modulation of an initially uniform Langmuir wave (with wave number k) and its break up into wave packets with a scale K^{-1} (see *Robinson* [1997] for more details). Depending on the regime of the instability, i.e. MI, subsonic MI, or supersonic MI, (1) the ion sound quantum can be an ion acoustic wave or an ion acoustic quasi mode that does not follow the linear dispersion relation and (2) K can be much larger or smaller than k (i.e. the Langmuir energy can transfer to higher or lower wave numbers). MIs are often discussed in the literature as one route to caviton formation and wave collapse. In this case, through highly nonlinear interactions, the peaks of the modulated Langmuir wave become narrower and more intense and the ion response appears as stationary density cavities at the locations of the peaks which narrow and deepen (i.e. *collapse* to smaller scales) due to the Ponderomotive force of the Langmuir field. Eventually localized density cavities with intense Langmuir energy trapped into them, i.e. cavitons, are formed. Signatures of cavitons are shown in Figure 2.26d. These will be discussed in details in Chapter 5.

One goal of this thesis is to investigate the 5 instability regimes summarized in Figure 2.25 as well as other relevant processes such as the wave collapse and revisit the topic of beam generated Langmuir turbulence for the ionospheric F region plasma.

2.6 Ionospheric Modification Experiments

Ionospheric modification experiments (also known as ionospheric heating experiments) refer to experiments in which a large number of antennas (a heater) are used to transmit megawatts of electromagnetic radiation with frequency below the peak plasma frequency of the ionosphere into the ionosphere. The transmitted electromagnetic wave interacts with the ionosphere near the reflection height, where its frequency matches the local frequency of the plasma, exciting a spectrum of plasma waves—most prominently, Langmuir waves which grow to very high intensities and lead to Langmuir turbulence. On long time scales after the heater is turned on, the pump wave modifies the bulk properties of the ionosphere, altering the local density and temperature and producing field-aligned irregularities. But on short time scales, after the heater is turned on and before the pump wave affects the background plasma greatly, ISR measurements from within the heated region can be used to study the induced Langmuir turbulence and nonlinear properties of the ionospheric plasma [*Carlson et al.*, 1972; *Fejer et al.*, 1991; *Cheung et al.*, 1992; *Isham et al.*, 1999].

Chapter 3

Naturally Enhanced Ion Acoustic Lines

Ever since the first observation by *Foster et al.* [1988], the appearance of strong non thermal echoes in incoherent scatter radar (ISR) data has been the subject of numerous theoretical and experimental studies. Different mechanisms have been proposed to explain NEIALs. These include (1) streaming instabilities due to relative drifts between thermal electrons and different species of ions [*Rietveld et al.*, 1991; *Collis et al.*, 1991; *Wahlund et al.*, 1992], (2) wave-wave interactions where a destabilized primary Langmuir wave gives rise to enhanced ion acoustic waves [*Forme* 1993, 1999; *Strømme et al.*, 2005], and (3) destabilization of ion acoustic waves by local acceleration of electrons by ion-cyclotron waves [*Bahcivan and Cosgrove*, 2008]. Regardless of the generation mechanism, the initial free energy is assumed to be provided by electron precipitation. Since auroral activity is a proxy for electron precipitation, some experimental works have been focused on correlating radar echoes with optical data and investigating the temporal and spatial relationship between NEIALs and different types of aurora [*Collis et al.*, 1991; *Sedgemore-Schulthess et al.*, 1999; *Grydeland et al.*, 2003, 2004; *Blixt et al.*, 2005; *Michell et al.*, 2008, 2009; *Michell and Samara*, 2010]. Other efforts have focused on the statistical occurrence of NEIALs as a function of altitude, season, and radar frequency [*Rietveld et al.*, 1991, 1996].

One aspect of NEIALs that has not been systematically investigated is their dependence on magnetic aspect angle. The degree to which the visibility of NEIALs changes with

magnetic aspect angle depends on the underlying generation mechanism. For instance, streaming instabilities produced by field-aligned particle fluxes are expected to destabilize ion acoustic waves in a highly field-aligned fashion, whereas ion acoustic wave enhancements generated by parametric decay of Langmuir waves should be observable over a wide range of angles to the magnetic field lines (as discussed further in Section 3). The aspect angle dependence of NEIALs therefore provides an additional constraint on possible generation mechanisms. The lack of experimental work on this matter is in part due to the ephemeral nature of the echoes coupled with limitations in beam steering speed associated with dish-based ISRs. However, the pulse-by-pulse steering capability of the new Advanced Modular Incoherent Scatter Radars (AMISRs) is well suited for such studies.

In the study presented in this chapter, the multi-beam capability of the 450 MHz Poker Flat Incoherent Scatter Radar (PFISR; 65.12N, 147.47W) is exploited to investigate the visibility and intensity of NEIALs as a function of magnetic aspect angle. NEIALs are known to be localized in space with small horizontal scales (about 100 meters) [*Cabrit et al.* 1996; *Grydeland et al.*, 2004]. Since different beam directions intersect different locations in space, it is possible to mistakenly interpret spatial variability in the NEIAL source as a magnetic aspect angle effect. To distinguish between these cases, we monitor auroral activity as a proxy for the spatial distribution of the underlying turbulence. The data presented in this chapter have been obtained during substorm expansion phase, wherein dynamic auroral forms moved rapidly through the set of radar beams and later

covered a large portion of the sky. Such large scale coverage has been used to put additional constraints on the conclusions that can be reached from the radar data.

3.1 Experimental Results

An experiment was conducted during a one-week period beginning 1 March 2011 with the specific aim of investigating the aspect angle dependence of NEIALs. PFISR was configured to sample five beam positions, one pointed to the magnetic zenith and four adjacent beams separated by only one degree. Figure 3.1 shows the position and angular extent (half-power contour ~ 1.1 degrees) of the beams in one frame extracted from the narrow-field CMOS camera measurements used in the study by *Dahlgren et al* [2013], with geodetic azimuth and elevation contours shown. The narrow-field camera was collocated with PFISR, thus the beam patterns in Figure 3.1 are independent of the altitude.

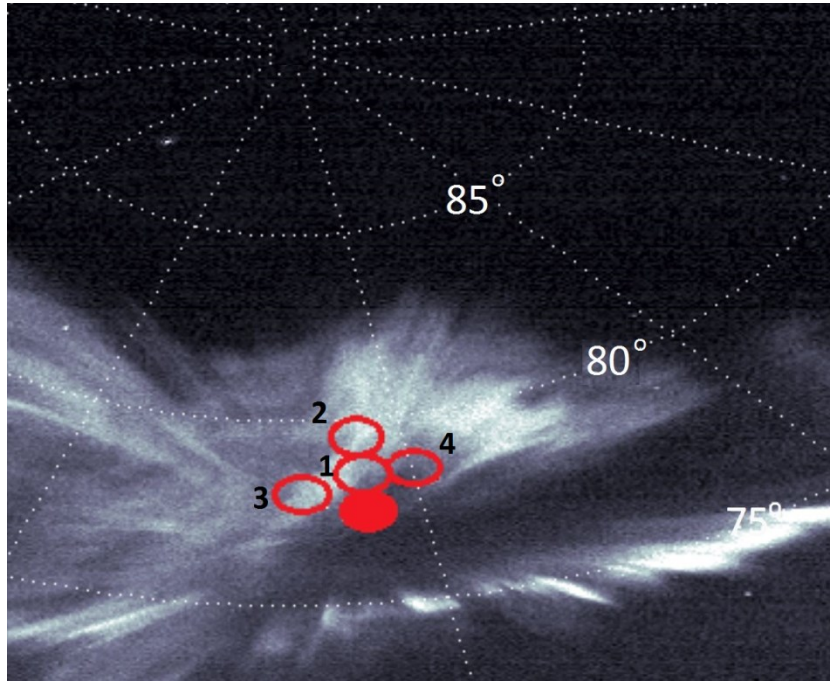


Figure 3.1. PFISR beam positions overlain on one frame recorded by a narrow-field camera on 01 March 2011. The magnetic zenith beam is filled in, the separation between beams is one degree (after *Dahlgren et al.* [2013]).

The magnetic zenith beam, indicated in solid red, is defined as the radar beam parallel to the magnetic field line at the ground, as determined using the International Geomagnetic Reference Field (IGRF) model [*International Association of Geomagnetism and Aeronomy, Working Group V-MOD*, 2010]. Due to curvature of the field lines, this beam is not exactly parallel to the field lines at higher altitudes. However, it remains the closest beam to parallel. At altitudes where the NEIALs are observed the magnetic zenith beam has an angle of about 0.2 degrees with the magnetic field lines.

A substorm onset occurred in the southeast of the PFISR facility at ~10:00 UT on 1 March 2011, with the poleward expansion of the aurora reaching the PFISR zenith at ~10:05:30 UT. Figure 3.2 shows snapshots at 557.7-nm wavelength recorded by the Poker Flat all sky camera as the aurora expanded through the PFISR beam cluster (indicated in red). The oxygen 557.7-nm emission in the aurora occurs at altitudes between 120 and 180 km. It is a proxy for electron precipitation over a broad range of energies, and is therefore expected to appear on flux tubes that are magnetically conjugate to NEIALs.

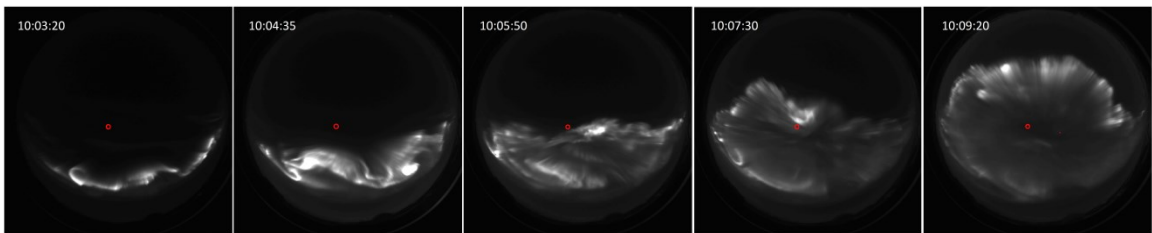


Figure 3.2. Sequential all sky camera samples showing auroral activity associated with a substorm poleward expansion on 01 March 2011. The nominal position of the PFISR beam cluster (Figure 3.1) is indicated in red.

Figure 3.3 shows received PFISR power in the ion line channel during this period. For the sake of simplifying the aspect angle comparison, radar data in only three beams are shown, corresponding to the beams labeled MZ, 1, and 2 in Figure 3.1. The streaks with power >10-dB are all NEIALs. Significant variations in the echo power are observed from beam to beam. The echoes at higher altitudes (> 250 km) in the zenith beam are less pronounced at one degree offset and almost completely disappear at two degree

offset. The angular dependence is less significant for the lower altitude echoes (< 250 km). This is readily seen in Figure 3.4, which shows line plots of the occurrence rate of NEIALs for all five beams during a 90-second period starting at 10:05:20 UT. The occurrence rate at any altitude is calculated by counting the transmitted radar pulses from Figure 3.3 for which the scattered power from the same altitude is at least a factor of 10 higher than thermal level. The values are then normalized with total number of transmitted radar pulses during this 90-s interval.

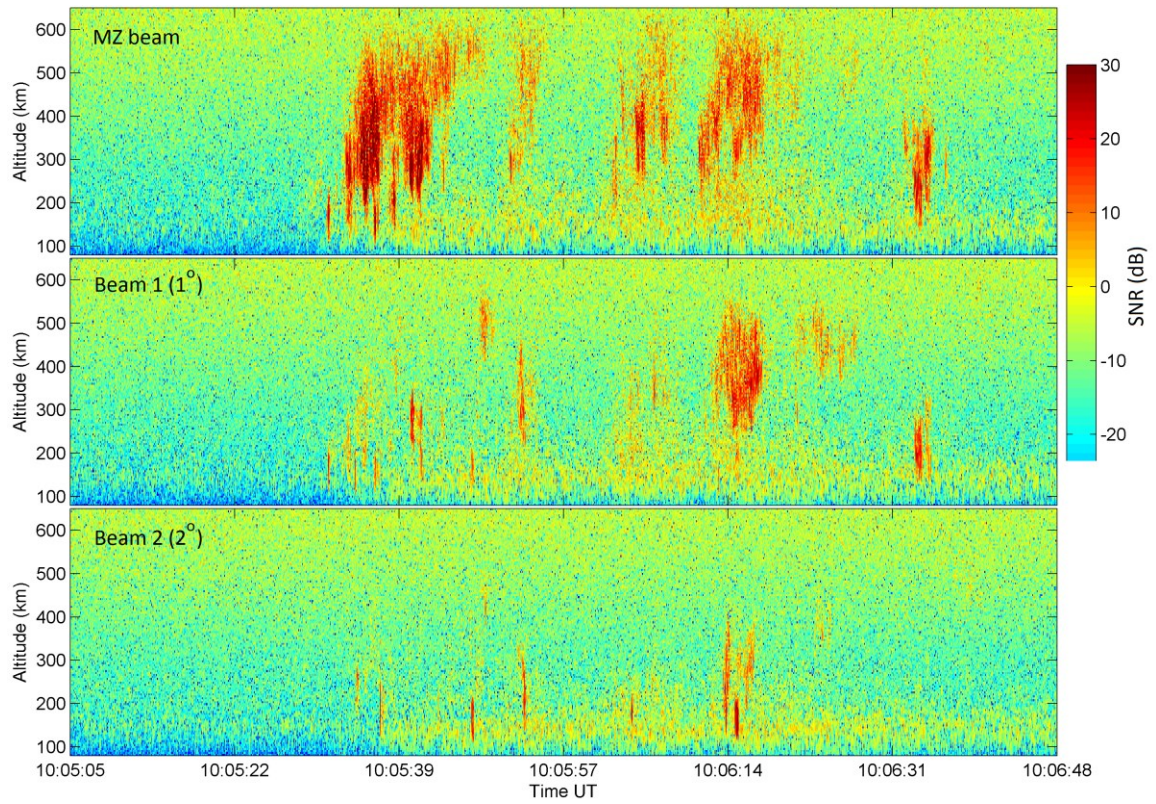


Figure 3.3. Range-time plot of received power in the ion line channel for three of the radar beams (see Figure 3.1) during a period when the substorm expansion crossed through the PFISR beams. Mentioned in parenthesis are angles with respect to the magnetic zenith beam.

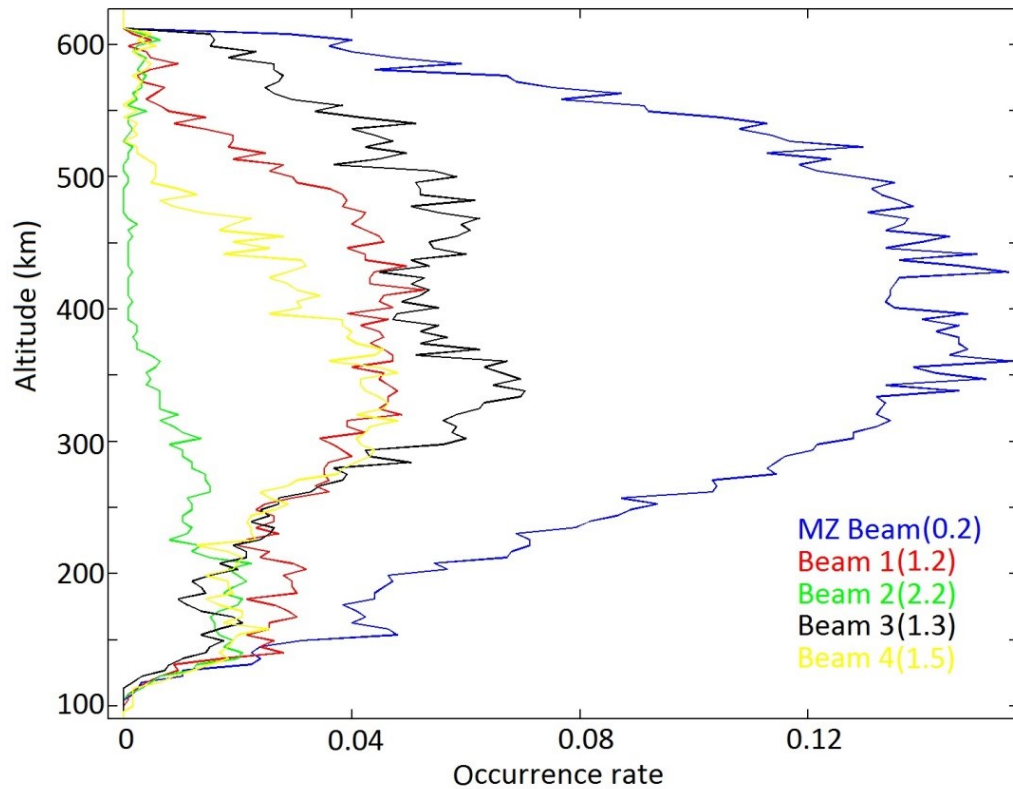


Figure 3.4. Line plots of relative occurrence of NEIALs during a 90-second period starting at 10:05:20 UT for all beams of the 01 March 2011 experiment. Mentioned in parenthesis are angles with respect to magnetic field line at 500 km.

An overview movie showing the full all sky camera image sequence used to create Figure 3.2 and the corresponding PFISR backscattered power measurements, embodying the interval of Figure 3.3, has been included as auxiliary material in the corresponding published journal paper [Akbari and Semeter; 2014]. The movie better illustrates the space-time relationship between poleward expanding auroral forms and the occurrence of NEIALs within the PFISR beam cluster.

Figure 3.5 shows 5-s samples of the zenith ion line power as a function of frequency and altitude. Each image has been individually normalized in order to highlight morphological variations. Panel a corresponds to pre-event conditions and represents thermal ISR scatter. Panel b corresponds to the poleward edge of the substorm expansion, showing enhancements in both ion line shoulders with some evidence for a zero Doppler central peak. Presence of a zero Doppler central peak in ion line spectra has been explained in terms of the cavitating Langmuir turbulence [Guio and Forme, 2006; Akbari et al., 2012; Isham et al., 2012]. Panels c and d show the evolution toward higher altitude echoes, with preferential enhancement of the downshifted shoulder. The Panel d shoulders exhibit a negative bulk Doppler shift, corresponding to upward ion velocities of ~ 800 m/s at 500 km altitude.

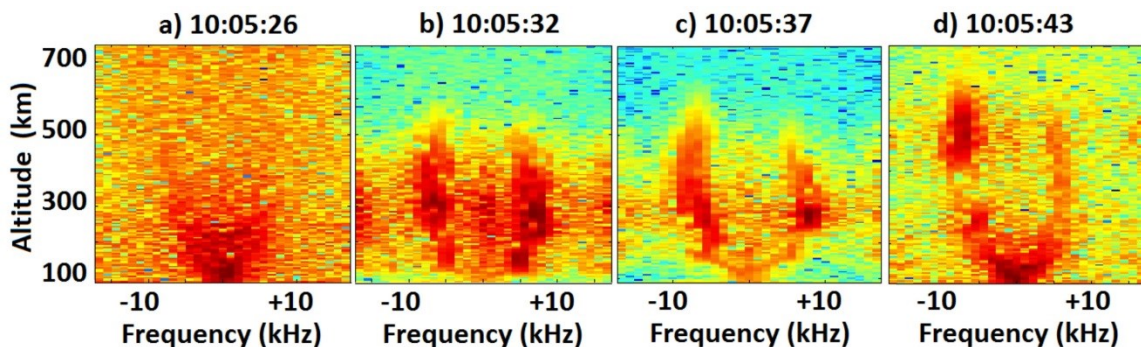


Figure 3.5. Samples of normalized PFISR power spectra corresponding to Figure 3.3, computed using only 5-second integration and 71 radar pulses. Panel a shows the pre-event thermal backscatter. The remaining panels exhibit various types of enhancements in the ion acoustic lines. The time stamps correspond to the start time of the integration.

Although the standard ISR analysis used to derive plasma parameters is not applicable for the coherent echoes, the frequency offset of the ion acoustic shoulders can be used to determine the wave phase velocity and, therefore, the plasma temperatures. Following the procedure presented by *Forme* and *Fontaine* [1999], for the echoes below 200 km the location of the shoulders at ± 6 kHz and ion composition of mixture of NO^+ and O_2^+ and the further assumption that the ion temperature maintains its typical value of ~ 1100 (K) just before the occurrence of the turbulence [*Forme* and *Fontaine*, 1999] gives the estimation of $T_e \approx 5000$ (K). For the echoes above 200 km, the shoulder offset is 9 kHz. Assuming O^+ is the dominant ion with temperature of ~ 2000 (K) we again calculate $T_e \approx 5000$ (K).

In an attempt to further explore magnetic aspect angle dependence, we studied results obtained from another multi beam PFISR experiment conducted on March 23, 2007. In this experiment PFISR was configured to sample a 3×3 array of beam positions, plus an additional beam trained in the magnetic zenith. Similar to Figure 3.1, Figure 3.6 shows the position of the radar beams on a sample auroral image, with the magnetic zenith beam marked, and other beams numbered 1-9. At $\sim 11:20:10$ UT strong echoes were observed in seven beams.

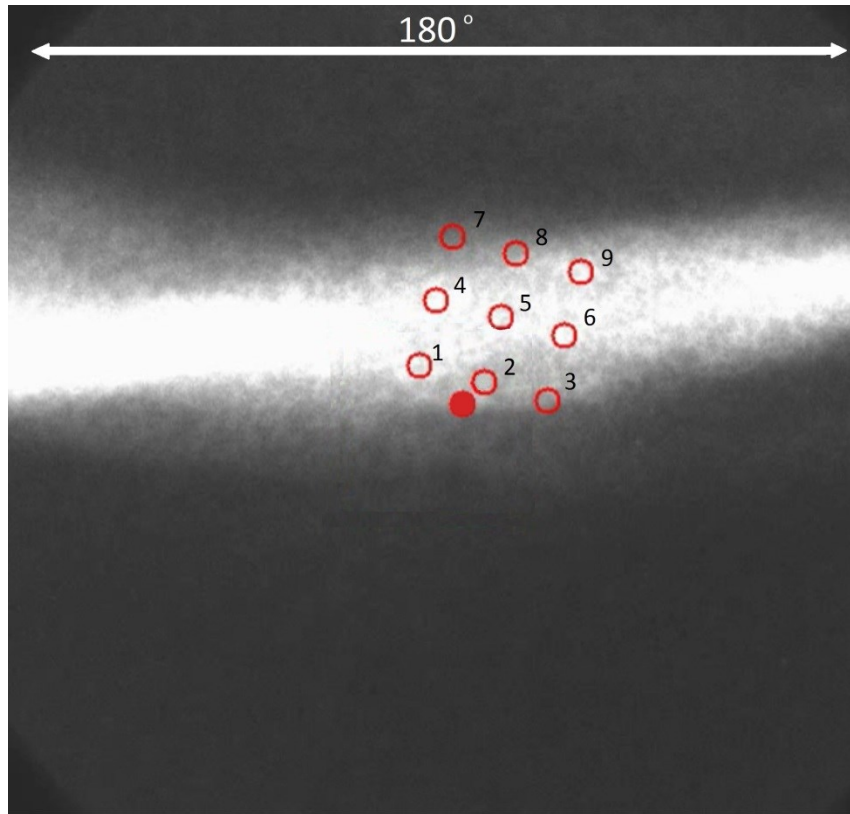


Figure 3.6. Radar beams configuration on top of one frame of an all sky camera (March 23, 2007 experiment). The magnetic zenith beam is filled-in.

Figure 3.7 shows the total received ion line power as a function of altitude and time in the five radar beams (beams MZ, 2, 3, 5, and 8) where the coherent echoes are strongest. In the magnetic zenith beam three bursts of echoes are identified and numbered. These echoes have been identified as signatures of Langmuir turbulence [Akbari *et al.*, 2012] and are subject of extensive discussions in the next chapter. Ion line spectra associated with echo 1 and echo 3 in Figure 3.7 are shown in Figure 3.8. As will be discussed in the next chapter, the filled-in ion line spectrum characteristic of echo 1 (hereafter called type 1) and the simultaneous observation of a double-peaked plasma line spectrum led to the

conclusion that this echo was produced by strong Langmuir turbulence [Akbari *et al.*, 2012]. The characteristics of echo 3 (hereafter called type 2), however, were similar to characteristics of the echoes in Figure 3.3 and 3.5. The high altitude portion of this spectrum can be seen to be Doppler shifted by about 2 kHz towards negative frequencies, indicating upward motion of plasma with velocity of ~ 660 m/s.

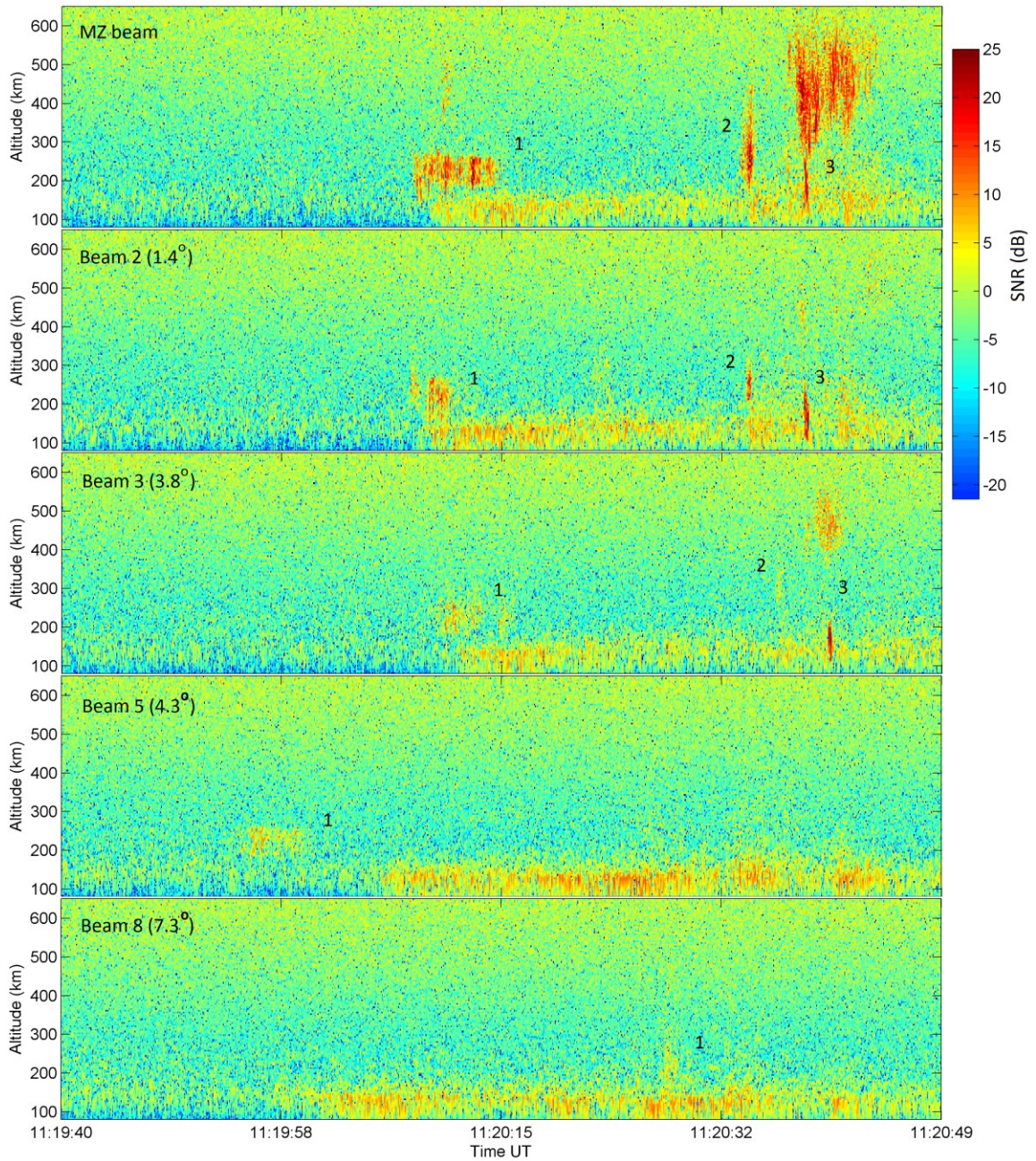


Figure 3.7. Similar to Figure 3.3, range-time plot of received power in ion line channel for five of the radar beams in Figure 3.6. Mentioned in parenthesis are angles with respect to the magnetic zenith beam. In the top panel, three bursts of coherent echoes are labeled (echo 3 refers to the whole enhanced received power extended from 100 to 600

km), which are tracked in subsequent panels. Echoes similar to echo 1 appear in all panels while echoes similar to echo 3 only appear in the top three panels.

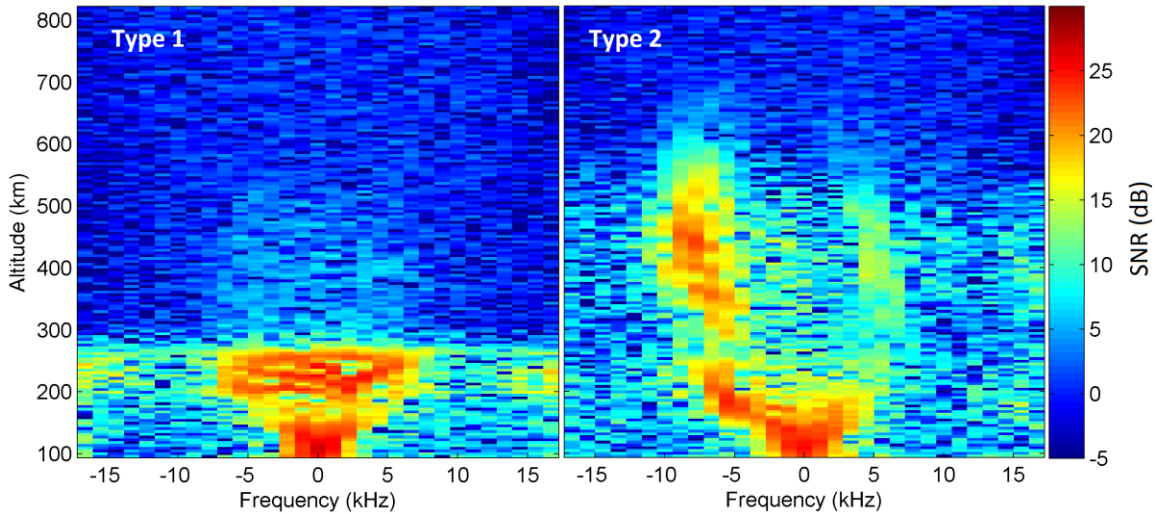


Figure 3.8. Ion line spectra computed from measurements within the first and third echoes in the top panel of Figure 3.7. In the right panel, the apparent shift of the spectrum toward negative frequencies corresponds to upward plasma velocity of ~ 660 m/s.

Comparing Figure 3.7 to Figure 3.3, we find similar aspect angle dependence: (1) there is a decrease in NEIAL visibility with increased aspect angle, and (2) the higher altitude type 2 echoes show stronger aspect angle sensitivity than the lower altitude type 2 and type 1 echoes.

3.2 Discussions

Using the EISCAT UHF radar *Rietveld et al.* [1991] reported NEIALs at angles 0, 12.5, and 14.6 degrees with respect to magnetic field lines and found the main difference to be a smaller range extent of NEIALs at larger angles. The results were explained in terms of the horizontally localized nature of NEIALs. Our results, obtained using pulse-by-pulse sampling with the electronically steerable PFISR, show a significant difference in NEIAL power for beams that are separated by only one degree.

The claim rests on the combined consideration of radar and all sky camera observations. In carefully examining Figure 3.3, for instance, one does not find one-to-one correlation between features observed at different aspect angles. This is not surprising, since the horizontal extent of individual NEIAL scattering regions is small (~100 m) compared to the beam separation (~5 km at 300 km range). However, a clear trend can be seen in the observability of NEIALs as the radar beam moves away from parallel to the magnetic field lines; that is, the NEIALs at higher altitudes quickly disappear as the angle increases.

There are two possible explanations for this trend. One is that the source of the NEIALs was non-uniformly distributed within the spatial region covered by the different beams. But this is not supported by the optical measurements. Figure 3.2 showed representative auroral activity recorded before, during, and after the interval shown in Figure 3.3. In the left panel, at 10:03:20 UT, electron precipitation, manifested by auroral brightness, was present in the south and spread toward the north. At time 10:05:50 UT, corresponding to

the middle panel in Figure 3.2, the poleward edge of the brightness reached the region intersected by the PFISR beams, and the NEIAL echoes appeared in radar data. As the leading edge of the substorm expansion continued poleward, past the PFISR beams, the coherent echoes disappeared. There is no reason to believe that the characteristics of the NEIAL source changed as the source traversed the PFISR beam pattern. This conclusion is further supported by the movie included as auxiliary material in the published journal paper corresponding to these results ([*Akbari and Semeter, 2014*]), which shows a longer interval of PFISR backscattered power measurements in the magnetic zenith and the corresponding full all sky image sequence (20-s samples). We therefore conclude that the second explanation is more plausible—namely, the observed trend reveals variations in the observability of NEIALs with magnetic aspect angle.

The aspect angle dependence of NEIALs is determined by their generation mechanism. Strong dependence is not expected for NEIALs produced by the parametric decay of Langmuir waves. In both weak and strong Langmuir turbulence regimes, even if the initial Langmuir wave produced by an electron beams is strictly field aligned, the interaction of the Langmuir waves and ion density perturbations spreads the energy to larger angles and, as a result, incoherent scatter radars would be expected to observe the turbulence at angles as high as 20 and 40 degrees for the weak and strong regimes of turbulence, respectively [*DuBois et al., 1993*]. Note that the angular spread of turbulence also depends strongly on the source intensity, and for very small source energies the angular spread might not be as high as the angles mentioned above. Therefore the aspect angle dependence seen in Figure 3.3 strongly suggests that these echoes are not produced

by parametric decay of Langmuir waves but, rather, are produced by a plasma streaming instability.

In previous observational studies, the simultaneous enhancement of both ion acoustic shoulders, the rapid successive appearance of up- and down-shifted shoulder at similar altitudes, and the asymmetry sometimes found in altitude profiles of NEIALs [Forme *et al.*, 2000] have been used to argue in favor of the parametric decay mechanism. In our observations, however, the same arguments fail to explain the dominance of the enhanced down-shifted shoulder (corresponding to upward wave propagation) at the highest altitudes (> 550 km). Moreover, coherent echoes produced by the Langmuir decay mechanism are most expected in a narrow layer around the F region peak, where the effect of the density gradient in saturating the wave amplitude is minimum [Akbari *et al.*, 2013]. Finally, noting the fact that type-2 NEIALs occur over large altitude extents, one would expect to detect concurrent plasma line enhancements if the NEIALs were indeed produced by parametric decay. Although the ion acoustic wave and the Langmuir waves involved in a parametric decay have different wave numbers, and ISRs only observe wave activity in a single wave number, the presence of the echoes from 600 km all the way down to 150 km (i.e. more than a factor of four range in plasma density) implies that the Langmuir waves are subject to instability over a wide range of wave numbers. This wide range of plasma densities should guarantee the simultaneous observation of NEIALs at higher altitudes and Langmuir waves near the F region peak.

On the other hand, the simultaneous enhancement of both ion acoustic shoulders along with the observed upward plasma motion of ~ 660 m/s (right panel of Figure 3.8) argues in favor of the ion-ion streaming instability mechanism [*Wahlund et al.*, 1992] for the type-2 echoes above 200 km (note that, unless subjected to temporal/spatial averaging, electron-ion streaming instability cannot give rise to simultaneous enhancement of both ion-acoustic shoulders). The observed upward plasma motion is also consistent with the high ion temperatures derived for lower altitudes. Ion temperature enhancements can be produced by strong horizontal electric fields that are often observed on the edge of auroral arcs, and subsequent ion-neutral frictional heating due to $E \times B$ drift [*Lynch et al.*, 2007; *Zettergren et al.*, 2008]. Alternatively, the ion heating and the upward motion can be produced by the electrostatic ion-cyclotron instability on the boundary of auroral precipitations [*Ungstrup et al.*, 1979; *Bering*, 1984; *Lysak et al.*, 1980; *Palmedesso et al.*, 1974].

Although plausible for higher-altitude (> 200 km) type-2 NEIALs, the ion-ion streaming instability mechanism does not suit the lower altitude (< 200 km) type-2 NEIALs (shown in Figure 3.3). Firstly, no sign of vertical plasma motion exists; secondly, ion acoustic shoulders are not enhanced simultaneously; and thirdly, at these altitudes ion dynamics are dominated by ion-neutral collision that prevents any mechanism from producing relative drift between different ion species. Observations of NEIALs at such low altitudes are rare. In fact we are only aware of those reported by *Rietveld et al.* [1991]. In their observations, given the fact that only the up-shifted shoulder was enhanced at lower altitudes, they argued that the echoes were produced by thermal electrons streaming from

the F region toward the E region. According to this theory, soft electron precipitation is collisionally stopped at F region heights where cross field mobility is poor. Accumulation of electrons results in a field-aligned electric field which, in turn, repels thermal electrons upward and downward from the stopping height. This mechanism may be applicable to the *Rietveld et al.* observations, but cannot explain the low altitude down-shifted shoulder enhancements observed in our data. The ion cyclotron mechanism proposed by *Bahcivan* and *Cosgrove* [2008] or upward streaming thermal electrons originating from even lower altitudes might be candidate mechanisms.

The weaker aspect angle dependence of type-2 echoes at lower altitudes versus at higher altitudes should be further studied. Whether this is due to a different generation mechanism or due to parameters of the ambient plasma is yet to be determined. However, we would like to mention the possibility that this behavior might be simply due to different plasma parameters at lower and higher altitudes rather than the source of instabilities. At lower altitudes, the ions become increasingly demagnetized and their motions are not as tightly constrained by the magnetic field compared with higher altitudes. As a result ion acoustic turbulence might be less sensitive to magnetic aspect angle at lower altitudes.

3.3 Summary and Conclusions

Experimental data presented in this chapter reveals that the visibility of substorm-related NEIALs by incoherent scatter radars is highly sensitive to magnetic aspect angle. The

aspect angle sensitivity was found to depend on both altitude and spectral morphology, providing a means of classifying the results according to allowable generation mechanisms: type-1 NEIALs (flat ion line spectrum) are consistent with the parametric decay of Langmuir waves into ion acoustic waves; these echoes show weak aspect angle dependence. The higher-altitude (> 200 km) type-2 NEIALs (one or both ion acoustic shoulders enhanced) are consistent with the ion-ion streaming instability, and are extremely sensitive to the aspect angle. These echoes almost completely disappear when the aspect angle is increased to only two degrees. And finally, the lower altitude (< 200 km) type-2 NEIALs show less aspect angle sensitivity when compared to the higher altitude type-2 NEIALs; these echoes are not consistent with the ion-ion streaming instability. We also conclude that during dynamic geophysical conditions, such as the substorm intervals studied in this report, more than one of the generation mechanisms proposed to explain NEIALs may be simultaneously at work.

Chapter 4

Langmuir Turbulence: Experimental Results

Chapter 4 presents results from a few experiments conducted by the Poker Flat incoherent scatter radar. In Section 4.1 results from an experiment conducted on 23 March 2007 that led to discovery of a new type of coherent echo in ISR data are presented. This section is followed by discussions in Section 4.2 that clarifies the observed features and explains the radar echoes in terms of signatures of electron beam-generated Langmuir turbulence. Section 4.3 presents results of an extensive search through the PFISR database that was done with the goal of identifying more examples of the newly discovered echoes. As a result of this search many examples of the coherent echoes were detected, many of which were accompanied by unexpected features. Discussions on the observed features are the subject of Section 4.4.

4.1 March 23, 2007 Experiment: Cavitating Langmuir Turbulence in the Auroral Ionosphere

The observations reported in this section were recorded during the expansion phase of a substorm with onset at 11:10 UT on 23 March 2007. This was the first substorm studied using the coordinated ground-based and space-based diagnostics of the THEMIS mission and, as such, the event has received considerable attention [*Angelopoulos et al.*, 2008]. Auroral activity for this event reached the zenith of PFISR (147.48°W, 65.13°N) at 11:20

UT, where it was observed simultaneously by the radar and a collocated narrow-field video system. The dynamic auroral morphologies observed at this time have been studied by *Semeter et al.* [2008] in the context of dispersive Alfvén waves (video data is linked as dynamic content in the paper by *Semeter et al.* [2008]). The focus of this section is on non-thermal ISR echoes observed by PFISR during the same period.

For this experiment PFISR was configured to sample a 3×3 grid of beam positions, plus an additional beam trained in the magnetic zenith. The transmit waveform was a 480- μ s uncoded pulse, from which ion line spectra and up- and down-shifted plasma line spectra were computed for each of the 10 beams. Here, we focus on observations in the magnetic zenith beam only (-154.3° azimuth, 77.5° elevation), where the largest coherent echoes were observed.

Figure 4.1a shows the total received ion line power as a function of altitude and time in the magnetic zenith beam during a 50-second period beginning at 11:20 UT. The enhanced scatter below 150 km beginning at 10 s is due to ionization of the E region by precipitating electrons. Above this altitude, three intervals of coherent scatter can be observed, identified as 1, 2, and 3 in the figure. These events were correlated with dynamic auroral activity within the beam. Figure 4.2 shows representative images associated with each scattering event, along with the position of the radar beam. Scattering event 1 occurred near the edge of the intensifying discrete auroral arc. Event 2 occurred just after breakup as a dispersive packet of elemental arcs (100-m width) transited rapidly through the beam. Event 3 occurred as the auroral breakup filled the

field of view.

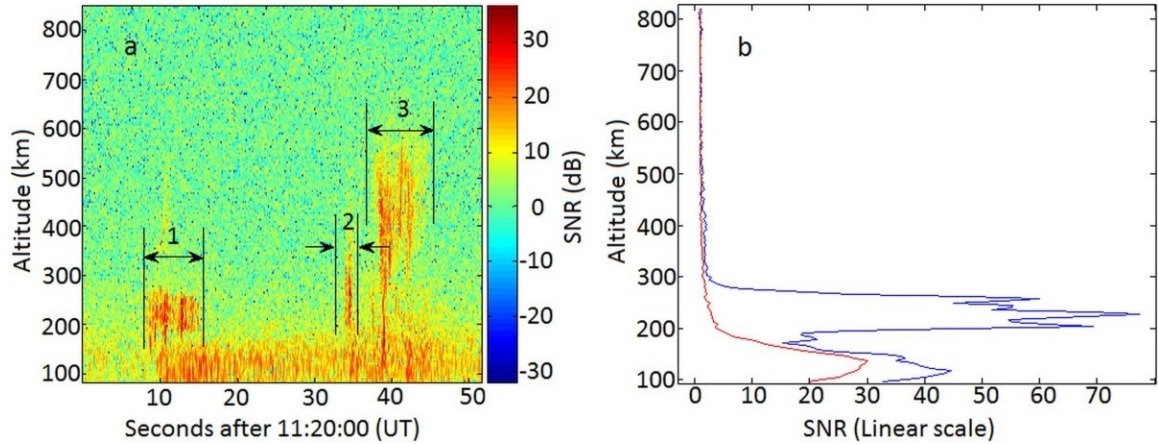


Figure 4.1. (a) Received radar power, in the ion line channel, for the magnetic zenith beam. Three intervals of coherent scatter are identified and numbered. (b) Vertical cuts from the power plot in Figure 4.1a. Blue: At a time during the scattering event 1. Red: During the thermal scattering interval between the event 1 and 2. (SNR values are not range corrected)

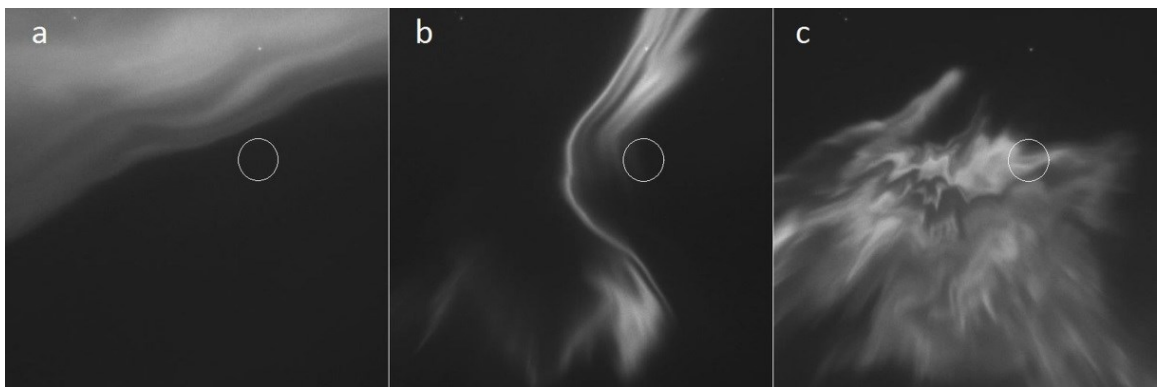


Figure 4.2. Representative narrow-field (11 degree diagonal field of view) images of dynamic auroral forms associated with (a) event 1, (b) event 2, and (c) event 3 in Figure

4.1a. White circles represent the location and approximated 3 dB beamwidth of the radar beam. Exact 3 dB beamwidth is not a circle. (Images taken from *Semeter et al.* [2008])

Figure 4.3 shows height-resolved ion line spectra computed from measurements for these three scattering events. Event 1 shows unusual characteristics. First, the apparent altitude extent of the scattering region is 72 km, exhibiting a sharp cutoff at 270 km altitude (see Figure 4.1b). This suggests that the scattering may be localized in altitude near 230 km but, due to the poor altitude resolution of the measurements, appears to arise from a layer with extent similar in width to the range ambiguity function, 72 km here (i.e., although the received signal is sampled at 30 μ s, corresponding to a range resolution of 4.5 km, the true resolution is limited by the length of the transmitted pulse). The second unusual feature is the flat ion line spectrum. This is shown most clearly by blue line plot in Figure 4.4, which was produced by averaging the spectrum in Figure 4.3a over the scattering layer. Typical ion acoustic spectra have a double humped shape associated with the Landau damped ion acoustic mode matching the radar wave number (see red line plot in Figure 4.4).

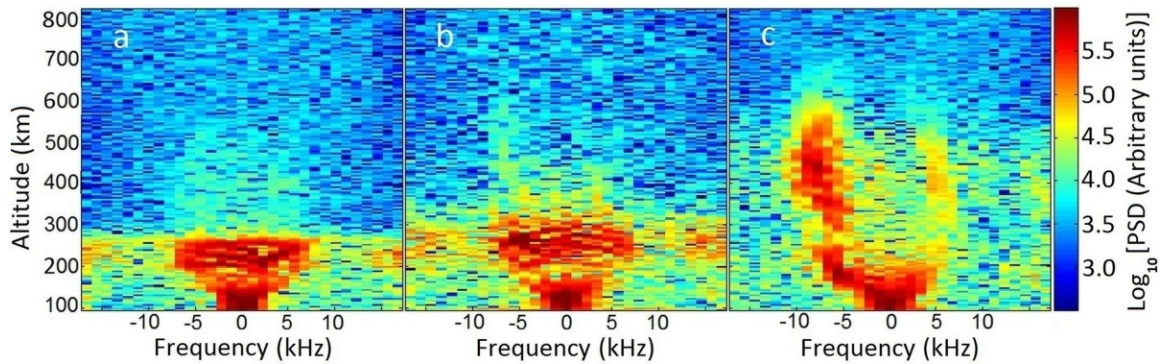


Figure 4.3. Ion line spectra computed from measurements within the (a) first, (b) second, and (c) third scattering events of Figure 4.1a. (SNR values are not range corrected)

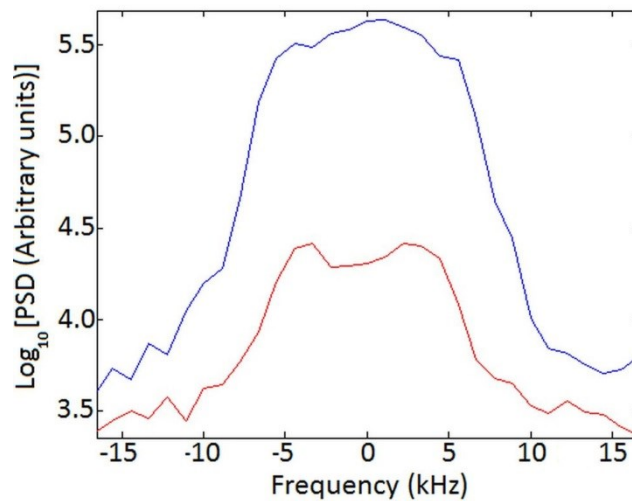


Figure 4.4. Blue: Ion acoustic spectrum for scattering event 1 (averaged over the scattering layer). Red: Ion acoustic spectrum for the thermal scattering interval between event 1 and 2 (averaged between 200 km and 270 km).

Figures 4.5a and 4.5b show down- and up-shifted plasma line spectra, respectively, for scattering event 1. The critical feature is the presence of two peaks separated by 120 kHz.

This is seen more clearly in Figure 4.5c, which plots the plasma line power spectra through the features in Figures 4.5a and 4.5b.

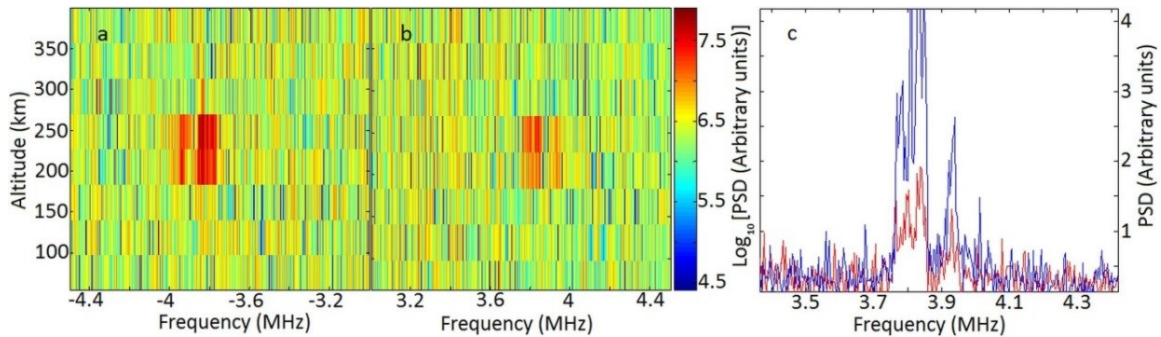


Figure 4.5. (a and b) Down- and up-shifted plasma line measurements, respectively, from scatter events 1. (c) Blue and red: horizontal cuts from Figures 4.5a and 4.5b, respectively, averaged over 200-km and 250-km altitude; showing the presence of two peaks in the plasma line spectra. (Negative frequencies are folded on top of the positive frequencies.)

Scattering event 2 presents similar characteristics to those of event 1, albeit with poorer statistics since the time interval used to compute the spectra is shorter. The ion acoustic spectrum, shown in Figure 4.3b, also shows enhancements at zero frequency. The plasma lines were also enhanced at this time, but their morphologies were not sufficiently resolved with the limited integration period.

For event 4 (Figure 4.3c), the ion acoustic spectrum shows features consistent with the classic Naturally Enhanced Ion Acoustic Line (NEIAL) [*Sedgemore-Schulthess and St. Maurice, 2001; Mitchell and Samara, 2010*], where one or both shoulders of the power

spectrum is enhanced well above the thermal level. There was no plasma line enhancement observed for event 3.

4.2 March 23, 2007 Experiment: Discussions

Simultaneous enhancements of ion acoustic waves and Langmuir waves in both up- and down-shifted channels of an ISR, can only be explained in terms of Langmuir turbulence. In the case of the observations presented in Section 4.1, further confirmation for presence of Langmuir turbulence arises from the observed double-peaked plasma line spectra in Figure 4.5c. Such plasma line spectra have been measured during ionospheric modification experiments where cavitating Langmuir turbulence is artificially generated in the ionosphere. Such spectra consist of a peak at the Langmuir wave frequency, due to scattering off Langmuir waves that follow the linear dispersion relation, and an additional peak at the plasma frequency, that is produced by scattering off cavitons.

This interpretation of Figure 4.5 is supported by our calculations of plasma frequency and Langmuir frequency. By performing the standard ISR fitting procedure for the time of thermal scattering 30 seconds before Event 1, we derived the background electron density of about $n_0 = 1.82 \times 10^{11} \text{ (m}^{-3}\text{)}$ at 230 km. Using the relation $f_p \approx 8.98 \sqrt{n_0}$, this fixes the plasma frequency at $f_p = 3.83 \text{ MHz}$, which agrees with the position of the first peak in our plasma line measurement. The background electron temperature is calculated to be about 1925 °K, and the angle between the radar beam and the magnetic field lines at 230

km is about $\alpha = 1.148^\circ$. Substituting these into the linear Langmuir dispersion relation, $\omega^2 = \omega_p^2 + 3k^2 V_{the}^2 + \Omega_e^2 \sin^2 \alpha$, gives the Langmuir frequency of 3.93 MHz which is close to the position of the second peak in our experiment (3.939 MHz). In the above equation Ω is electron gyro frequency (9.6 megarad/s, computed using the IGRF model), V_{the} is mean thermal velocity of electrons, and k is the radar wave number.

Cavitating Langmuir turbulence is expected to produce enhanced features in the ion line channel as well. The ion line spectrum in this case should include enhanced ion acoustic shoulders, corresponding to scattering off amplified ion acoustic waves, and an additional peak at zero Doppler, corresponding to scattering of stationary density cavities associated with Langmuir wave collapse and caviton formation [DuBois et al., 1991].

Figure 4.6 compares representative ion line power spectra associated with natural turbulence (Figure 4.6a) and heater-induced turbulence (Figure 4.6b), both observed with the PFISR. The heater-induced turbulence was generated by the High Power Auroral Stimulation heater, which was located ~ 35 km from PFISR [Kosch et al., 2009]. In each case, the spectra were calculated using a 72 km long pulse. Thus, even though the turbulence is confined to thin layers, the backscattered power is seen over an extended altitude range. The two panels are different in that in the heater-produced turbulence, unlike the naturally produced case, the central peak is distinguishable from the ion acoustic peaks. The origin of the difference is not clear at this point but it might be due to the different nature of the source in the two cases. Another difference is the stronger

incoherent scattering from the E region (100–150 km) in the case of the natural turbulence due to density enhancement produced by electron precipitation.

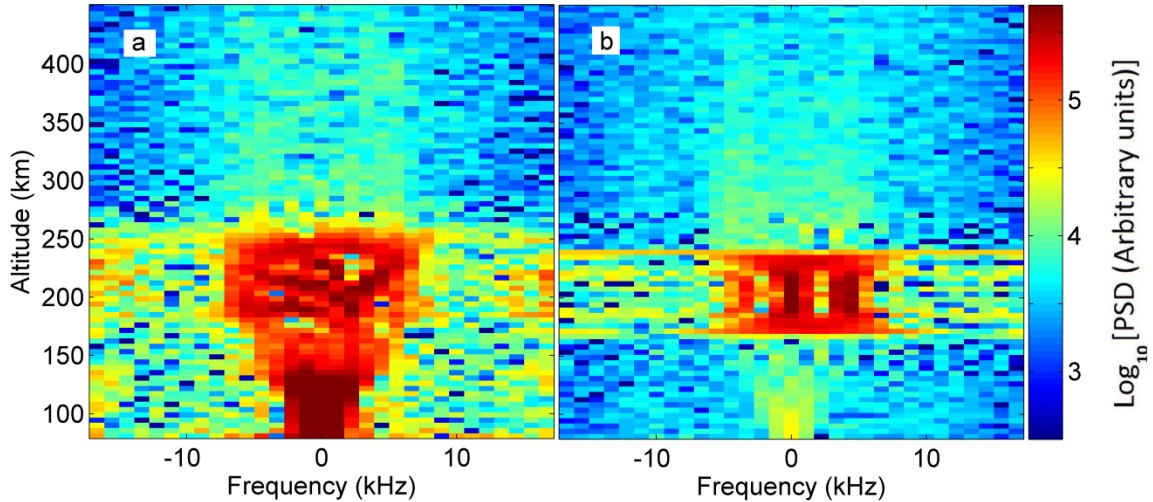


Figure 4.6. PFISR observations of anomalous ion line spectra from (a) naturally and (b) heater wave produced Langmuir turbulence. Figure 4.6a corresponds to the data shown in Figure 4.3a. Figure 4.6b was recorded during an active ionospheric modification experiment using the High Power Auroral Stimulation facility on 17 March 2007.

Based on the simultaneous enhancements of ion acoustic and Langmuir waves and the observation of the double-peaked plasma line it is concluded that naturally occurring cavitating Langmuir turbulence is a plausible interpretation of the presented data (i.e. echo 1 in Figure 4.1a). However, questions remain regarding 1) the source of free energy underlying the turbulence, 2) the limited altitude extend of echo 1, and 3) discrepancies that exist between the ion line spectra produced in the natural and heater-induced Langmuir turbulence (i.e. Figure 4.6). These will be addressed in the next sections.

4.3 Further Experimental Results on ISR echoes

In an attempt to identify more echoes similar to echo 1 in Figure 4.1a, a substantial amount of experimental data obtained by the PFISR were analyzed. The data often included ion and plasma line measurements from a 480 μs long pulse, and ion line measurements from a 16 baud Alternating Codes (AC). Alternating codes [Lehtinen, 1986] are sets of phase-coded pulses that permit spectral measurements with high range resolution at the expense of lower SNR and therefore are crucial in investigating the limited altitude extent of echoes produced by Langmuir turbulence. Different radar beam patterns were used in various experiments, however, here the focus is only on observations from the magnetic zenith beam (-154.3° azimuth, 77.5° elevation), where the largest coherent echoes were observed.

The search through the PFISR database resulted in identifying 35 instances of coherent scatter exhibiting flat ion line spectra similar to Figure 4.3a. The observed echoes were accompanied by interesting characteristics that are summarized below.

1. Echoes on the Edge of the E region Ionization Enhancements

The enhanced scatters usually occurred just before the E region ionization maximized due to energetic (keV) electron precipitation. Figure 4.7 shows two example range-time-intensity plots illustrating the temporal relationship between enhanced ion line power (echoes above 200 km) and E region ionization associated with the visible aurora (echoes below 150 km). Correlating the radar data in Figure 4.7 with optical data of

auroral activity confirms that the sudden drops in the E region signal strength correspond to sudden drops in intensity of aurora luminosity within the radar beam field of view. This does not necessarily imply that the electron precipitation has stopped in this period; however, this suggests a change in the energy of the precipitating electrons. The lack of correlation between the echoes and E region ionization enhancements together with occurrence of the radar echoes on the edge of the aurora suggest soft electron precipitations as the source of the echoes. This is consistent with the fact that the vicinity of an auroral arc is an ideal place for such electrons [Mishin and Banaszkiwicz, 1998; Arnoldy *et al.*, 1999]. The duration of the enhanced scatter is typically only a few seconds in the radar frame of reference. One fortuitous event, highlighted below, endured in the radar beam for over five minutes.

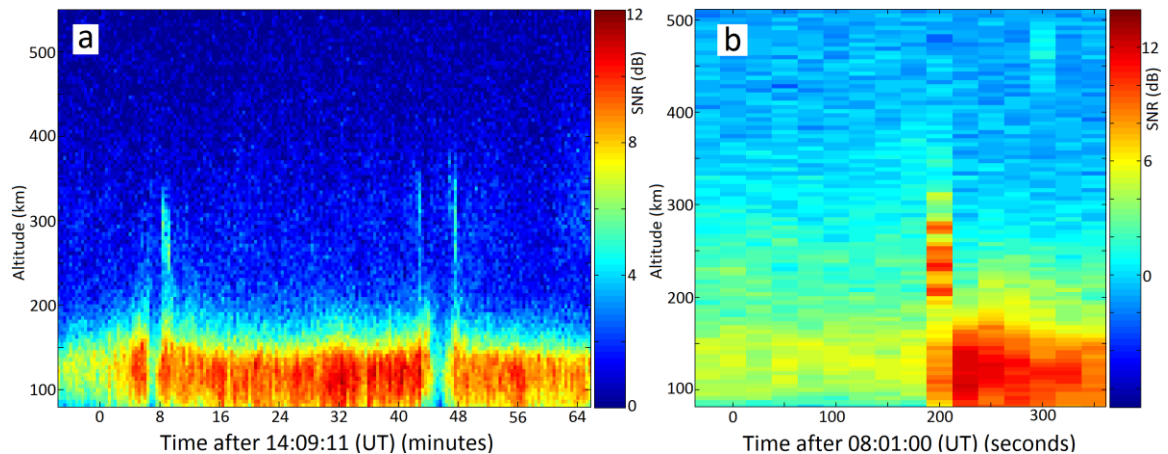


Figure 4.7. Received radar power in the ion line channel as a function of altitude and time, showing occurrences of coherent scatters just outside of periods of E region ionization enhancement due to energetic (keV) electron precipitation (left, 20 February 2012; right, 27 January 2012).

2. Simultaneous Enhancements in the Ion Line and the Plasma Line Channels

In only 11 of our 35 cases were ion line enhancements accompanied by plasma line enhancements in either or both the up- and down-shifted channels, and in only three cases were double-peaked plasma lines (Figure 4.5c) observed. According to Bragg scattering principle a radar only observes a single spatial frequency component k , and so simultaneous observation of Langmuir turbulence in the plasma line and the ion line is only possible if some conditions on intensity and bandwidth of the source are met [*Diaz et al.*, 2010]. However, in cavitating Langmuir turbulence, regardless of the spread in the beam velocity, collapse and dissipation lead to Langmuir wave enhancement over a broad k -space [*Guio and Forme*, 2006; *Goldman*, 1984; *Robinson*, 1997] and thus one would expect to observe the plasma line enhancement in more than 11 examples.

Although plasma line enhancements were absent in 24 out of 35 events, based on the similar characteristics of the echoes with the double-peaked plasma line spectra and those not accompanied by plasma line enhancements, we reasonably conclude that all the observed echoes are manifestation of Langmuir turbulence.

3. Localization of the Echoes in Thin Layers

The enhanced scatters usually appear in thin layers (< 10 km) at the F region peak. In a few events the main layer is accompanied by a secondary thin layer located about 50 km below the main layer. Figure 4.8a plots ion line power from AC measurements on 5 April

2012 at around 7:00 UT. The turbulence is manifested as thin layers of coherent scatter at 260 and 210 km. The upper layer persisted in the radar beam for over five minutes, and the lower layer for almost one minute. This provided sufficient statistics to compute ion line spectra within the turbulence layers at 4.5 km range resolution. Figure 4.8b shows the ion line power spectrum integrated between 4.5 and 5.33 min. The spectra in both layers are similar to Figure 4.3a, but with the altitude smearing removed. Only the upper layer is accompanied by plasma line enhancement. Such double layer profile was observed in six cases out of the observed 35 cases.

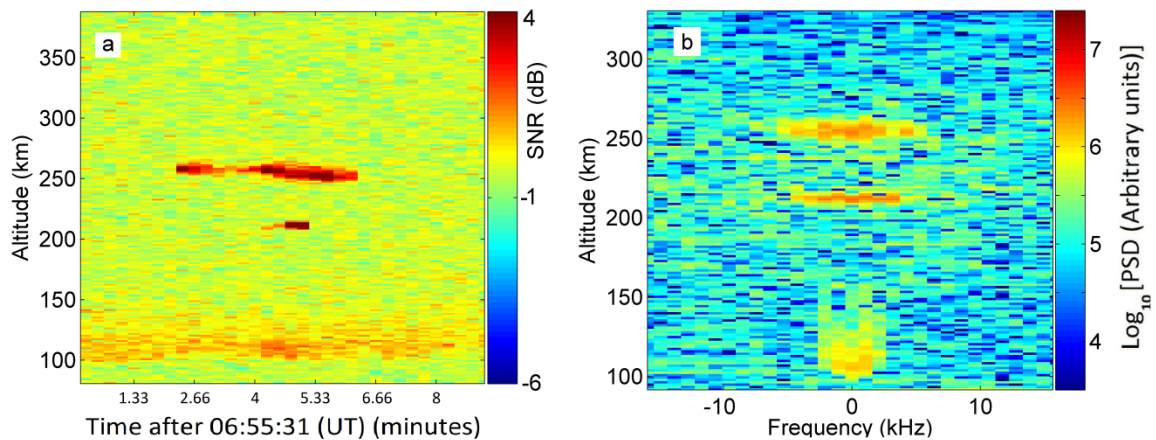


Figure 4.8. (a) Ion line power profile from alternating codes, showing localization of the turbulence in two thin layers. (b) Ion line power spectrum corresponding to Figure 4.8a, integrated between 4.5 and 5.33 min (data from 5 April 2012).

4. Correlation of the Radar Echoes with Natural Electromagnetic Emissions

Figure 4.9a shows the ion line power profile for the Langmuir turbulence event shown in Figure 4.1. Figure 4.9b, from *Bunch et al.* [2008], shows a 0–5 MHz spectrogram of electromagnetic emissions accompanying the auroral activity, recorded with the base antenna at Toolik Lake (about 400 km to the north of PFISR). The horizontal lines are man-made interference signals. The emission labeled “MF burst” is one type of auroral electromagnetic (EM) emissions detectable at ground [*Weatherwax et al.*, 1994; *Kellogg and Monson*, 1979, 1984; *Bale*, 1999]. Coincident with the MF burst, the Toolik receiver also records auroral hiss, a broadband impulsive emission at frequencies below 500 kHz [for a review on auroral EM emissions look at *LaBelle and Treumann*, 2002]. Using a ray tracing technique, *Bunch et al.* [2008] showed that the MF burst originates about 400 km south of the receiver at Toolik Lake, at the approximate location of the PFISR. The orange and the blue bars on Figures 4.9a and 4.9b show the time periods when the electrostatic turbulence and the MF burst, respectively, happen.

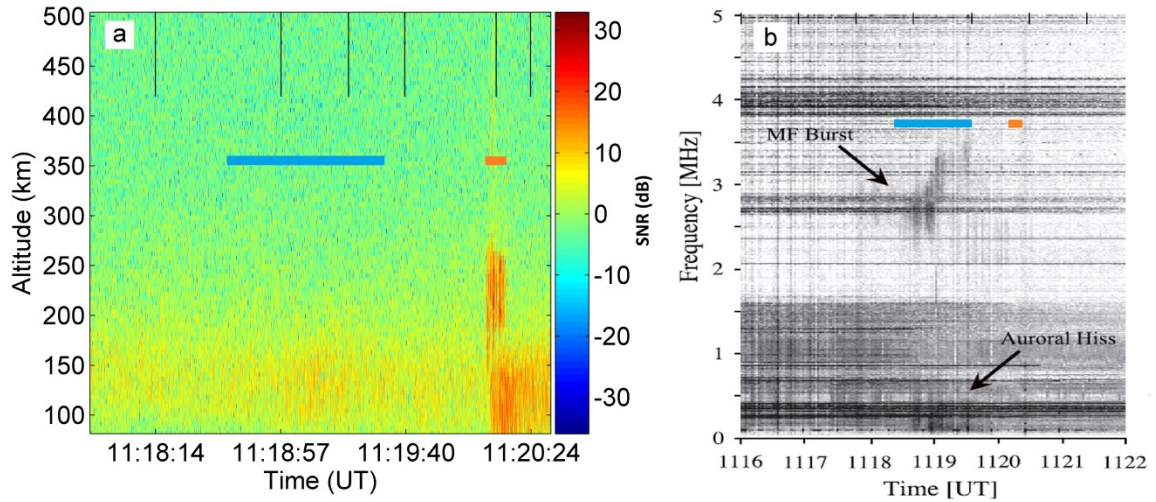


Figure 4.9. (a) Ion line power profile: occurrence of the coherent scatter at 11:20:08 UT, 23 March 2007. (b) Spectrogram of natural electromagnetic emissions accompanying the auroral activity, recorded with the base antenna at Toolik Lake (plot taken from *Bunch et al.* [2008]). The blue and the orange bars specify the time of the features in each panel.

For context, Figure 4.10 shows a sequence of all-sky camera images recorded from Fort Yukon, AK, during this interval. The observations occurred during a substorm expansion phase, with onset point a few hundred kilometers to the west of PFISR at $\sim 11:18$ UT [*Angelopoulos et al.*, 2008]. The image sample times are indicated by vertical black lines in Figure 4.9a, and the PFISR location is indicated by a red circle in Figure 4.10. The onset of Langmuir turbulence echo corresponded with an auroral brightening and subsequent breakup at $\sim 11:20$ UT (Figures 3.10d–3.10f). Analysis of high-speed imagery from Poker Flat at this time suggests the presence of dispersive-scale Alfvén waves within the PFISR beam [*Semeter and Blixt*, 2006; *Semeter et al.*, 2008]. Nonlinear evolution of inertial Alfvén waves provides one mechanism for producing the high-

density, low-energy electron beams required for inducing cavitating Langmuir turbulence [Mishin and Banaszekiewicz, 1998; Mishin and Förster, 1995].

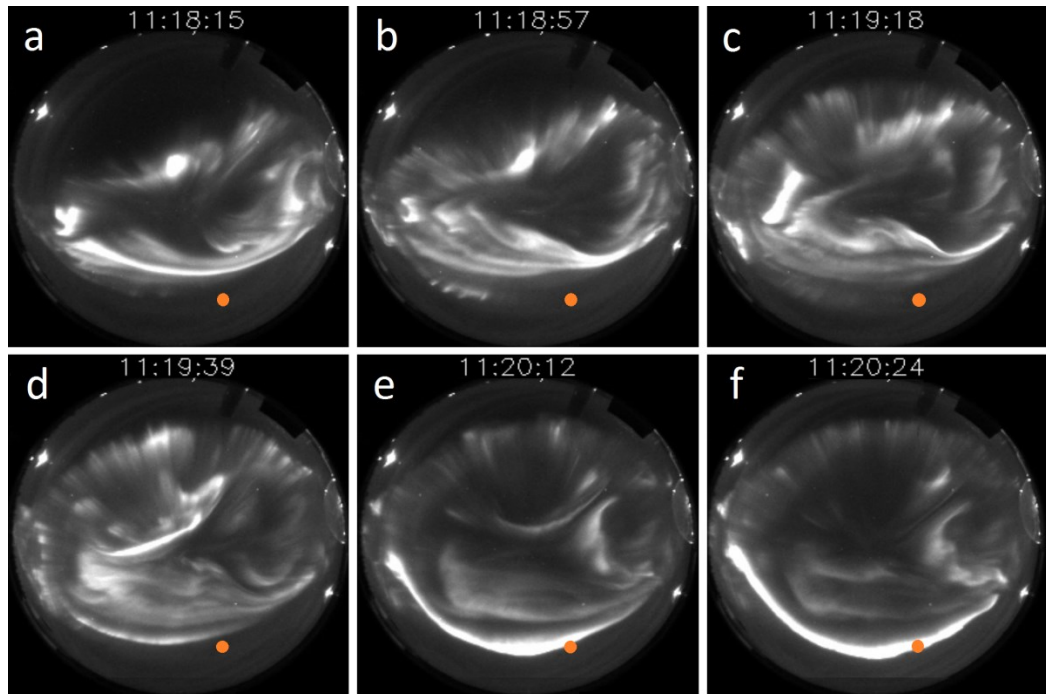


Figure 4.10. A sequence of all-sky camera images recorded from Fort Yukon, AK. The image sample times are indicated by vertical black lines in Figure 4.9a, and the PFISR location is indicated by a red circle in Figure 4.10.

Figure 4.11, in the same format as Figure 4.9, shows another example of simultaneous measurements of PFISR echoes and natural EM emissions recorded at Toolik Lake. Four types of EM emissions occur sporadically during the approximately one hour interval shown in Figure 4.11b: 2fce and 3fce auroral roars, which are narrowband emissions near 2.9 and 4.0 MHz presumed to result from upper hybrid waves; auroral hiss at frequencies below 1 MHz; and auroral MF burst, including four bursts exceeding 2 min duration and

spanning approximately 2.9–3.3 MHz. Two of the three radar echoes detected with the PFISR, centered approximately at 8:49 and 9:03 UT, coincide with two of the four MF bursts. In the latter case, auroral hiss occurs at the same time as well. The probability of these coincidences happening by chance is about 5%; this level of coincidence is all the more surprising considering that Toolik Lake is located more than 400 km from the PFISR, and MF burst occurrence at ground level is severely affected by propagation effects in the disturbed auroral ionosphere.

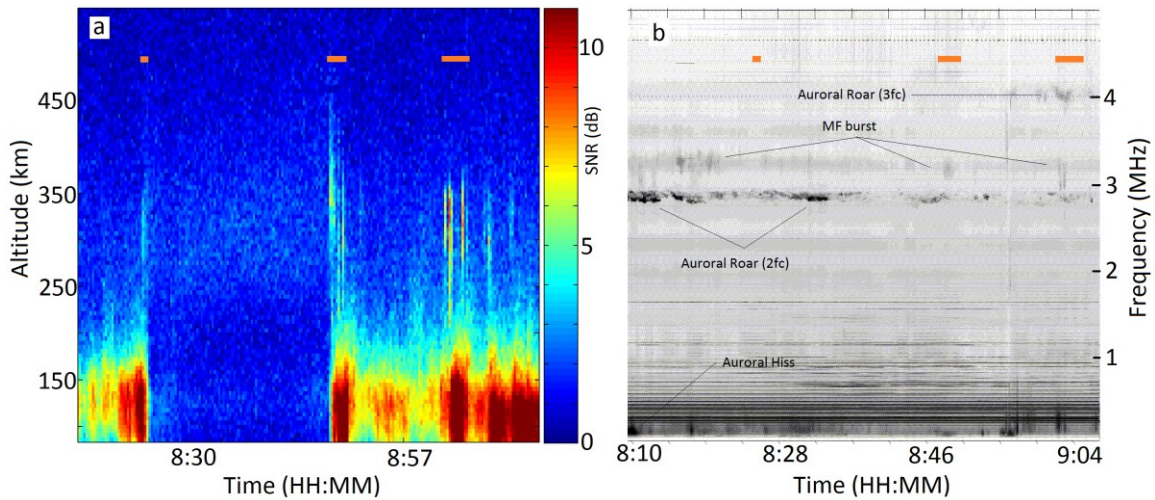


Figure 4.11. Similar to Figure 4.9: (a) ion line power profile and (b) spectrogram of natural electromagnetic emissions. For convenience the time interval of three coherent scatters are marked by orange bars in both panels. (Data from 5 April 2012).

5. Asymmetric Plasma Line Spectra: Evidence for Existence of other Wave Modes

In a few events asymmetric peaks in up- and down-shifted plasma line spectra were observed. Figure 4.12 shows an example. In Figure 4.12a an ion line range-time-intensity

plot produced from a separate one-baud-length pulse that was added to the AC pulses is shown. In this panel, in addition to incoherent scatter from the enhanced E region ionization (the enhancements below 150 km) due to energetic electron precipitation, coherent echoes are also present in thin layers close to the F region peak at ~ 250 km. Figure 4.12b shows the up- (blue) and down-shifted (red) plasma line spectra produced by the long pulse measurements for record 16 in Figure 4.12a. The spectra are averaged over a 70-km range gate centered at 290 km. The up-shifted channel consists of a peak at 3.8 MHz and a peak at ~ 3.5 MHz, while the down-shifted channel consists of a peak at 3.8 MHz and a peak at ~ 4.1 MHz. The spectra for lower altitudes (at 250 and 210 km) only consist of the peaks at 3.8 MHz. The 3.8-MHz peaks commonly exist at other records in Figure 4.12a, where coherent echoes are seen in the corresponding ion line channel. However, the peaks at 3.5 and 4.1 MHz only exist in records 16 and 10. For record 10 where the echoes have almost disappeared in the ion line channel, the plasma line spectra still show the peaks at 3.8 MHz as well as the peak ~ 3.5 MHz in the up-shifted channel; however the peak at ~ 4.1 MHz in the down-shifted channel is absent. In addition to these features, weak signs of double-peaked spectra similar to that in Figure 4.5c are seen in records 7, 8, and 9 in the up-shifted channel, but are not pronounced in the down-shifted channel. In all of the five records which plasma-lines were enhanced, the enhancements were relatively more pronounced in the up-shifted channel.

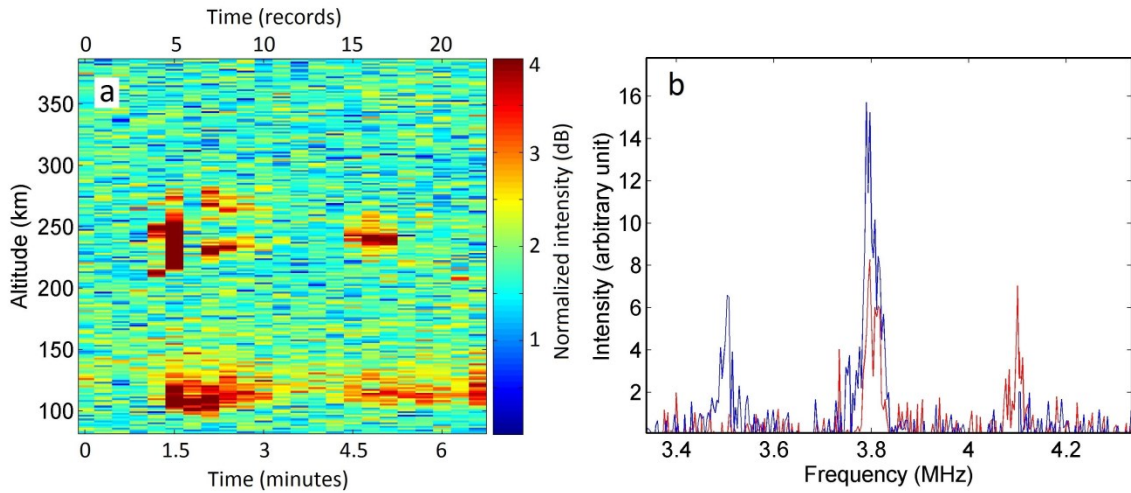


Figure 4.12. Panel a: ion line range-time-intensity (RTI) plot derived from a separate one-baud-length pulse that accompanied AC. The time axis is shown in minutes as well as in 16-second intervals (records) starting at 6:04:35 (UT). Coherent echoes are originating from thin layers close to the F region peak (~ 250 (km)). Panel b: up- (blue) and down-shifted (red) plasma line spectra produced by long pulse measurements for record 16 in Panel a. The spectra are averaged over a 70-km range gate centered at 290 (km).

In Figure 3.12 we conclude that the peaks at 3.8 MHz are produced by the waves that are directly connected to Langmuir turbulence. The two extra peaks at 4.1 and 3.5 MHz, however, require explanation. The frequency offset of ~ -300 kHz of the secondary peak with respect to the main peak in the up-shifted channel, and the matching positive frequency offset in the down-shifted channel, confirms that the peaks are not produced as a result of spatial/temporal averaging. This rather suggests that the peaks are produced by non-linear interactions between Langmuir waves and a secondary wave. A variety of electrostatic and electromagnetic modes exist and have been observed in the ionosphere

during disturbed periods [*Andre*, 1997; *LaBelle* and *Treumann*, 2002; *Samara* and *LaBelle*, 2006]. Determining which of these modes are responsible for the asymmetric spectra presented here would also provide further insights into source mechanisms for the Langmuir turbulence.

4.4 Propagation Effects on Saturation of Langmuir Waves

Typically, magnetospheric electron beams are assumed to be directly responsible for high-frequency ionospheric turbulence and their signatures in radar data. The electrons are assumed to be accelerated at much higher altitudes (~ 6000 km) and propagate downward to the observation altitudes, interacting with the ionospheric plasma along the way. Therefore, localization of the echoes, i.e. turbulence, in thin layers seems inconsistent with this mechanism. A careful examination of the PFISR data reveals that this localization cannot be explained as an ISR wave number matching effect.

Enhancement of both up- and down-shifted plasma lines at wave number $k = 19$ (m^{-1}) (the spatial frequency component observable by the PFISR) requires parametric decay of either up- or down-going Langmuir waves at wave number $k \approx 19$ (m^{-1}). On the other hand, enhancement of ion acoustic lines at wave number $k = 19$ (m^{-1}) requires parametric decay of Langmuir waves with wave number $k \approx 10$ (m^{-1}). This broad enhancement in k -space, at a single altitude, implies a large velocity spread and/or a large intensity of the electron beam which, in turn, guarantees that the PFISR wave number

matching conditions are met over an altitude range that far exceeds the width of the observed turbulence layer. In an extreme case, it is possible that the highest wave number of the enhanced Langmuir waves in the top layer is $k = 19 \text{ (m}^{-1}\text{)}$; as the beam propagates downward to a region of lower plasma density, it amplifies Langmuir waves at lower wave numbers ($k < 19 \text{ (m}^{-1}\text{)}$). Such waves are invisible to the radar and consequently the radar only sees a localized plasma line enhancement. However, given the large velocity spread of the beam, ion acoustic waves produced by parametric decay of such invisible Langmuir waves should be visible to the radar. Therefore, we conclude that the observed localization of the ion line enhancement in thin layers implies localization of the turbulence.

Several mechanisms have been proposed that can lead to localization of turbulence in thin layers. *Mishin and Schlegel* [1994] used the theory of plasma turbulence layer to explain, ISR observations of intense Langmuir wave enhancements within layers with altitude extent less than the ionospheric scale heights in auroral E region. This mechanism requires relatively sharp variation of collision frequency with altitude and thus is not applicable to our F region observations. Plasma waves being trapped in small scale ($\sim \text{km}$) density cavities or enhancements are also proposed to explain some rocket observations of intense localized wave enhancements [*McAdams et al.*, 2000]. Amplification of plasma waves not only depends on the growth rate, which is mainly determined by the source characteristics, i.e., auroral electron distribution function, but also depends on growth time—i.e., the time period in which the wave stays resonant with the source, which is typically determined by the ambient plasma and the wave's

dispersion relation. In the auroral ionosphere, often latter is the critical factor that limits the wave amplification [Maggs, 1978]. In such situations, wave trapping in density enhancements or cavities provides further amplification by allowing the wave to stay resonant for a longer period. Small scale density cavities capable of trapping the Langmuir waves cannot be resolved with our long range-resolution ISR data and therefore their possible roles in the localization of the turbulence in thin layers cannot be investigated.

Investigating the ionospheric background plasma parameters reveals that the altitude characteristics of the echoes may be explained via the ionospheric electron density profile. Similar to Figure 4.8a, Figures 4.13a and 4.14a present other examples of AC measurement of two turbulence layers. Also shown in each figure is the background electron density profile. The incoherent scatter measurement period that is used to calculate the density profiles are marked by the color bars in the left panels and the location of the turbulence layers with respect to the electron density profiles are specified by the horizontal bars on the right panels. The shaded area around the density profiles represents error bars and statistical accuracy of the calculations. Interestingly, the turbulence layers are located at regions of minimal density gradient, where the effect of propagation in limiting the Langmuir energy is minimal.

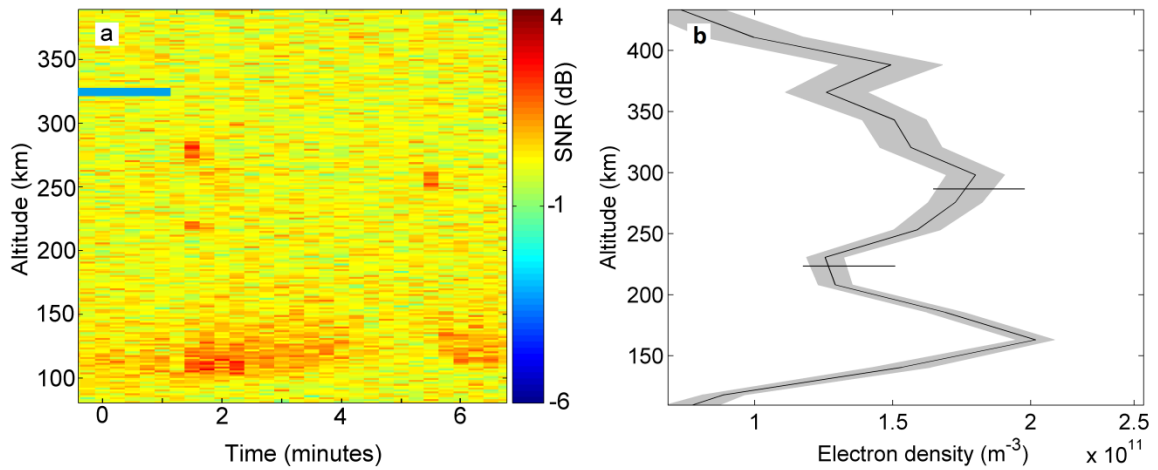


Figure 4.13. (a) Ion line power profile from the alternating codes, showing the localization of turbulence in two thin layers. (b) Background electron density profile averaged over the incoherent scatter measurement period marked by the blue bar in the left panel. Shaded area represents the statistical accuracy of the measurements (one standard deviation). The two horizontal bars show the location of the two layers with respect to the background density (Data from 17 March 2012).

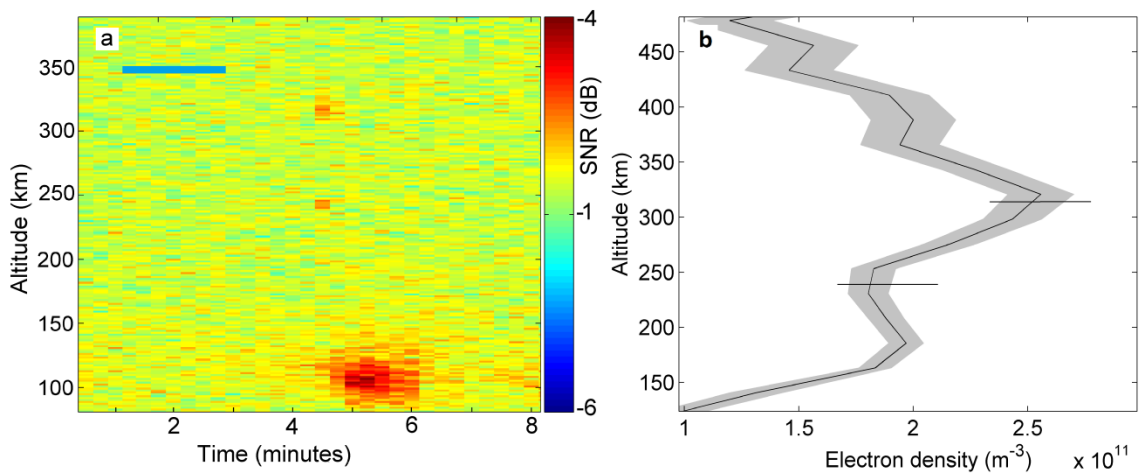


Figure 4.14. Similar to Figure 4.13, (a) another example of the double-layer profile

observed in the ion line channel, and (b) locations of the layers with respect to the background electron density (Data from 5 April 2012).

It can be argued that, in the presence of density gradient, propagation of Langmuir waves leads to change in the phase velocity and consequently detuning the waves from the electron beam and limiting the amplitude of the waves. Our calculations for altitudes between the two turbulence layers in Figure 4.8a, where the density gradient is highest with linear-scale height of ~ 200 km, shows that the Langmuir waves generated by a down-going electron beam with energy of 100 eV and beam velocity spread of $\Delta v = 0.3v$, only propagate 500 m until they become off-resonant with the beam. Given the calculated $22.5 \frac{\text{km}}{\text{s}}$ group velocity of such waves, the total resonant time is about 22 ms. In fact the exact resonant time is even less. As the wave propagates down the density gradient its phase velocity decreases and the group velocity increases according to $v_g = \frac{3KT_e}{m_e v_\phi}$, decreasing the total resonant time. Here v_g , v_ϕ , m_e , K , and T_e are the wave's group velocity, phase velocity, electron mass, Boltzmann constant, and electron temperature, respectively. Furthermore, during this time the wave is not being amplified by the highest possible growth rate. On the other hand, propagation of the Langmuir waves with constant group velocity of $22.5 \frac{\text{km}}{\text{s}}$ in a 5 km long region of zero density gradient, at the location of the turbulence layers, ensures that the waves remain resonant with the beam, with the highest possible growth rate, for at least 220 ms. The required resonant time for the Langmuir waves to reach the nonlinear regime depends on the growth rate and the beam parameters, however, for reasonable auroral electron beams and

neglecting the propagation effects this time is in the order of tens of milliseconds [*Guio and Forme, 2006*]. Therefore, with such electron beams, propagation effects may be able to limit the Langmuir waves' amplitude in the regions between the two turbulence layers, preventing them from reaching the nonlinear regime. However, in the region of zero density gradient the Langmuir waves can reach to high intensities and develop the turbulence layers.

In comparison with the 100 eV beam, Langmuir waves resonant with a lower energy beam need to propagate longer distances, in the same density gradient, to become off-resonant. For instance, for beams with mean energy of 20 and 4.6 eV and velocity spread of $\Delta v = 0.3v$ the resonant distances and times are, 3 and 12 km and 57 and 112 ms, respectively (calculated for linear-scale height of ~ 200 km). Therefore, for higher energy beams one would expect to observe enhancements more localized in altitude in ISR data. Note that in the case of higher energy beams (> 20 eV) the mother Langmuir wave and Langmuir and ion acoustic waves produced by cascading Langmuir turbulence are all invisible to the radar, and observation of the turbulence with the radar requires a mechanism capable of transferring energy to higher wave numbers, i.e., cavitating Langmuir turbulence.

The above explanation is also consistent with the simultaneous measurements of the radar echoes and MF burst. MF burst, an impulsive broadband emission at 1.3–4.5 MHz associated with the onset of auroral substorms, is one type of auroral EM emissions detectable at ground [*Weatherwax et al., 1994*]. The generation mechanism of MF

bursts remains unclear, but the prevailing theory involves linear mode conversion of Langmuir or upper hybrid waves driven by auroral electron beams or loss cone features over an extended altitude range on the bottom-side F region [*LaBelle et al.*, 1997, 2005]. Other theories involve nonlinear conversion of electron acoustic or electron cyclotron sound waves into broadband electromagnetic emissions [*Sotnikov et al.*, 1996; *Bunch et al.*, 2011]. *Bunch et al.* [2011] found all the mechanisms mentioned above to be viable based on consideration of conditions for resonance between auroral electrons and either wave mode.

LaBelle [2011] considered another possibility, that MF burst is produced by linear mode conversion of Langmuir waves, driven by low-energy beams (\sim few hundred eV) on the topside F region, to LO mode. In this model, Langmuir waves propagate downward to regions of higher plasma density implying that their wave number decreases. After a short distance, Langmuir waves propagating parallel to magnetic field lines and linearly convert to downward propagating L mode waves. Below the F region peak, the L mode waves encounter decreasing plasma density as they propagate and their wave number increases. Upon reaching the conversion point some portion of the waves that propagate parallel to the magnetic field lines converts back to Langmuir waves and the rest freely propagate to the ground as MF burst. In this model low-energy ($<$ keV) electron beams are assumed as the energy source because they fit more properly with the shape of the fine structures present in MF burst [*LaBelle*, 2011].

Simultaneous measurement of Langmuir turbulence and MF burst, and their correlation with soft (< 500 eV) electron precipitations, not only supports our explanation for localization of the echoes but also provides evidence in support of the mechanism proposed by LaBelle [2011]. The offset in timing between the MF burst and the UHF turbulence is not surprising given the dynamic nature of the event and the differences in fields-of-view and observing geometry for the two instruments.

Chapter 5

Langmuir Turbulence: Zakharov Simulations

It was shown in the previous chapter that the observed radar echoes that were identified as signatures of Langmuir turbulence were associated with dynamic auroral features. This suggests that the magnetospheric-origin electron beams provide the free energy for the natural turbulence via the bump-on-tail instability. ISR observations of the echoes therefore motivated us to revisit the topic of beam-generated Langmuir turbulence in the F region ionosphere through simulations with the goal of regenerating the observed radar data and gaining insight into the nature of the source electron beams. In particular, the main goals of the simulations were 1) to identify the source parameters, i.e. parameters of the electron beams (such as electron number density, energy, and temperature) that are generating the ISR-detectable Langmuir turbulence and 2) to investigate the roots of the discrepancies in the heater-induced and natural ion line spectra.

Beam-generated Langmuir turbulence has been the subject of experimental and simulation studies in the solar wind plasma [*Nicholson et al.*, 1978], lower solar corona [*Goldman and Newman*, 1994], planetary foreshocks [*Gurnett et al.*, 1981; *Robinson and Newman*, 1991], and the topside auroral ionosphere [*Newman and Goldman*, 1994a and b]. However, it has been shown through many simulations that the development and dynamics of the turbulence are strong functions of many parameters such as the level of background density perturbations, magnetic field strength, damping rates for ion-acoustic and Langmuir waves, as well as the parameters of the source [*Newman et al.*, 1994a and

b; *Robinson et al.*, 1992; *Robinson and Newman*, 1989]. It is thus plausible that the dynamics of the turbulence at the lower auroral ionosphere is different from those observed before and unique to this region.

This chapter presents simulation results where electron beams with different set of parameters applicable to the F region ionosphere are considered as the source of free energy. The studied parameter regime is extended by more than two orders of magnitude in average energy and electron number density of the beams. The results suggest that magnetospheric-origin electron beams could not entirely be responsible for the turbulence and that a local energization mechanism close to the observation altitudes is most likely involved [*Akbari et al.*, 2014]. A range of very dynamic nonlinear interactions is observed for the different sets of beam parameter.

The next section presents the mathematical framework that is often used to simulate Langmuir turbulence.

5.1 Zakharov Equations

It has long been recognized that Langmuir turbulence in unmagnetized [*Goldman*, 1984; *Robinson et al.*, 1988] and weakly magnetized [*DuBois et al.*, 1990; *Robinson and Newman*, 1990; *Newman et al.*, 1994b] plasmas (conditions concerned in this work with ω_p (plasma frequency) $\approx 4 \omega_c$ (electron cyclotron frequency)) can be modeled by the Zakharov system of equations. The electrostatic Zakharov system of equations is a set of

non-linear, stochastic partial differential equations (PDE) and is derived by solving continuity, momentum, and Poisson equations for electron fluid and continuity and momentum equations for ion fluid under the assumption of quasi-neutrality. When solving the equations for the electron fluid one should have in mind that in addition to the high frequency component the electron density consists of a low frequency component that accounts for the low frequency ion density fluctuation. When solving for the ion fluid, one should note that in the presence of a non-uniform electric field charged particles are subject to the nonlinear Ponderomotive force that acts due to the gradient in the electric field intensity. Therefore, an additional term $F_{PM} = \frac{e^2}{m_e \omega_p^2} \nabla |E|^2$ exists in the momentum equation. Here, e and m_e are the electron charge and mass.

Numerical works in one and two dimensions [Rowland *et al.*, 1981] have shown that for a spectrum of Langmuir waves with small angular spread, such as those generated by the bump-on-tail instability, the interactions, at least until the initial stage of the caviton formation, can be investigated in one dimension. Moreover, in-situ observations of beam-generated Langmuir turbulence in the topside auroral ionosphere have shown that the generated waves dominantly propagate with angles less than 10 degrees from the direction of the beam [Newman *et al.*, 1994a]. Therefore, without undermining the possible effects of transverse modes on the turbulence, in this work we restrict our attention to one-dimensional simulations since this enables wider parameter ranges to be studied with reasonable simulation length and temporal/spatial resolutions.

Following the standard derivation for electron and ion fluids in one dimension we derive:

$$\left(i \frac{\partial}{\partial t} + \frac{3}{2} \omega_p \lambda_D^2 \frac{\partial^2}{\partial x^2}\right) E = \frac{\omega_p}{2} \frac{n}{n_0} E \quad (4.1)$$

$$\left(\frac{\partial^2}{\partial t^2} - C_s^2 \frac{\partial^2}{\partial x^2}\right) n = \frac{\epsilon_0}{4m_i} \frac{\partial^2 |E|^2}{\partial x^2} \quad (4.2)$$

Where n is the total low-frequency ion density fluctuation and E is the slowly varying envelope of the electric field. The total high-frequency electrostatic field in terms of the slowly varying envelope is given by $\mathcal{E} = \frac{1}{2}[E \exp(-i\omega_p t) + E^* \exp(i\omega_p t)]$. Other quantities are: n_0 , background plasma density; $C_s = \frac{\eta m_e}{m_i} v_e^2$, the sound speed; $\eta = \frac{T_e + 3T_i}{T_e}$; $v_e^2 = \frac{k_B T_e}{m_e}$; and T_i , ion temperature. Removing the nonlinear terms on the right hand side of equation 4.2 and replacing the temporal and spatial derivatives by $-i\omega$ and ik , respectively, result in the familiar dispersion relation $\omega^2 = C_s^2 k^2$ for the ion acoustic waves.

Plasma waves are spontaneously generated, by random fluctuations of charged particles, and damped, by Landau damping. In the above equations spontaneous emission of Langmuir and ion acoustic waves can be modeled by adding source terms in the form of independent complex Wiener/Brownian motion processes (S_E and S_n) to the right hand sides of the equations. Landau damping can also be accounted for by including damping coefficients ϑ_e and ϑ_i in the derived equations. The damping terms include kinetically determined linear Landau damping of Langmuir and ion acoustic waves, γ_L and γ_{IA} respectively, and the electron and ion collision frequencies, ν_{ec} and ν_{ic} , and are given by $\vartheta_e = -\frac{\nu_{ec}}{2} + \gamma_L$ and $\vartheta_i = -\frac{\nu_{ic}}{2} + \gamma_{IA}$ [Guio and Forme, 2006] where

$$\gamma_{IA} = -\sqrt{\frac{\pi}{8}} \left[\left(\frac{m_e}{m_i} \right)^{\frac{1}{2}} + \left(\frac{T_e}{T_i} \right)^{\frac{3}{2}} \exp \left(-\frac{T_e}{2T_i} - \frac{3}{2} \right) \right] |k| C_s \quad (4.3)$$

$$\gamma_L = \frac{\pi}{2n_0} \frac{\omega_p^2}{k^2} \omega_L \left[\frac{df(v)}{dv} \right]_{\omega_L/k} \quad (4.4)$$

Here $f(v)$ is the one-dimensional electron distribution function that consists of the background thermal electrons as well as the beam electrons that provide the free energy for the turbulence through inverse Landau damping, i.e. bump on tail instability. For thermal and beam electron populations we assume separate Maxwellian distributions. The entire electron distribution function is thus identified by electron number density (n), mean drift velocity (u), and thermal velocity or temperature (θ) for thermal and beam electron populations.

Including the stochastic source and damping terms in equations 4.1 and 4.2 we derive:

$$\left(i \frac{\partial}{\partial t} + i\vartheta_e \times + \frac{3}{2} \omega_e \lambda_D^2 \frac{\partial^2}{\partial x^2} \right) E = \frac{\omega_e}{2} \frac{n}{n_0} E + S_E \quad (4.5)$$

$$\left(\frac{\partial^2}{\partial t^2} + 2\vartheta_i \times \frac{\partial}{\partial t} - C_s^2 \frac{\partial^2}{\partial x^2} \right) n = \frac{\epsilon_0}{4m_i} \frac{\partial^2 |E|^2}{\partial x^2} + S_n \quad (4.6)$$

Where \times denotes the convolution product operator, since the damping coefficients are given for single wavenumbers, i.e. spatial Fourier components of E and n . Assuming a one-dimensional simulation space of length L and periodic boundary condition, the equations can be solved by the pseudo spectral method where E and n are decomposed to their Fourier components:

$$E(x, t) = \sum_{k=-N/2}^{N/2-1} \hat{E}_k(t) \exp(i2\pi kx/L) \quad (4.7)$$

$$n(x, t) = \sum_{k=-N/2}^{N/2-1} \hat{n}_p(t) \exp(i2\pi kx/L) \quad (4.8)$$

Here N is the number of discrete wave numbers. Inserting equations 4.7 and 4.8 into equations 4.5 and 4.6, replacing the spatial derivatives with ik , breaking the second order PDE in terms of first order PDEs, and finally rewriting the result equations in their update Langevin form $dX = F(X, t)dt + G(X, t)dW$, where $dW = \sqrt{dt} [N_1(0,1) + i N_2(0,1)]$ is a complex Wiener process with independent real and imaginary parts, we drive:

$$d\hat{E}_k(t + dt) = \left[\left(-\vartheta_e - i \frac{3}{2} \omega_e \lambda_D^2 k^2 \right) \hat{E}_k(t) - i \frac{\omega_e}{2n_0} (\hat{n}\hat{E})_k \right] dt + A_k dW_1(t) \quad (4.9)$$

$$d\hat{n}_k(t + dt) = \hat{n}_k(t)dt + B_k dW_2(t) \quad (4.10)$$

$$d\hat{n}_k(t + dt) = \left[-2\vartheta_i \hat{n}_k(t) - k^2 \left(C_s^2 \hat{n}_k(t) + \frac{\epsilon_0}{4m_i} |\hat{E}_k|^2 \right) \right] dt \quad (4.11)$$

A_k and B_k are weighting constants that equal the steady state solutions of the equations to the thermal levels of the electric field and density perturbations in the ionosphere in the absence of the beam electron population. We now solve equations 4.9, 4.10, and 4.11 by 4th order stochastic Runge-Kutta method. For simulations presented here we consider 70-100 m long plasma, time resolution of 0.1 μ s, and $N = 2048 - 4096$ spatial Fourier components; and apply one-third zero padding to avoid spectral aliasing.

5.2 Simulation Results

5.2.1 Dynamics of Langmuir Turbulence

This section discusses dynamics of the interactions between high-frequency Langmuir waves and low-frequency ion density perturbations as the parameters of the source electron beam changes. As will be discussed, a variety of processes, ranging from a single parametric decay, to a cascade of parametric decays, to formation of stationary wave packets and density cavities in the condensate region that may lead to collapse, and to direct collapse at initial stages of the turbulence, occurs as the input energy to the system increases.

Inputs to the simulator are parameters of the background plasma as well as parameters of electron beams that provide the free energy for the system. For the background plasma we consider the typical parameters of the F region peak. These are: electron temperature $T_e = 3000 K^\circ$; ion temperature $T_i = 1000 K^\circ$; electron density $n_0 = 5 \times 10^{11} (m^{-3})$; electron-neutral collision frequency $\nu_{ec} = 100 (s^{-1})$; ion-neutral collision frequency $\nu_{ic} = 1 (s^{-1})$; and we assume the plasma only consists of atomic Oxygen ions. Assuming Maxwellian distribution function, the beam electron population can be identified by beam's electron number density (n_b), mean drift velocity (V_b) or equivalently mean energy of the precipitating electrons ($E_b = \frac{1}{2} m_e V_b^2$), and beam's velocity spread or temperature (ΔV_b). The parameter regimes that we studied are: electron number density ratio $10^{-7} \leq \frac{n_b}{n_0} \leq 2.5 \times 10^{-5}$; average beam energy $40 eV \leq E_b \leq 2 keV$; and beam velocity spread $\Delta V_b = 0.3 V_b$. The upper bound for the average beam energy has been chosen with regard to the fact that the radar echoes are found to be

correlated with soft electron precipitations and the lower bound has been chosen with regard to the observation altitudes (~ 250 km). Precipitating electrons with yet lower energies will be collisionally stopped at higher altitudes and cannot reach to the observation altitudes [Fang *et al.*, 2008]. Also the chosen beam velocity spread is the typical value for the ionospheric electron beams.

Below, simulations results derived for three sets of beam parameters are presented. The three selected beam parameters, and the resulting turbulence dynamics, are good representatives of the many sets of beam parameters that we studied. The presented results provide a clear picture of Langmuir turbulence that is believed to be responsible for the radar echoes that were presented in Chapter 4.

1. Simulation One: $\frac{n_b}{n_0} = 30 \times 10^{-7}$ and $E_b = 125$ eV

For electron number density ratios $\frac{n_b}{n_0} \sim 10^{-7}$ the growth rate of the resonant Langmuir waves, given by equation 4.4, is small and the waves do not reach to the nonlinear regime within the 100 ms simulation time. In fact, such waves would most likely never reach to the nonlinear regime in the ionosphere. That is because in the presence of background density gradient the waves' amplitude would most likely be saturated by propagating out of resonant with the beam within such a long time period. As we increase the electron number density ratio the growth rate increases and the waves may reach to high intensities before they are saturated by other processes. Figure 5.1 shows the result of the simulation for one set of beam parameters ($\frac{n_b}{n_0} = 30 \times 10^{-7}$ and $E_b = 125$ eV). The left

and right panels show the evolution of the electric field and the ion-density perturbations, respectively, as a function of time and wave number. The positive or negative sign for wave numbers determines the propagation direction of the waves. The asymmetric enhancement at $k \sim -8 \text{ (m}^{-1}\text{)}$ for $t < 67 \text{ (ms)}$ in the electric field spectrum, therefore, means that only Langmuir waves propagating in the direction of the electron beam are enhanced. These are the Langmuir waves for which the damping coefficient ϑ_e is positive due to the inverse Landau damping. It is seen that once the waves with the highest growth rate at $k \sim -8 \text{ (m}^{-1}\text{)}$ reach to high intensities they decay to counter propagating Langmuir waves (L_1) at $k \sim +7.1 \text{ (m}^{-1}\text{)}$ and ion acoustic waves (S_1) at $k \sim 15.1 \text{ (m}^{-1}\text{)}$ (in Figure 4.1b). Soon after the first PDI the second (L_2, S_2), third (L_3, S_3), and the fourth (L_4, S_4) parametric decays occur and energy quickly transfers to lower wave numbers. For the plasma parameters used in this simulation we drive $k^* \approx 0.9 \text{ (m}^{-1}\text{)}$ and we verify that the matching conditions $K \approx 2k - k^*\hat{k}$ and $\hat{k} \approx -k + k^*\hat{k}$ are satisfied in Figure 5.1.

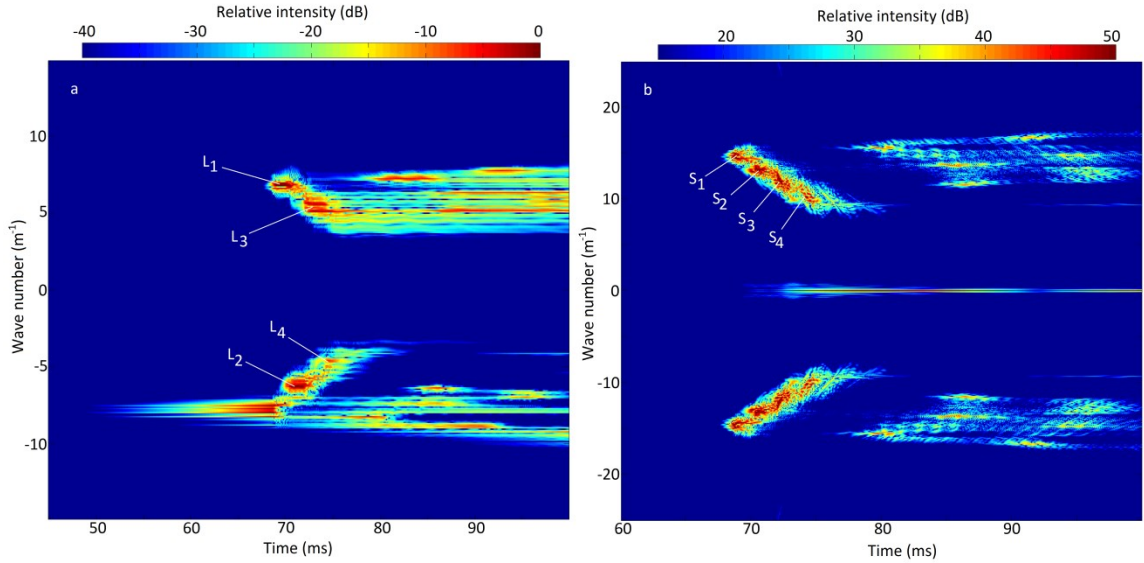


Figure 5.1. The left and right panels show the evolution of the electric field and the ion density perturbations, respectively, as a function of time and wave number for the beam parameters of $\frac{n_b}{n_0} = 30 \times 10^{-7}$ and $E_b = 125 \text{ eV}$ which has been applied at time $t = 0 \text{ ms}$.

In Figure 5.1b note that, since equation 4.6 is independent of the sign of k , the modal spectrum is symmetric around $k = 0$ for the ion density perturbations and therefore the down- and up-going ion acoustic waves are not distinguishable in this figure. Moreover, note that the generated ion acoustic waves are fairly short lived due to the strong Landau damping and the waves damp away shortly after the PDI stops operating at the corresponding wave numbers. This can be seen more clearly in Figure 5.2 that shows the density fluctuations in real space as a function of time. Here the ion acoustic waves propagating with the sound speed (slope of the patterns in space-time domain) in positive

and negative directions as well as a standing wave pattern produced by collocated counter propagating waves are seen.

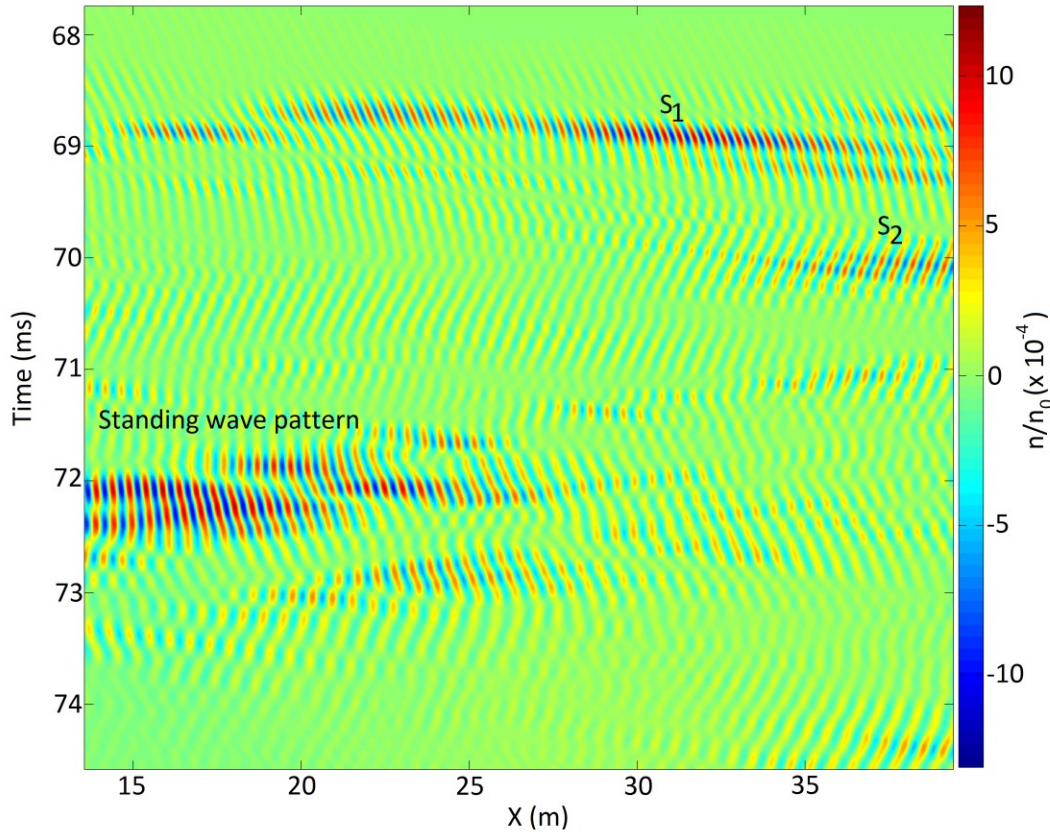


Figure 5.2. Normalized density fluctuations of Figure 5.1 in real space as a function of time. S_1 and S_2 are the ion acoustic waves produced by the first and the second PDI in Figure 5.1

In Figure 5.1b in addition to the enhancements produced by the parametric decay, enhancements at small wave numbers ($k \sim 0$) are also seen that are produced by beat modulation between the intense Langmuir waves that locate close to each other on the Langmuir dispersion curve. Such density enhancements follow their own dispersion

relation and will be discussed later. The three-wave coalescence, by which the interaction of a Langmuir wave $L_1(\omega, k)$ and an ion acoustic wave $S(\Omega, K)$ gives rise to a Langmuir wave $L_2(\omega + \Omega, k + K)$, is another process that is expected in the presence of strong Langmuir and ion acoustic waves. This process is secondary compared to the PDI and thus its product waves are not visible in Figure 5.1 due to the chosen scale for the plot; however, are visible in Figure 5.3 that shows the same data but for a broader range of wave numbers and intensities. In Figure 5.3a Langmuir waves at $k_0 \approx -8 \text{ (m}^{-1}\text{)}$ (labeled as $L@k_0$), Langmuir waves at $k \approx +|k_0|$ (labeled as $L@-k_0$), and ion acoustic waves at $k \approx 2k_0$ (labeled as $S@2k_0$) are produced by the direct interaction with the electron beam and parametric decay. These are the same enhancements as in Figure 5.1. The three-wave coalescence of $L@-k_0$ and $S@-2k_0$ then gives rise to the Langmuir enhancements at $k \approx -3k_0$ (labeled as $L@-3k_0$) which subsequently decay into Langmuir waves at $k \approx k_0$ and ion density waves at $k \approx -4k_0$. The newly generated ion density waves participate in a three-wave coalescence interaction with the most intense Langmuir waves to produce Langmuir enhancement at yet higher wave numbers, which are, in turn, subject to decay generating ion density enhancements at yet higher wave numbers. A series of such interactions ultimately gives rise to the enhancements seen in Figure 5.3. It is important to note that although the products of the three-wave coalescence and beat modulations are orders of magnitude weaker than the waves produced by the PDI, are yet orders of magnitude more intense than the background thermal waves. Such interactions might be, therefore, detectable by Incoherent Scatter Radars since ISRs are sensitive to wave activities at a single wave numbers.

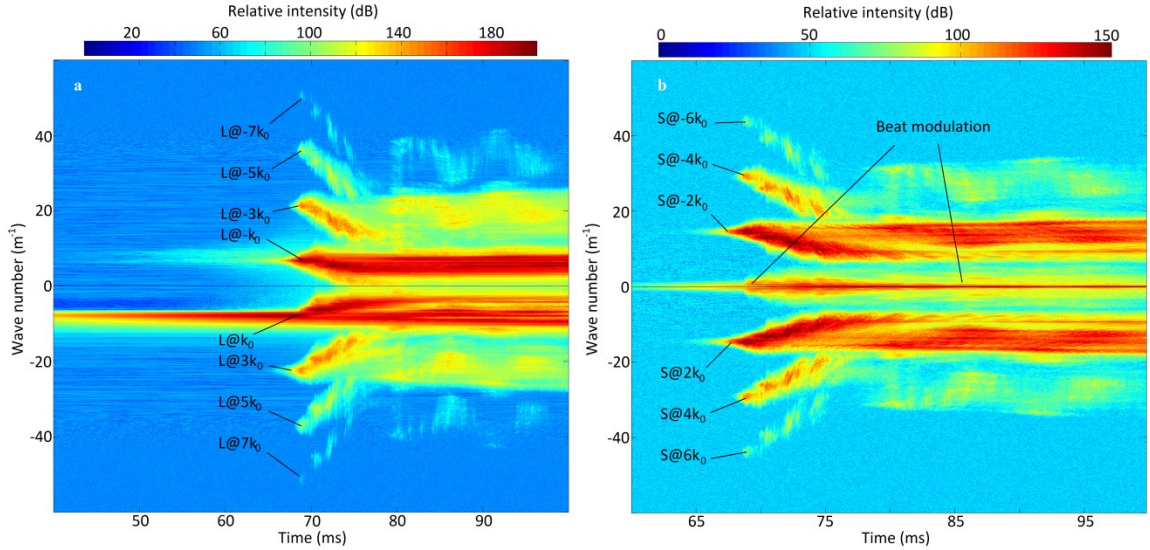


Figure 5.3. The same data as shown in Figure 5.1 but for a broader range of wave numbers and intensities to illustrate the presence of the beam modulation and three-wave coalescence products.

Figure 5.4 shows the averaged frequency behavior of the electric field and the density perturbations in Figure 5.3. In Figure 5.3 the 100 – ms simulation time is divided into 1 – ms periods. Each period is then Fourier transformed with respect to time and the results for all periods are averaged to produce Figure 5.4. In Figure 5.4a the PDI-generated Langmuir waves that closely follow the linear dispersion relation $\omega_L^2 = \omega_p^2 + 3k^2 v_e^2$ and the waves produced by the three-wave coalescence at higher wave numbers ($L@3k_0$ and $L@ - 3k_0$) are seen. Note that the features are downshifted in frequency by the plasma frequency, therefore the zero on the horizontal axis corresponds to $f_p = \frac{\omega_p}{2\pi}$.

Density perturbations are symmetric with respect to the origin (0,0) on the frequency-wave number plane; therefore, in Figure 5.4b we arbitrarily show the enhancements on

the top half plane of the frequency-wave number plane rather than on the right half plane. In this case a horizontal cut through Figure 5.4b exactly mimics the ion-line channel spectra that an ISR would measure from the underlying unstable plasma. In this figure, PDI-generated ion-acoustic waves are seen at $8 < k < 18 \text{ (m}^{-1}\text{)}$. The enhancements at higher wave numbers ($S@ - 4k_0$ and $S@ - 6k_0$) are those produced by the decay of the electric fields transferred to higher wave numbers in Figure 5.4a. At the highest wave numbers the thermal ion acoustic waves are seen that follow the linear dispersion relation $\omega^2 = C_s^2 k^2$. Finally, the enhancements at small wave numbers ($k < 8 \text{ (m}^{-1}\text{)}$) are the density perturbations produced by the beat modulations between Langmuir waves. It can be shown that such enhancements follow the dispersion relation $\omega \approx k(3 \frac{3v_e^2}{v_b})$. In both panels of Figure 5.4 the horizontal spread of energy from the most intense features are artifacts due to the chosen scale for the plot in order to simultaneously capture features with different levels of intensity.

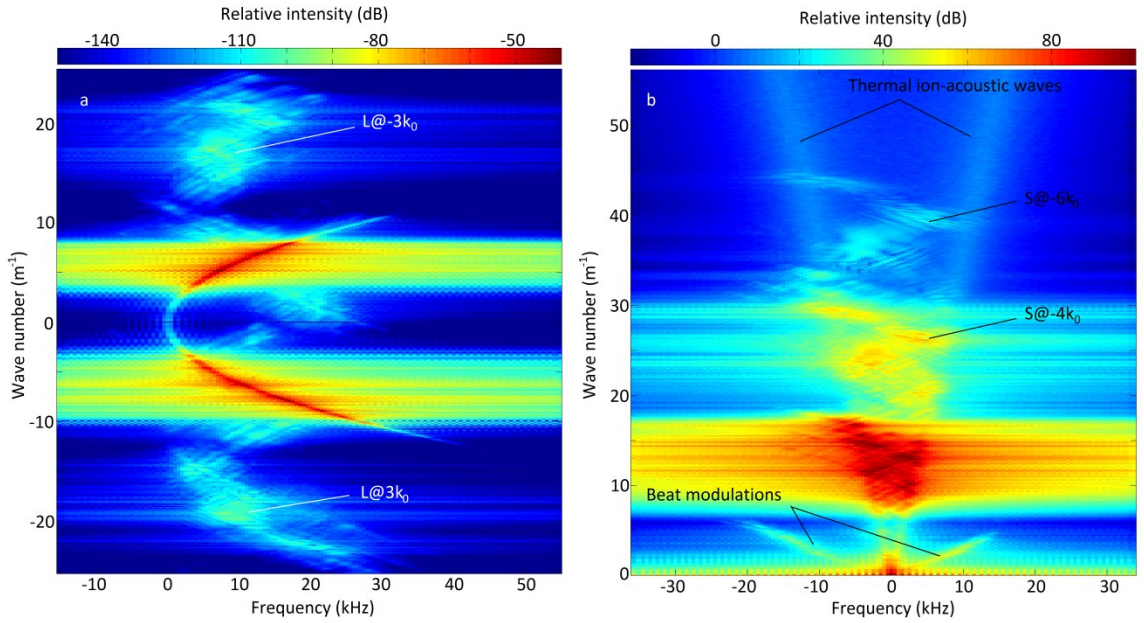


Figure 5.4. Averaged frequency behavior of the electric field and density perturbations in Figure 5.3. Products waves of the PDI, beam modulations, and the three-wave coalescence are observed.

In Figure 5.1 the cascade of parametric decays continues until the total electrostatic energy loss, due to Landau damping, equals the energy transfer from the beam to the system. At this point a quasi-steady state is reached. Providing more energy into the system by increasing the beam number density, therefore, increases the number of cascades and eventually energy may reach to the condensate ($k \sim 0$) where the PDI is prohibited and waves are subject to the modulational instabilities. This scenario has been often mentioned in the literature as one route to caviton formation and wave collapse. Note that transfer of energy to the condensate can also be facilitated by increasing the

energy of the beam which, according to the resonance condition $V_b \approx \frac{\omega}{k}$, results in the injection of energy at smaller wave numbers and thus closer to the condensate.

2. Simulation Two: $\frac{n_b}{n_0} = 60 \times 10^{-7}$ and $E_b = 125 \text{ eV}$

Figures 5.5 and 5.6 show the results of a simulation for beam parameters $\frac{n_b}{n_0} = 60 \times 10^{-7}$ and $E_b = 125 \text{ eV}$ (the beam electron number density has been increased by a factor of two compared to the simulation shown in Figures 5.1–5.4). It is seen that following the first electrostatic decay at $t \approx 32 \text{ (ms)}$ energy quickly transfers to the condensate which in real space is characterized by formation of stationary density cavities. The density cavities correspond to regions of higher refractive index and thus are ideal for trapping Langmuir energy in the form of standing waves. In Figure 5.5a a range of k components of the turbulence fall into the Modulational, subsonic Modulational, and supersonic Modulational instability regimes. However, no signs of such instabilities rise above the background turbulence. It is therefore hard to determine whether any type of Modulational Instability is in fact operating.

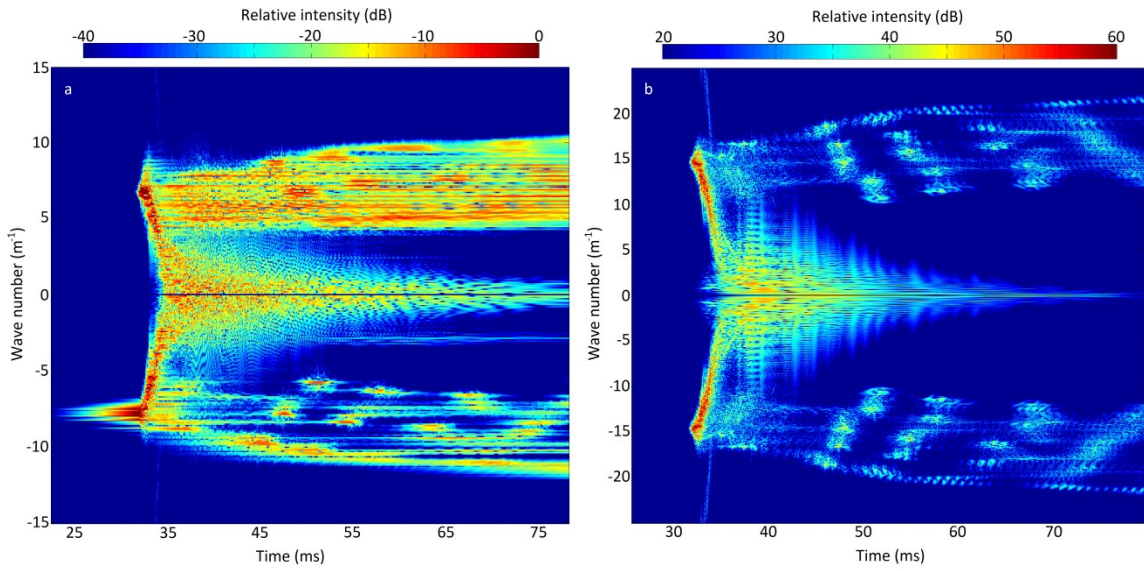


Figure 5.5. Similar to Figure 5.1, the left and right panels show the evolution of the electric field and the ion density perturbations, respectively, as a function of time and wave number for the beam parameters of $\frac{n_b}{n_0} = 60 \times 10^{-7}$ and $E_b = 125 \text{ eV}$ which has been applied at time $t = 0 \text{ ms}$.

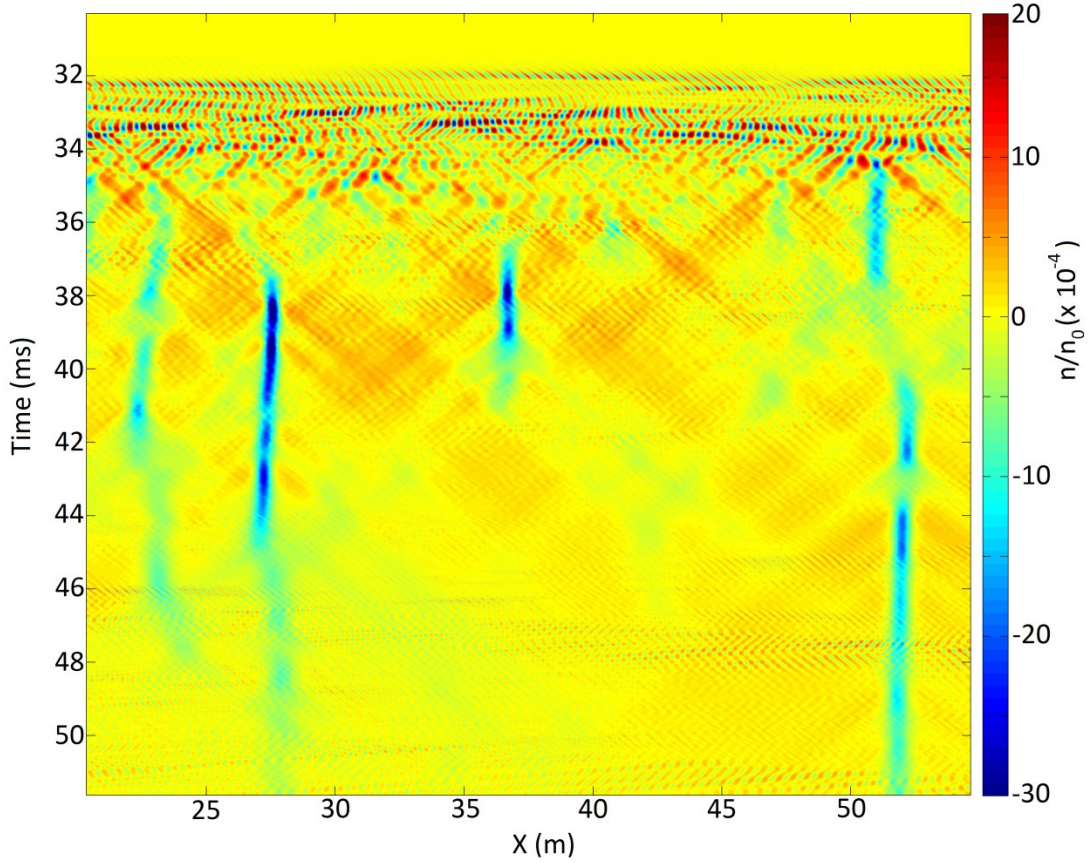


Figure 5.6. Normalized density fluctuations of Figure 5.5 in real space as a function of time: showing the formation of stationary density cavities following the transfer of energy to the condensate.

3. Simulation Three: $\frac{n_b}{n_0} = 150 \times 10^{-7}$ and $E_b = 500 \text{ eV}$

We next further increase the input energy to the system. Figure 5.7 shows the evolution of the turbulence in k space for electron beam parameters $\frac{n_b}{n_0} = 150 \times 10^{-7}$ and $E_b = 500 \text{ eV}$. The first electrostatic decay happens at time $t \approx 8 \text{ ms}$ after which energy rapidly flows to higher and lower wave numbers. After a few milliseconds the energy at

very high wave numbers dissipates and a quasi-steady state is reached which is characterized by the concentration of energy at $|k| < 20 \text{ (m}^{-1}\text{)}$ and occasional impulsive energy transfer to higher wave numbers.

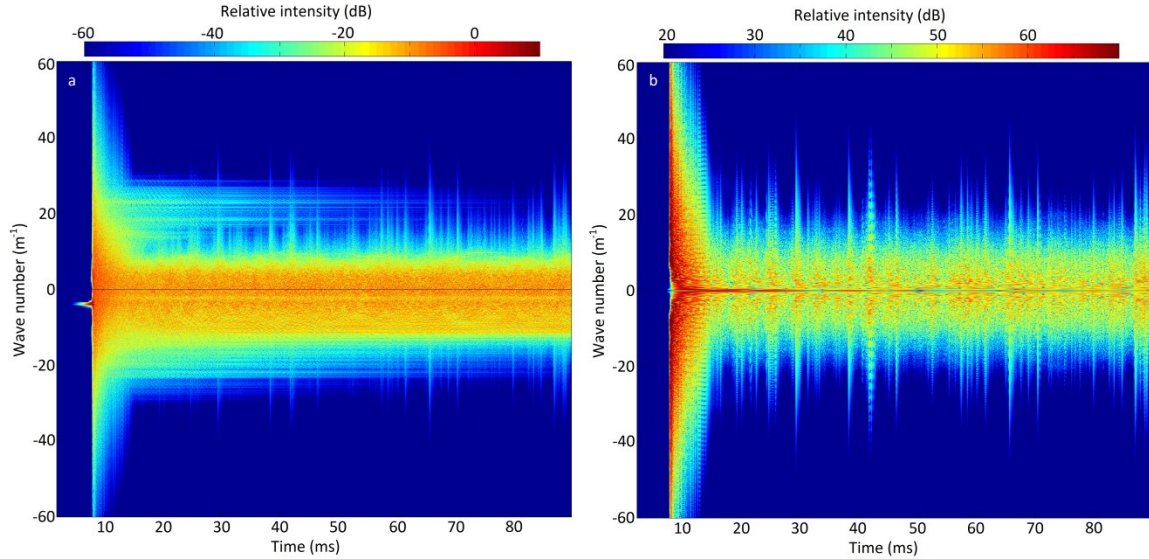


Figure 5.7. The evolution of the turbulence in k space for electron beam parameters $\frac{n_b}{n_0} = 150 \times 10^{-7}$ and $E_b = 500 \text{ eV}$.

In Figure 5.7 the initial stage of the turbulence ($8 < t < 9 \text{ ms}$) develops extremely fast making it difficult to observe the development of the turbulence in frequency domain. Therefore, in order to capture the frequency domain features at the initial stage of the turbulence we use a less strong electron beam (beam parameters $\frac{n_b}{n_0} = 90 \times 10^{-7}$ and $E_b = 500 \text{ eV}$) that allows a slower development. The results are shown in Figure 5.8. Our investigations suggest that the same development applies to the turbulence shown in Figure 5.7.

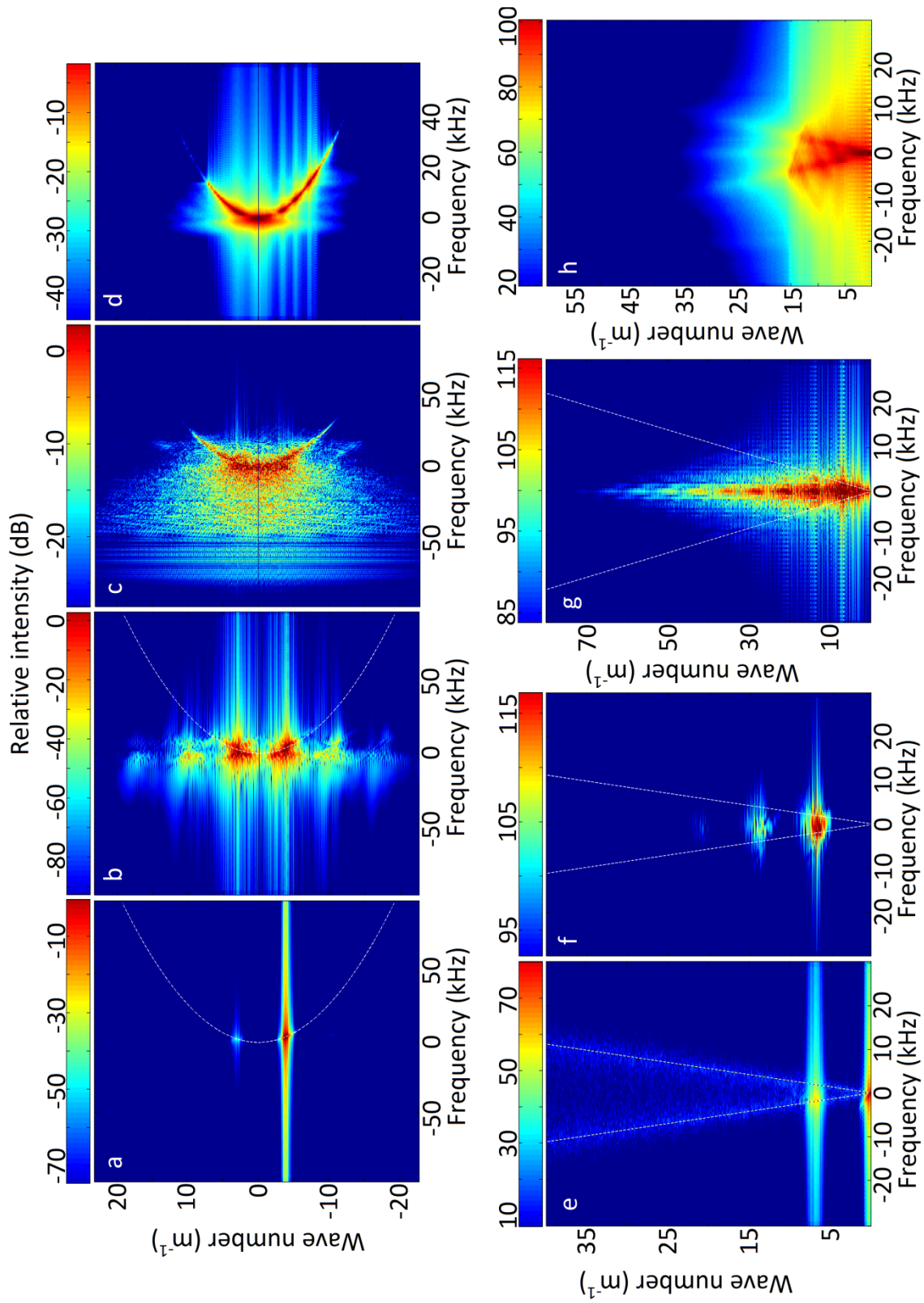


Figure 5.8. Development of the turbulence (beam parameters $\frac{n_b}{n_0} = 90 \times 10^{-7}$ and $E_b = 500 \text{ eV}$) in the wave number-frequency domain. Top and bottom panels correspond to the electric field and density perturbations, respectively, for four consecutive periods of the turbulence. Dashed white curves are the theoretical dispersion curves for the Langmuir and ion-acoustic waves.

Figures 5.8a and 5.8e correspond to the spectra for the electric field and density perturbations averaged over a $1 - ms$ period during which the initial interactions start to occur. Signatures of the initial electrostatic decay on the Langmuir and ion acoustic dispersion curves (the white dashed lines) are seen. During the next $1 - ms$ period (panels b and f) the parametrically generated Langmuir waves intensify and the products of the three-wave coalescence appear in the electric field spectrum. In the ion density spectrum the enhancements that was located on the dispersion curve, indicating the formation of ion acoustic waves, now appears at zero frequency, indicating the presence of stationary structures. During the next $1 - ms$ period (panels c and g) it is seen that the energy has covered a broad range of wave numbers and the major portion of the turbulence does not lie on the linear dispersion curves. In the electric field spectrum, in addition to the enhanced Langmuir waves, features appear below the plasma frequency indicating the existence of Langmuir fields at regions of low electron density, i.e. density cavities. In the ion density spectrum, zero frequency enhancements appear for a broad range of wave numbers, again indicating the presence of stationary structures. As will be clarified later such spectral features are signatures of caviton formation and wave

collapse. Finally, panels d and h show the spectral features averaged over a long period once the steady state has reached. Enhanced linear Langmuir and ion-acoustic waves as well as the signatures of caviton formation as seen in panels c and g, although much smoother and less intense, are present.

The time evolution of the ion density perturbations in real space is shown in Figure 5.9. Strong response appears soon after the initial electrostatic decay at time $t \approx 8 \text{ ms}$. This stage is quickly followed by formation of narrow, deep, stationary density cavities where the plasma density is up to 10% below the mean background plasma density. Inside the density cavities exist intense electric fields with amplitudes of up to 40 Vm^{-1} whose Ponderomotive force is necessary in order to maintain the density cavities. The combination of the intense electric field and the associated density cavity is called a caviton. Cavitons have been shown to go through the cycle of nucleation-collapse-dissipation-relaxation [Doolen *et al.*, 1985; Russell *et al.*, 1988; Robinson *et al.*, 1988]. This cycle can be seen in Figure 5.10 where formation of a discrete caviton is illustrated. It starts with nucleation of Langmuir packet in a density cavity that may be generated via stochastic fluctuation in the plasma. The Langmuir packet can intensify by accumulating energy from the background turbulence. Once the energy reaches to a threshold collapse initiates, i.e. the wave packets narrows and becomes more intense and the density cavity narrows and deepens as the Ponderomotive force digs the cavity. The extra plasma then propagates to the sides in the form of ion sound pulses. In Figure 5.7 collapse appears as sudden transfer of energy to high wave numbers (i.e. small spatial scales). At very small scales, tens of λ_D , a variety of linear and nonlinear processes [Robinson 1997 and

references therein] dissipate the Langmuir energy. Once a big portion of the Langmuir energy is dissipated the Ponderomotive force is no longer high enough to support the deep density cavity. The density cavity therefore relaxes, shallowing and spreading to sides. The remaining shallow density cavities have been shown to be ideal for renucleation of Langmuir packets, which allows the cycle repeat itself. This is seen in Figure 5.9 where collocated collapse events happen immediately after the relaxation stage of previous events.

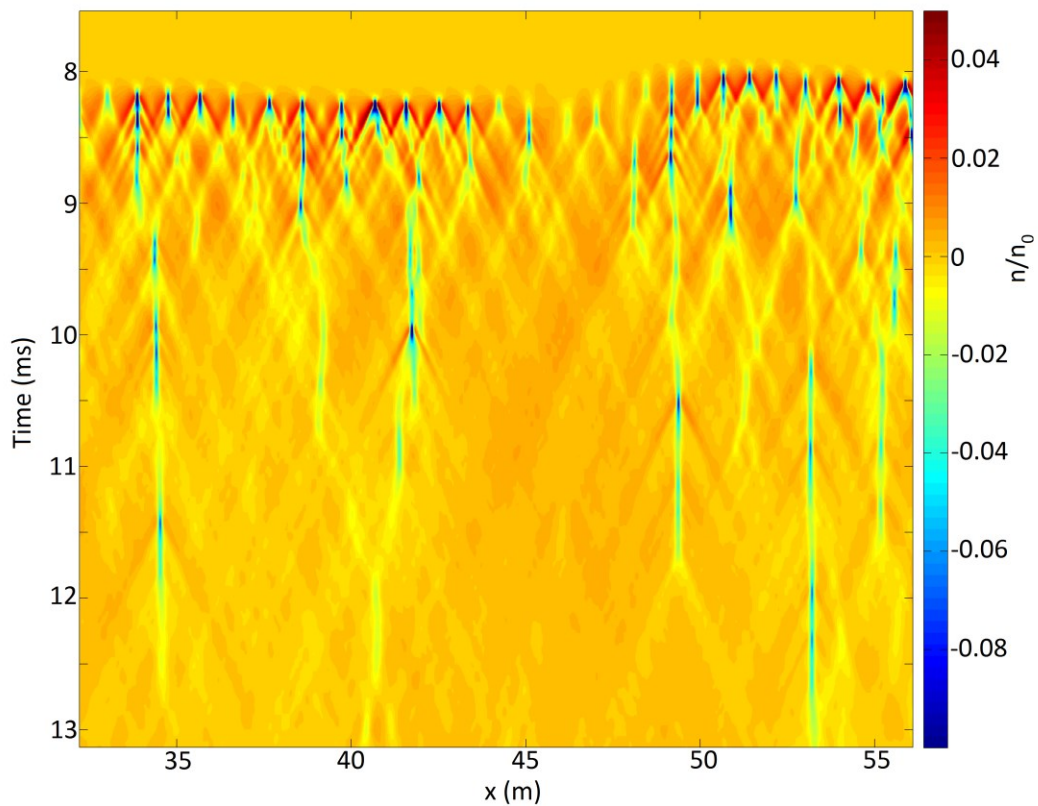


Figure 5.9. Normalized density fluctuations of Figure 5.8 in real space as a function of time.

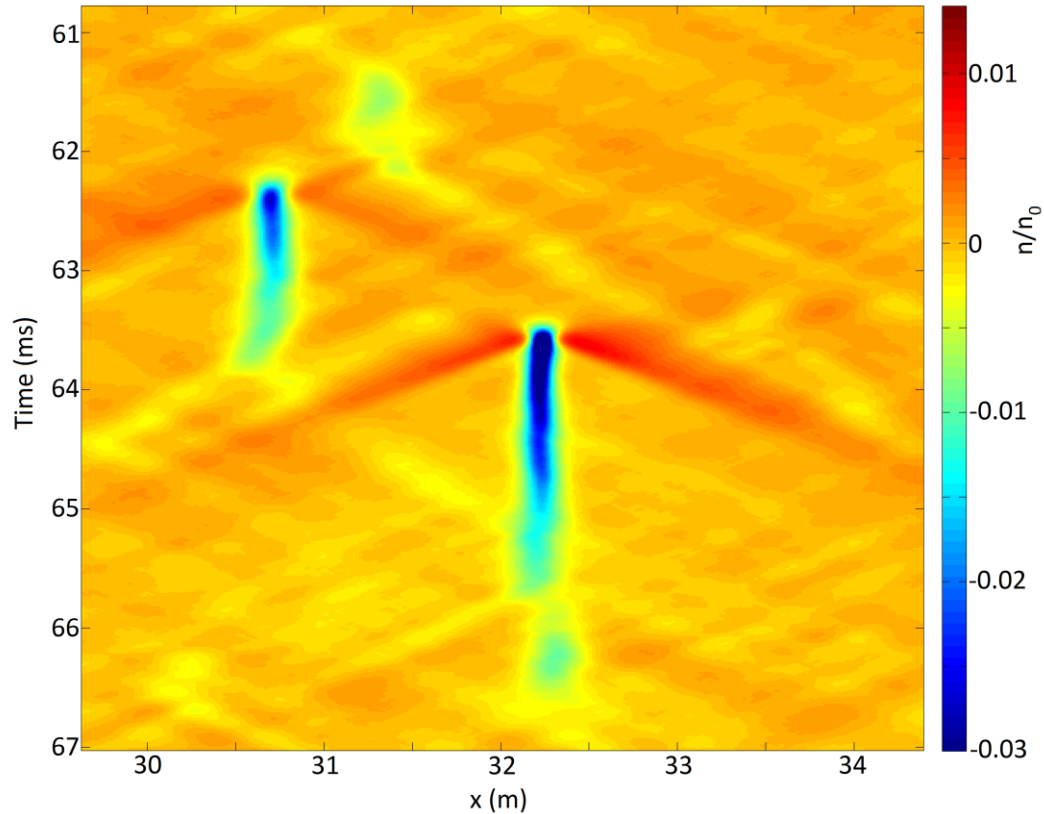


Figure 5.10. Normalized density fluctuations in real space as a function of time; showing the formation of cavitons through the cycle of nucleation-collapse-dissipation.

In Figure 5.9 it is evident that the initial stage of the turbulence, which is dominated by the formation of many cavitons, is different from the later stage once the quasi-steady state has reached. Moreover, the exact mechanism that leads to the formation of the initial cavitons needs to be clarified. In Figure 5.11 we revisit the development of the density perturbations (Figure 5.9) in more details in a logarithmic scale. At $t \approx 8.2 \text{ ms}$ density perturbations are produced as a result of the initial electrostatic decay. We verify that the density structures propagate with the sound speed and that the wavelength of the structure is what is expected from the parametric decay of the initial Langmuir waves. The

propagating ion acoustic waves are seen to gradually turn into a stationary structure. In this case every valley of the structure is an ideal location for nucleation and formation of a caviton. This development is consistent with the spectral features observed in Figures 5.8e, 5.8f, and 5.8g. After a few milliseconds the level of density perturbations in the form of ion sound pulses increases due to burnout of the cavitons. The high level of density fluctuations can then disturb the shallow density depressions before they serve as nucleation centers for new cavitons and thus the number of cavitons significantly drops after the initial stage. It is important to note that the caviton formation at early stages has dominated the turbulence and prevented any cascade of electrostatic decays or modulational instabilities.

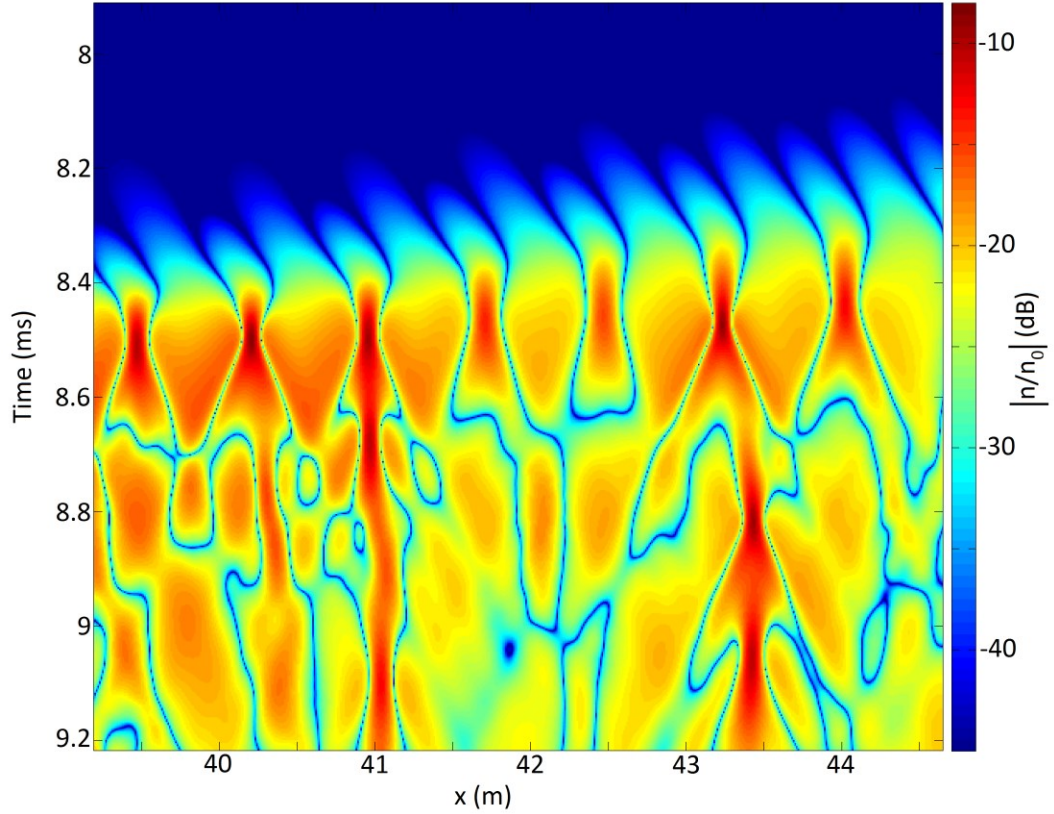


Figure 5.11. Normalized density fluctuations seen in Figure 5.9 in logarithmic scale.

Figure 5.12 shows the evolution of the electrostatic to thermal energy density (W) for the waves with the highest electrostatic energy for the simulation shown in Figure 5.7, 5.9, and 5.11. Initially the Langmuir waves with wave number $k \approx 4 \text{ (m}^{-1}\text{)}$ grow above the thermal level and at the time the ion density response appears in Figure 5.11, the Langmuir waves with the highest intensity locate on the boundary of region IV (Supersonic MI) and region V (Modified Decay Instability). Yet no signs of Supersonic MI or Modified Decay are seen. These results are similar to those presented by [Nicholson and Goldman, 1978]. They noted that once the criterion $W > (k\lambda_D)^2$ is

satisfied localized packets of waves moving at speeds less than the sound speed would directly lead to collapse and therefore for such intensities it is somewhat naive to think in terms of the linearized parametric instabilities.

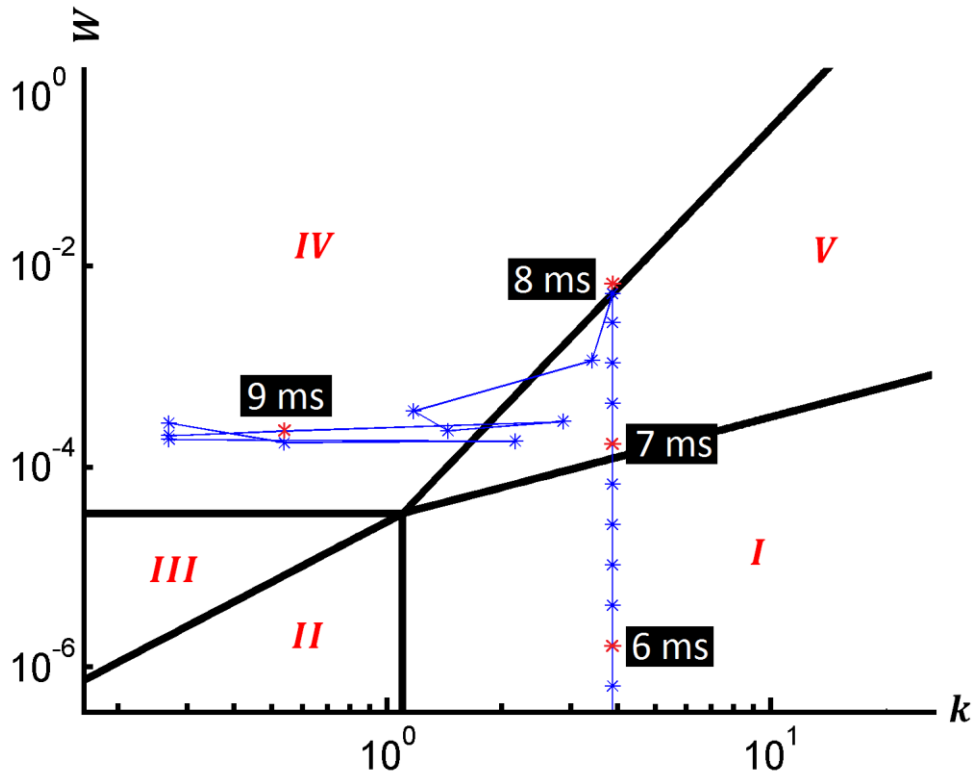


Figure 5.12. Evolution of the ratio of the electrostatic to thermal energy density (W) for the waves with the highest electrostatic energy for the simulation shown in Figures 5.7, 5.9, and 5.11.

4. Summary and Conclusion of Section 5.2.1

In summary, for the electron beams investigated in this work we observed a smooth transition in the dynamics of the turbulence from a cascade of PDI to direct collapse at

initial stages. Further increasing the input energy to the system does not significantly change the initial development of the turbulence and only increases the number of collapse events in the quasi-steady state. However, one should note that upon using much stronger electron beams the validity of the Zakharov equations would soon be under question and the beam-plasma interactions may fall under the control of other processes or higher order nonlinearities. For instance, processes such as the second harmonic generation and electron bunching in conjunction with measurements of high intensity Langmuir waves and caviton formation have been observed in the topside ionosphere [Ergun *et al.*, 1991] that cannot be described by the Zakharov equations.

Repeating the simulation for over 100 beams that explore the parameter ranges mentioned above revealed that in order for the PFISR to observe the cavitating Langmuir turbulence, an electron number density ratio of $\frac{n_b}{n_0} \geq 10^{-5}$ is typically required. For electron number density ratios much larger than the criteria mentioned above, the instability develops over relatively short time-scales. For instance, if the electron number density ratio for the simulation shown above is increased to $\frac{n_b}{n_0} = 1.5 \times 10^{-5}$ the instability fully develops in only ~ 8 milliseconds. Within such short timescales, saturation effects due to propagation of the Langmuir waves in the background density gradient is negligible, and the theory proposed to explain the localization of the echoes in thin layers by propagation effects is not applicable. We therefore conclude that if the radar echoes are produced by cavitating Langmuir turbulence, generated by electron beams streaming from higher altitudes, and localized in thin layers at the F region peak,

due to propagation effects, the electron number density of the source beams may not be much higher or lower than $n_b \approx n_0 \times 10^{-5}$.

5.2.2 Suprathermal Electrons as the Source for the ISR Echoes

The discussions in Section 5.2.1, although, provide a clear picture of the dynamics of Langmuir turbulence, do not completely address the source question for the ISR echoes. It was concluded in Section 5.2.1 that cavitating Langmuir turbulence generated by electron beams with energies of hundreds of eV may lead to simultaneous enhancements in ISRs' plasma and ion line channels. However, no definite conclusion can be made on whether such sources are in fact responsible for the radar echoes unless the details of the simulated spectra in the ion line and plasma line channels are compared to the spectral details measured by the PFISR. This is the target of the current section. Before proceeding with the comparison, however, it is important to discuss detectability of turbulence with an ISR and its relation to the input energy mechanism.

Observation of plasma waves by ISRs provides a way to accurately determine the phase velocity of the waves and therefore the energy of the electrons that may directly exchange energy with them. Assuming a background plasma density of $n = 2 \times 10^{11} \text{ (m}^3\text{)}$, this energy is ~ 5 eV for Langmuir waves that are observed by the 450-MHz Poker Flat incoherent scatter radar (with the detecting wave number, $k \sim 19 \text{ (m}^{-1}\text{)}$), and increases as the density increases. Therefore, it is sometimes argued that the free energy for the turbulence must be provided by such low energy electrons. For instance, by the

secondary electrons that are produced as a result of collisional interaction of a primary high-energy beam and the background atmosphere.

Such an input energy source is plausible, and in fact required, if the turbulence and thus the echoes are produced by the Parametric Decay Instability (PDI) at the corresponding wave numbers; however, it is not necessarily required if the turbulence is produced as a result of cavitating Langmuir turbulence and wave collapse. In the latter case, as was seen in the previous section (for instance in Figure 5.7) the input energy can be injected at lower wave numbers, via a primary electron beam with energy of hundreds of eV , and subsequently transfer to higher wave numbers and be detected by ISRs. Therefore, the simple argument mentioned above in support of the idea of secondary electrons being responsible for the observed ISR echoes needs to be further discussed. As mentioned before the goal of this section is to determine whether such soft electron beams (hundreds of eV) are responsible for the echoes. This goal will be achieved by comparing spectral details in the measured ion line channel with those seen in simulations.

1. Ion Line Spectra: ISR Measurements

Figure 5.13 shows a few examples of ion line spectra obtained from turbulence layers. Panel a (averaged over ~ 5.5 seconds) shows an enhanced double-humped spectrum where the peaks are located at the frequency of ion acoustic waves. The spectrum in panel b measured 11 seconds later shows a strong central peak at zero frequency. Signs of weaker enhancements at the frequency of ion acoustic waves are also present in this panel. If the spectrum was produced by averaging over a 16-second that includes data

shown in panels a and b, the result would look like the spectra shown in panel c and the one shown in Figure 4.4. The superposition of the two ion acoustic shoulders and the central peak would result in a flat spectrum that extends from the down-shifted shoulder to the up-shifted shoulder. This kind of flat spectrum has been previously observed by different ISRs [Ekeberg *et al.*, 2010; Mitchell and Samara, 2010; Akbari *et al.*, 2012, 2013].

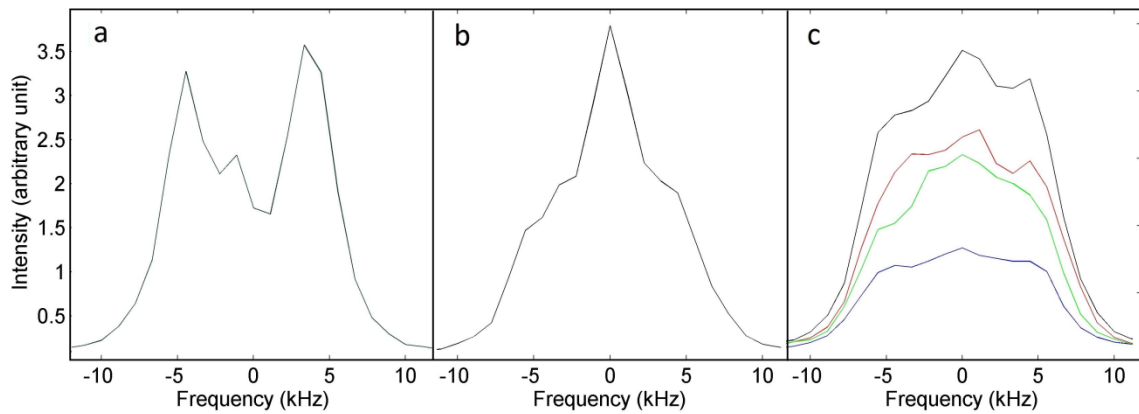


Figure 5.13. Examples of ion line spectra measured by the PFISR. Each spectrum, including those with different colors in panel c, corresponds to different times.

As was discussed in Section 5.2.1, observation of a strong central peak in the ion line spectrum is commonly attributed to the existence of stationary density cavities produced by strong Langmuir turbulence [DuBois *et al.*, 1993a, b], whereas the enhanced peaks seen in Figure 5.13a are attributed to enhanced level of ion acoustic waves that follow the linear dispersion relation. The flat spectra seen in Figure 5.13c, on the other hand, are not fully understood. The only speculation thus far is that the flat shape arises as a result of superposition of enhanced ion acoustic peaks and a strong central peak. Other

experiments by EISCAT UHF and VHF radars have measured triple-peaked spectra in which the two ion acoustic shoulders and a distinct and equally enhanced central peak are present simultaneously [Isham *et al.*, 2012; Schlatter *et al.*, 2013].

2. Ion Line Spectra: Simulations and Comparison with Measurements

Figure 5.14 shows the result of the simulation for one set of beam parameters ($\frac{n_b}{n_0} = 0.9 \times 10^{-5}$ and $E_b = 500 \text{ eV}$) in the same format as those in Section 5.2.1. The left and right panels show the evolution of the electric field (E) and the ion density perturbations (n), respectively, as a function of time and wave number. The source electron beam initially enhances Langmuir waves with wave numbers $k \sim 4 \text{ (m}^{-1}\text{)}$ that satisfy the resonant condition $v_b \approx \omega_p/k$ (where ω_p is the plasma frequency) and soon the turbulence expands in a broad range of wave numbers due to caviton formation.

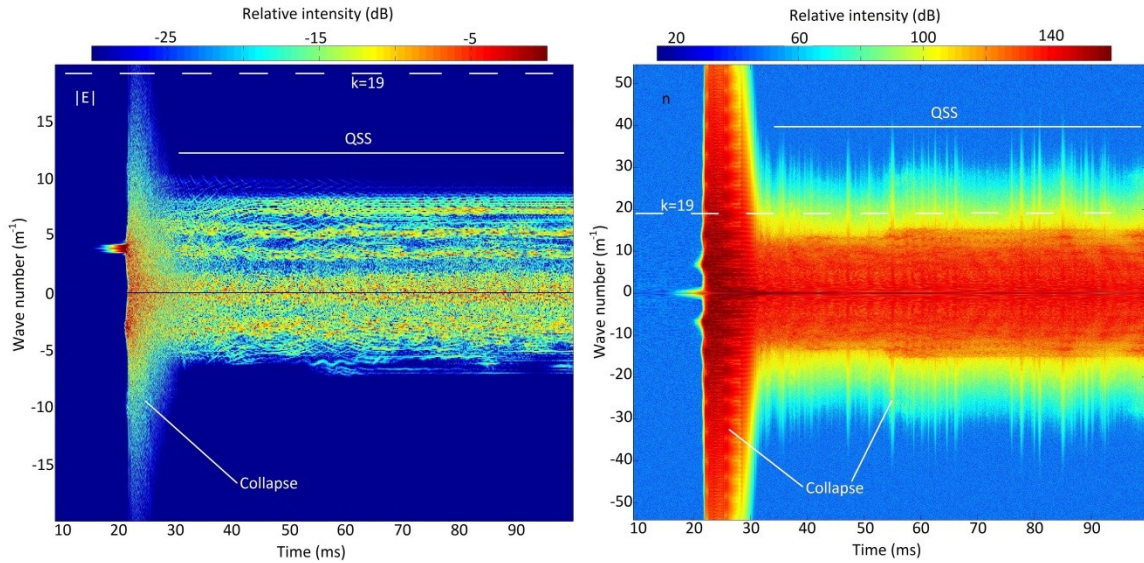


Figure 5.14. Evolutions of the electric field magnitude (left) and ion density perturbations (right) as a function of time and wave number. The electron beam has been applied at time $t = 0$ (ms). White dashed lines show the PFISR detecting wave number.

This figure presents an important point on the wave number dependence of the turbulence. It is seen that once we pass the initial stage of the turbulence at $t \sim 22 - 28$ (ms), the turbulence in quasi-steady state is highly k -dependent. In Figure 4.14b the main portion of the density perturbations exists at low wave numbers ($k < 15$ (m^{-1})). For higher wave numbers ($15 < k < 30$ (m^{-1})) the level of density fluctuations drops by orders of magnitude below the level for $k < 15$ (m^{-1}). This level of density fluctuations, however, is still orders of magnitude above the thermal level. The observed wave number dependence can be easily explained. Intense ion density perturbations at $k < 15$ (m^{-1}) are produced by a cascade of PDIs which efficiently transfers energy from the upper bound ($k = 15$ (m^{-1})) to small wave numbers ($k \approx 0$ (m^{-1})). The PDI do not

transfer any energy to higher wave numbers, however, a small portion of energy in the range $k < 15 \text{ (} m^{-1} \text{)}$ can still leak to $k > 15 \text{ (} m^{-1} \text{)}$ via two other processes, these are 1) wave collapse and 2) a two-step process by which first, high-frequency waves are produced by scattering of Langmuir waves off ions and second, the produced high-frequency waves decay to produce ion density perturbation at $k > 15 \text{ (} m^{-1} \text{)}$. Both these processes are secondary relative to the PDI and thus the generated waves in the range $15 < k < 30 \text{ (} m^{-1} \text{)}$ are orders of magnitude weaker than those in the range $k < 15 \text{ (} m^{-1} \text{)}$.

The point of the discussion above is that if the turbulence is generated by injection of energy at low wave numbers and is brought to higher wave numbers by wave collapse or scattering off ions, upon being detected by various ISRs such as the EISCAT VHF (detecting wave number $k \sim 11 \text{ (} m^{-1} \text{)}$), the PFISR (detecting wave number $k \sim 19 \text{ (} m^{-1} \text{)}$), and the EISCAT UHF (detecting wave number $k \sim 38 \text{ (} m^{-1} \text{)}$) would produce backscatters that are orders of magnitude different in intensity in the three radars. This is in clear disagreement with the observations, where the intensity of the echoes in the three ISRs are similarly 15–20 dB above the thermal level [*Isham et al.*, 2012; *Akbari et al.*, 2012; *Schlatter et al.*, 2013]. We therefore conclude that the injection of energy to the system should happen, at least in part, at high wave numbers. This in turn requires low energy electrons of the order $5 - 20 \text{ eV}$.

Further discrepancy between experimental observations and the hypothesis that the beam energy injection happens at small wave numbers (long wavelengths) appears in spectral

features of density perturbations. It is seen in our simulations that the behavior of density cavities after the dissipation stage and the level of ion acoustic density pulses emitted from them strongly depend on the damping rate for density fluctuations which, in turn, depends on the electron to ion temperature ratio. For the temperature ratio of $\frac{T_e}{T_i} = 3$ (plausible for the auroral F region) it is seen that the density cavities slowly relax in place rather than emitting strong sound pulses. The stationary density cavities then dominantly give rise to a strong central peak at zero frequency in ISR's ion line channel with no strong ion acoustic sidebands. This picture changes if we decrease the ion acoustic damping rate by using a higher temperature ratio. In this case: first, following the dissipation stage unsupported density cavities break into ion sound pulses and, second, the reduced damping enables the ion sound pulses to continue to propagate for a longer time in the system giving rise to resonant ion acoustic shoulders.

The dominance of a zero-frequency central peak in the ion line spectra is shown in Figure 5.15. Figure 5.15a shows the averaged frequency behavior of density perturbations in Figure 5.14b once the system has reached the quasi-steady state. The enhancements produced by Langmuir decay follow the linear dispersion relation, $\omega = C_s|k|$ where ω , C_s , and k are wave frequency, sound speed, and wave number. A very weak central peak at zero frequency is also observed for $k < 20$ (m^{-1}) that is the signature of the sporadic collapse events seen in Figure 5.14b. No density perturbations above thermal level is seen above $k = 35$ (m^{-1}). Increasing the input energy to the system, by increasing the beam number density from $\frac{n_b}{n_0} = 0.9 \times 10^{-5}$ to $\frac{n_b}{n_0} = 1.5 \times 10^{-5}$, results in an increase in the

number of collapse events and consequently a pronounced central peak appears in the frequency spectrum. This is shown in Figure 5.15b where the central peak dominates the shape of the spectrum at higher wave numbers. In Figure 5.15c we plot the ion line spectra that would be seen if the turbulence was detected by the EISCAT VHF, PFISR, and the EISCAT UHF radars. These are horizontal cuts through Figure 5.15b since ISRs observe wave activities at single wave numbers.

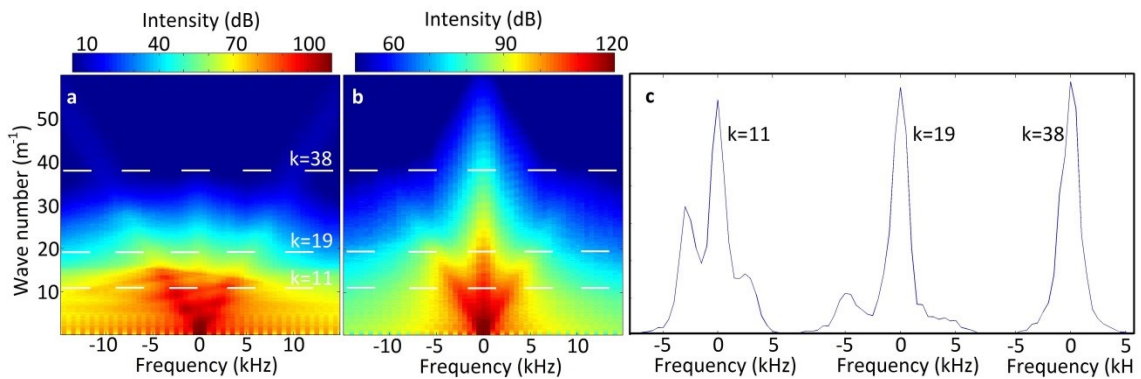


Figure 5.15. Panel a shows the averaged frequency behavior of density perturbations in Figure 5.14b once the quasi-steady state has been reached. Panel b is similar to panel a, but for a simulation run with a higher input energy to the system. Panel c, shows horizontal cuts through panel b at wave numbers 11, 19, and 38 (m^{-1}) (shown by white dashed lines in panels a and b), modeling the spectra that would be obtained if the turbulence was detected by the EISCAT VHF, PFISR, and the EISCAT UHF radars, respectively.

The spectrum at $k = 38$ (m^{-1}) is dominated by a single central peak and no resonant ion acoustic peaks similar to those seen by the EISCAT UHF radar [Schlatter et al., 2013]

are seen. We therefore propose the possibility that the observed enhanced ion acoustic peaks in the EISCAT UHF radar measurements are produced by the parametric decay instability at the corresponding wave numbers.

3. Summary and Conclusion of Section 5.2.2

Based on the results discussed above it is concluded that a turbulence developed by injection of energy to small wave numbers and transferred to higher wave numbers by caviton collapse or scattering off ions, upon being detected by ISRs with different detecting wave numbers, would result in radar backscatter echoes that are orders of magnitude different in intensity. This is in clear disagreement with the experimental observations, suggesting that at least a portion of the energy is provided at higher wave numbers by a locally generated suprathermal electron population in the 5-20 eV range.

Moreover, at high wave numbers such as $k = 38 \text{ (m}^{-1}\text{)}$, i.e. detecting wave number of the EISCAT UHF radar, caviton collapse would give rise to a dominant zero-frequency peak in the ion line channel which does not match the experimental data. Observations of enhanced ion acoustic peaks, therefore, suggest that the PDI operates at the observations wave numbers. This, in turn, requires the existence of lower energy electrons ($E_b < 20 \text{ eV}$) at the observations altitudes and, since such electrons cannot propagate from higher altitudes, this population should be produced locally.

Secondary electrons produced as a result of collisional interaction of primary energetic electrons with neutral atmosphere have been previously suggested to provide free energy

for some E region Langmuir wave enhancements [*Valladares et al.*, 1988; *Kirkwood et al.*, 1995] as well as two E region plasma instabilities involving modes that propagate close to perpendicular to the magnetic field [*Basu et al.*, 1982; *Jasperse et al.*, 2013]. However, given their pitch-angle distribution, it is yet to be determined whether such secondary electrons would develop the intense unstable feature that is required to initiate the PDI, namely a strong positive slope in their 1-dimensional distribution function.

Chapter 6

Summary, Conclusions, and Future Directions

6.1 Summary and Conclusions

In this chapter a summary of the main results obtained in this thesis is presented. Possible directions that I envision as extension of this work are also discussed.

Through experimental efforts with the 449-MHz Poker Flat Incoherent Scatter Radar (PFISR) a new type of echo was discovered that showed unusual features in both the ion line and plasma line measurements. These were (1) a greatly enhanced flat ion acoustic spectrum and (2) presence of two peaks in the plasma line spectra. We identified the echoes as signatures of beam-generated cavitating Langmuir turbulence. The flat ion acoustic spectrum is believed to represent a zero-frequency peak, caused by Bragg scattering from non-propagating density fluctuations, and the two peaks in the plasma line spectra are associated with (1) caviton formation and (2) linear Langmuir waves. The observations attracted attention to the topic of Langmuir turbulence in the auroral ionosphere and ever since many examples of the echoes have been detected by various ISRs.

Following the detection of the first echo I focused my attention on conducting more ISR experimental to resolve the unusual characteristics of the echoes. Using high-range resolution measurements we showed that the turbulence is sometimes manifested as two concurrent layers separated by about 50 km. The turbulence layers appear at regions of

zero electron density gradient, indicating the importance of propagation effects in dynamics of beam-plasma interactions in the ionosphere. It was argued that in the presence of density gradient such effects play an important role in limiting the waves' amplitude. Furthermore, the radar measurements of the electrostatic waves were found to be correlated in space and time with one type of natural auroral electromagnetic emissions, i.e. "MF burst", supporting the theory that the emission is produced by linear conversion of Langmuir waves produced by soft electron precipitation (~few hundred eV) on the topside F region. The results suggested that the observed Langmuir turbulence and MF burst are both manifestations of the same process.

Next, I focused my efforts on simulations. The goal was to identify the source of free energy underlying the turbulence. I used 1-dimensional Zakharov simulations to investigate beam-generated Langmuir turbulence in the auroral ionosphere. We found that simultaneous enhancements in the ion and plasma line channels of the PFISR can be produced by strong Langmuir turbulence and caviton collapse generated by relatively strong ($n_b \sim n_0 \times 10^{-5}$) soft electron beams ($100 \text{ eV} \leq E_b \leq 1 \text{ keV}$). However, it was shown that turbulence developed by injection of energy to small wave numbers and transferred to higher wave numbers by caviton collapse or scattering off ions would produce echoes that are in clear disagreement with the experimental observations. Based on the results we, therefore, proposed that, at least, a portion of the energy is provided at higher wave numbers by a locally generated suprathermal electron population in the 5-20 eV range. It is not clear what process might be responsible for energization of the electron.

Through simulations we also extensively investigated the dynamics of Langmuir turbulence for a wide range of input energies. While for smaller input energies we observed the well know Parametric Decay Instability and Langmuir cascade, for higher energies or lower wave numbers where Supersonic MI or Modified Decay were expected, these interactions were absent and instead direct collapse was initiated from ion density perturbations at early stages of the turbulence. These results are similar to those presented by [Nicholson and Goldman, 1978] and suggest that once the criterion $W > (k\lambda_D)^2$ is satisfied localized packets of waves moving at speeds less than the sound speed would directly lead to collapse and therefore for such intensities it is somewhat naive to think in terms of the linearized parametric instabilities.

6.2 Future Directions

Observations suggest that plasma waves and wave-particle interactions are widely present during intense auroral activities. Their signatures manifest in a variety of large scale auroral. Yet, the role of plasma waves in the large scale energy balance in the magnetosphere-ionosphere system has attracted little quantitative studies. For instance, deposition of magnetospheric energy into the ionosphere is largely considered in the form of collisional interactions in the lower ionosphere, and a simple question that ‘what fraction of the kinetic energy of the precipitating electrons would be dissipated through plasma waves at higher altitudes where collisional interactions are not important?’ has not been addressed in depth. ISR and in-situ measurement suggest that Langmuir waves are commonly enhanced in the auroral ionosphere. A possible future direction for this

work is, therefore, to investigate the role such waves in the magnetospheric energy deposition in the ionosphere.

Based on the quasi-linear diffusion theory upon presence of unstable electron distribution, namely presence of positive slope in the one-dimensional distribution function, beam-plasma interactions continue until plasma waves grow to high enough intensity to react back on the distribution function and flatten the positive slope. At this point electrons have lost up to one third of their kinetic energy to the waves. In the auroral ionosphere, high altitude rocket observations [Ergun *et al.*, 1991] have revealed that during periods of intense electron precipitation large amplitude Langmuir waves are commonly generated above 600 (km). Yet the measured auroral electron distributions are rarely unstable to such waves at altitudes of 200~300 km [McFadden *et al.*, 1986] since the distribution has already flattened. This transition needs to be investigated in details. Note that modifications on the distribution function also affect the collisional interaction of the electrons with the lower ionosphere through altering the penetration depth. Although, the predictions of a simple quasi-linear diffusion theory may be overestimated due to neglecting nonlinear wave-wave processes [Matthews *et al.*, 1976] and the pitch angle distribution of electrons, the combination of the experimental and theoretical works illustrates the need for detailed quantitative studies on effects of plasma waves on energy balance in the magnetosphere-ionosphere system.

An inseparable aspect of such studies is detailed investigation of micro-scale processes and instabilities. Sparse reports of rocket and satellite measurements have revealed large-

amplitude (up to 500 mV/m) Langmuir waves in the auroral ionosphere. Such intense waves are subject to nonlinear effects, such as second harmonic generation, amplitude modulations, and wave collapse, and are responsible for processes such as electron bunching and generation of non-thermal features in electron distribution function [*Ergun et al.*, 1991; *Kaufmann*, 1980; *Papadopoulos and Coffey*, 1974; *Boehm et al.*, 1984; *Gough and Urban*, 1983]. Observations of medium frequency electromagnetic waves, their connection to Langmuir waves, and the corresponding mode conversion is currently being investigated [*Broughton and LaBelle*, 2014] and fall in the same category as the mentioned processes. Such observations, however, have raised as many questions as answers they have provided. For instance, observations of beam generated Langmuir waves at lower ionosphere raise questions on the nature of wave-particle interactions at higher altitudes where yet stronger interactions are expected due to drop in the background plasma density. Such interactions must saturate quasi-linear diffusion in order to let the precipitating electrons maintain the unstable distribution as they propagate to lower altitudes.

The point is that the picture that currently arises from sparse observational reports is far from a comprehensive picture that summarizes beam-plasma interactions in magnetosphere and ionosphere. A complete picture, however, can be produced by extensive observationally-inspired simulations, for instance three-dimensional Particle-in-Cell (PIC) or electromagnetic Zakharov simulations that incorporate quasi-linear diffusion effects.

References

- Akbari, H., J. L. Semeter, H. Dahlgren, M. Diaz, M. Zettergren, A. Strømme, M. J. Nicolls, and C. Heinselman (2012), Anomalous ISR echoes preceding auroral breakup: Evidence for strong Langmuir turbulence, *Geophysical Research Letters*, 39, L03102, doi:10.1029/2011GL050288.
- Akbari, H., J. L. Semeter, M. J. Nicolls, M. Broughton, and J. W. LaBelle (2013), Localization of auroral Langmuir turbulence in thin layers, *Journal of Geophysical Research. Space Physics*, 118, 3576–3583, doi:10.1002/jgra.50314.
- Akbari, H., and J. L. Semeter (2014), Aspect angle dependence of naturally enhanced ion acoustic lines, *Journal of Geophysical Research. Space Physics*, 119, 5909–5917, doi:10.1002/2014JA019835.
- Akbari, H., J. L. Semeter, M. A. Hirsch, P. Guio, and M. J. Nicolls (2015a), Evidence for generation of unstable suprathermal electron population in the auroral F region, *Geophysical Research Letters*, 42, 185–192, doi:10.1002/2014GL062598.
- Akbari, H., J. L. Semeter, P. Guio, M. A. Hirsch (2015b), Ionospheric electron beams and Langmuir turbulence (submitted).
- André, M. (1997), Wave and wave-particle interactions in the auroral region, *Journal of Atmospheric and Solar-Terrestrial Physics*, 5914, 1687–1712, doi:10.1016/S1364-6826(96)00173-3.
- Angelopoulos, V., et al. (2008), First results from the THEMIS mission, *Space Science Reviews*, 141, 453–476, doi:10.1007/s11214-008-9378-4.
- Arnoldy, R. L., K. A. Lynch, J. B. Austin, and P. M. Kintner (1999), Energy and pitch angle-dispersed auroral electrons suggesting a time-variable, inverted-V potential structure, *Journal of Geophysical Research*, 104(A10), 22,613–22,621, doi:10.1029/1999JA900219.
- Bahcivan, H., and R. Cosgrove (2008), Enhanced ion acoustic lines due to strong ion cyclotron wave fields, *Annales Geophysicae*, 26, 2081–2095
- Bale, S. D. (1999), Observation of topside ionospheric MF/HF radio emission from space, *Geophysical Research Letters*, 26(6), 667–670.

Basu, B., T. Chang, and J. R. Jasperse (1982), Electrostatic plasma instabilities in the daytime lower ionosphere, *Geophysical Research Letters*, 9, 68–71, doi:10.1029/GL009i001p00068.

Bering, E. A. (1984), The plasma wave environment of an auroral arc: Electrostatic ion cyclotron waves in the diffuse aurora, *Journal of Geophysical Research*, 89(A3), 1635–1649, doi:10.1029/JA089iA03p01635.

Bernstein, I. B., *Phys. Rev.* 109, 10 (1958).

Birkmayer, W., T. Hagfors, and W. Kofman (1986), Small-scale plasmadensity depletions in Arecibo high-frequency modification experiments, *Physical Review Letters*, 57, 1008–1011.

Blixt, E. M., T. Grydeland, N. Ivchenko, T. Hagfors, C. La Hoz, B. S. Lanchester, U. P. Løvhaug, and T. S. Trondsen (2005), Dynamic rayed aurora and enhanced ionacoustic radar echoes, *Annales Geophysicae*, 23, 3–11.

Bunch, N. L., J. LaBelle, A. T. Weatherwax, and J. M. Hughes (2008), Auroral medium frequency burst radio emission associated with the 23 March 2007 THEMIS study substorm, *Journal of Geophysical Research*, 113, A00C08, doi:10.1029/2008JA013503, [printed 115(A1), 2010].

Bunch, N. L., J. LaBelle, P. Yoon, and A. T. Weatherwax (2011), Theoretical constraints on the generation mechanism of auroral medium frequency burst radio emissions, *Journal of Geophysical Research*, 116, A01315, doi:10.1029/2010JA015951.

Cabrit, B., H. Opgenoorth, and W. Kofman (1996), Comparison between EISCAT UHF and VHF backscattering cross section, *Journal of Geophysical Research*, 101(A2), 2369–2376, doi:10.1029/95JA02175.

Carlson, H. C., W. E. Gordon, and R. L. Showen (1972), High frequency induced enhancements of the incoherent scatter spectrum at Arecibo, *Journal of Geophysical Research*, 77(7), 1242–1250, doi:10.1029/JA077i007p01242.

Chen, F. (1984). *Introduction to Plasma Physics and Controlled Fusion*. Plenum Publishing Corporation.

Cheung, P. Y., A. Y. Wong, T. Tanikawa, J. Sanford, D. F. DuBois, H. A. Rose, and D. Russel (1989), Short-time-scale evidence for strong Langmuir turbulence during HF

heating of the ionosphere, *Physical Review Letters*, 62, 2676–2679, doi:10.1103/PhysRevLett.62.2676.

Cheung, P. Y., D. F. DuBois, T. Fukuchi, K. Kawan, H. A. Rose, D. Russell, T. Tanikawa, and A. Y. Wong (1992), Investigation of strong Langmuir turbulence in ionospheric modification, *Journal of Geophysical Research*, 97(A7), 10,575–10,600, doi:10.1029/92JA00645.

Collis, P. N., I. Häggström, K. Kaila, and M. T. Rietveld (1991), EISCAT radar observations of enhanced incoherent scatter spectra: Their relation to red aurora and field-aligned currents, *Geophysical Research Letters*, 18(6), 1031–1034, doi:10.1029/91GL00848.

Dahlgren, H., J. L. Semeter, R. A. Marshall, and M. Zettergren (2013), The optical manifestation of dispersive field-aligned bursts in auroral breakup arcs, *Journal of Geophysical Research. Space Physics*, 118, 4572–4582, doi:10.1002/jgra.50415.

Diaz, M. A., J. L. Semeter, M. Oppenheim, and M. Zettergren (2008), Particle-in-cell simulation of the incoherent scatter radar spectrum, *Radio Science*, 43, RS1007, doi:10.1029/2007RS003722.

Diaz, M. A., J. L. Semeter, M. Oppenheim, and M. Zettergren (2010), Analysis of beam plasma instability effects on incoherent scatter spectra, *Annales Geophysicae*, 28, 2169–2175, doi:10.5194/angeo-28-2169-2010.

Diaz, M. A., M. Oppenheim, J. L. Semeter, and M. Zettergren (2011), Particle-in-cell simulation of incoherent scatter radar spectral distortions related to beam-plasma interactions in the auroral ionosphere, *Journal of Geophysical Research*, 116, A00K10, doi:10.1029/2010JA016096.

Doolen, G. D., D. F. DuBois, and H. A. Rose (1985), Nucleation of solitons in strong Langmuir turbulence, *Physical Review Letters*, 54, 804–807, doi:10.1103/PhysRevLett.54.804.

Dougherty, J.P., and D. T. Farley (1960), A theory of incoherent scattering of radio waves by a plasma, *Proceedings of the Royal Society of London. Series A, Mathematical and Physical Sciences*, A359, 79-99.

DuBois, D. F., A. R. Harvey, and D. Russell (1988), Power spectra of fluctuations in strong Langmuir turbulence, *Physical Review Letters*, 61, 2209–2212, doi:10.1103/PhysRevLett.61.2209.

DuBois, D., H. Rose, and D. Russell (1990), Excitation of strong Langmuir turbulence in plasmas near critical density: Application to HF heating of the ionosphere, *Journal of Geophysical Research*, 95(A12), 21,221–21,272, doi:10.1029/JA095iA12p21221.

DuBois, D. F., H. A. Rose, and D. Russell (1991), Coexistence of parametric decay cascades and caviton collapse at subcritical densities, *Physical Review Letters*, 66, 1970–1973, doi:10.1103/PhysRevLett.66.1970.

DuBois, D. F., A. Hansen, H. A. Rose, and D. Russell (1993), Excitation of strong Langmuir turbulence in the ionosphere: Comparison of theory and observations, *Physics of Fluids. B, Plasma Physics*, 5(7), 2616–2622, doi:10.1063/1.860699.

DuBois, D. F., A. Hanssen, H. A. Rose, and D. Russell (1993a), Space and time distribution of HF excited Langmuir turbulence in the ionosphere: Comparison of theory and experiment, *Journal of Geophysical Research*, 98(A10), 17,543–17,567, doi:10.1029/93JA01469.

DuBois, D. F., A. Hansen, H. A. Rose, and D. Russell (1993b), Excitation of strong Langmuir turbulence in the ionosphere: Comparison of theory and observations, *Physics of Fluids. B, Plasma Physics*, 5(7), 2616–2622, doi:10.1063/1.860699.

Dysthe, K. B., E. Mjølhus, H. L. Pecseli, and L. Stenflo, Langmuir solitons in magnetized plasmas, *Plasma Physics*, 20, 1087, 1978.

Ekeberg, J., G. Wannberg, L. Eliasson, and I. Häggström (2012), Soliton-induced spectrally uniform ion line power enhancements at the ionospheric F region peak, *Earth, Planets, and Space*, 64, 605–611, doi:10.5047/eps.2012.02.005.

Ergun, R. E., C. W. Carlson, J. P. McFadden, J. H. Clemmons, and M. H. Boehm (1991), Langmuir wave growth and electron bunching: Results from a wave-particle correlator, *Journal of Geophysical Research*, 96, 225.

Evans, J. V. (1969), Theory and practice of ionosphere study by Thomson scatter radar, *Proceedings of the IEEE*, 57(4), 496–530, doi:10.1109/PROC.1969.7005.

Fang, X., C. E. Randall, D. Lummerzheim, S. C. Solomon, M. J. Mills, D. R. Marsh, C. H. Jackman, W. Wang, and G. Lu (2008), Electron impact ionization: A new parameterization for 100 eV to 1 MeV electrons, *Journal of Geophysical Research*, 113, A09311, doi:10.1029/2008JA013384.

- Farley, D. T., J. P. Dougherty, and D. W. Barron, Proceedings of the Royal Society of London. Series A, Mathematical and Physical Sciences 263, 238 (1961).
- Farley, D. T. (1969), Incoherent scatter correlation function measurements, *Radio Science*, 4, 935–953.
- Farley, D. T., Multiple pulse incoherent scatter correlation function measurements, *Radio Science*, 7, 661-666, 1972.
- Farley, D. (1996). Incoherent scatter radar probing. *Modern Ionospheric Science*, Eds. H. Kohl, R. Rüster, K. Schlegel, Copernicus Society, Katlenburg-Lindau, Germany.
- Fejer, J. A. (1960), Radio-wave scattering by an ionized gas in thermal equilibrium, *Journal of Geophysical Research*, 65, 2635-2636.
- Fejer, J. A., *Canadian Journal of Physics*, 39, 716 (1961).
- Fejer, J. A., M. P. Sulzer, and F. T. Djuth (1991), Height dependence of the observed spectrum of radar backscatter from HF-induced ionospheric Langmuir turbulence, *Journal of Geophysical Research*, 96(A9), 15,985–16,008, doi:10.1029/91JA00565.
- Forme, F., and D. Fontaine (1999), Enhanced ion acoustic fluctuations and ion outflows, *Annales Geophysicae*, 17, 182, doi:10.1007/s00585-999- 0182-6.
- Forme, F., Y. Ogawa, and S. C. Buchert (2001), Naturally enhanced ion acoustic fluctuations seen at different wavelengths, *Journal of Geophysical Research*, 106(A10), 21,503–21,515, doi:10.1029/2000JA900164.
- Forme, F. R. E. (1993), A new interpretation on the origin of enhanced ion-acoustic fluctuations in the upper atmosphere, *Geophysical Research Letters*, 20(21), 2347–2350, doi:10.1029/93GL02490.
- Forme, F. R. E. (1999), Parametric decay of beam-driven Langmuir waves and enhanced ion-acoustic fluctuations in the ionosphere: A weak turbulence approach, *Annales Geophysicae*, 17, 1172–1181.
- Foster, J. C., C. del Pozo, K. Groves, and J.-P. Saint Maurice (1988), Radar observations of the onset of current driven instabilities in the topside ionosphere, *Geophysical Research Letters*, 15(2), 160–163, doi:10.1029/GL015i002p00160.

Foster, J. C., and P. J. Erickson, Simultaneous observations of E-region coherent backscatter and electric field amplitude at F-region heights with the Millstone Hill ULF radar, *Geophysical Research Letters*, 27, 3177–3180, 2000.

Gillespie, D. T., Exact numerical simulation of the Ornstein-Uhlenbeck process and its integral, *Physical Review E*, 54, 2084 (1996a).

Gillespie, D. T., The multivariate Langevin and Fokker–Planck equations, *American Journal of Physics*, 64, 225 (1996b).

Goldman, M. V. (1984), Strong turbulence of plasma waves, *Reviews of Modern Physics*, 56, 709–735.

Graham, D. B., and I. H. Cairns (2013), Electrostatic decay of Langmuir/z-mode waves in type III solar radio bursts, *Journal of Geophysical Research. Space Physics*, 118, 3968–3984, doi:10.1002/jgra.50402.

Graham, D. B., I. H. Cairns, D. R. Prabhakar, R. E. Ergun, D. M. Malaspina, S. D. Bale, K. Goetz, and P. J. Kellogg (2012a), Do Langmuir wave packets in the solar wind collapse? *Journal of Geophysical Research*, 117, A09107, doi:10.1029/2012JA018033.

Graham, D. B., I. H. Cairns, D. M. Malaspina, and R. E. Ergun (2012b), Evidence against the oscillating two-stream instability and spatial collapse of Langmuir waves in solar Type III radio bursts, *Astrophysical Journal. Letters*, 753(1), L18, doi:10.1088/2041-8205/753/1/L18.

Gross, E. P., *Phys. Rev.* 82, 232 (1951).

Grydeland, T., C. La Hoz, T. Hagfors, E. M. Blixt, S. Saito, A. Strømme, and A. Brekke, (2003), Interferometric observations of filamentary structures associated with plasma instability in the auroral ionosphere. *Geophysical Research Letters*, 30(6), 1338, doi:10.1029/2002GL016362.

Grydeland, T., E. Blixt, U. Løvhaug, T. Hagfors, C. La Hoz, and T. Trondsen (2004), Interferometric radar observations of filamented structures due to plasma instabilities and their relation to dynamic auroral rays, *Annales Geophysicae*, 22, 1115–1132.

Guio, P., and F. R. E. Forme (2006), Zakharov simulations of Langmuir turbulence: Effects on the ion acoustic waves in incoherent scattering, *Physics of Plasmas*, 13, 122902, doi:10.1063/1.2402145.

Gurnett, D. A., J. E. Maggs, D. L. Gallagher, W. S. Kurth, and F. L. Scarf, Parametric interaction and spatial collapse of beam-driven Langmuir waves in the solar wind. *Journal of Geophysical Research*, 86, 8833, 1981.

Hagfors, T. (1961). Density fluctuations in a plasma in a magnetic field, with applications to the ionosphere. *Journal of Geophysical Research*, 66.

Hagfors, T. (2003). Basic physics of incoherent scatter; EISCAT summer school 2003.

International Association of Geomagnetism and Aeronomy, Working Group V-MOD (2010), International Geomagnetic Reference Field: The eleventh generation, *Geophysical Journal International*, 183, 1216–1230, doi:10.1111/j.1365-246X.2010.04804.x.

Isham, B., C. La Hoz, M. T. Rietveld, T. Hagfors, and T. B. Leyser (1999), Cavitating Langmuir turbulence observed during high-latitude ionospheric wave interaction experiments, *Physical Review Letters*, 83, 2576–2579, doi:10.1103/PhysRevLett.83.2576.

Isham, B., M. T. Rietveld, P. Guio, F. R. E. Forme, T. Grydeland, and E. Mjølhus (2012), Cavitating Langmuir Turbulence in the Terrestrial Aurora, *Physical Review Letters*, 108, 105003, doi:10.1103/PhysRevLett.108.105003.

Jasperse, J. R., Basu, B., Retterer, J. M., Decker, D. T., and Chang, T. (2013), High frequency electrostatic plasma instabilities and turbulence layers in the lower ionosphere, in *Space Plasmas: Coupling Between Small and Medium Scale Processes*, edited by M. Ashour-Abdalla, T. Chang, and P. Dusenbery, American Geophysical Union, Washington, D. C., doi:10.1029/GM086p0077.

Kaufmann, R. L., P. B. Dusenbery, and B. J. Thomas (1978), Stability of the auroral plasma: Parallel and perpendicular propagation of electrostatic waves, *Journal of Geophysical Research*, 83(A12), 5663–5669, doi:10.1029/JA083iA12p05663.

Kelley, M. (1989). *The Earth's Ionosphere: Plasma Physics and Electrodynamics*. Academic Press.

Kellogg, P. J., and S. J. Monson (1979), Radio emissions from the aurora, *Geophysical Research Letters*, 6(4), 297–300, doi:10.1029/GL006i004p00297.

Kellogg, P. J., and S. J. Monson (1984), Further studies of auroral roar, *Radio Science*, 19(2), 551–555, doi:10.1029/RS019i002p00551.

- Kirkwood, S., H. Nilsson, J. Lilensten, and M. Galand (1995), Strongly enhanced incoherent-scatter plasma lines in aurora, *Journal of Geophysical Research*, 100(A11), 21,343–21,355, doi:10.1029/95JA00765.
- Knudsen, D. J., G. Haerendel, S. Buchert, M. C. Kelley, Å. Steen, and U. Brändström (1993), Incoherent scatter radar spectrum distortions from intense auroral turbulence, *Journal of Geophysical Research*, 98(A6), 9459–9471, doi:10.1029/93JA00179.
- Kosch, M. J., et al. (2009), First incoherent scatter radar observations of ionospheric heating on the second electron gyro-harmonic, *Journal of Atmospheric and Solar-Terrestrial Physics*, 71, 1959–1966, doi:10.1016/j.jastp.2009.08.007.
- LaBelle, J., S. G. Shepherd, and M. L. Trimpi (1997), Observations of auroral medium frequency bursts, *Journal of Geophysical Research*, 102(A10), 22,221–22,231, doi:10.1029/97JA01905.
- LaBelle, J., and R. A. Treumann (2002), Auroral radio emissions. 1. Hisses, roars, and bursts, *Space Science Reviews*, 101, 295–440, doi:10.1023/A:1020850022070.
- LaBelle, J., A. T. Weatherwax, M. Tantiwivat, E. Jackson, and J. Linder (2005), Statistical studies of auroral MF burst emissions observed at South Pole Station and at multiple sites in northern Canada, *Journal of Geophysical Research*, 110, A02305, doi:10.1029/2004JA010608.
- LaBelle, J. (2011), An explanation for the fine structure of MF burst emissions, *Geophysical Research Letters*, 38, L03105, doi:10.1029/2010GL046218.
- Landau, L. D., *Journal of Physics. Akademija Nauk S.S.S.R.* **10**, 25 (1946).
- Lehtinen, M. S. (1986), Statistical theory of incoherent scatter radar measurements, Doctoral dissertation, University of Helsinki, EISCAT Technical Note 86/45 Kiruna, Sweden.
- Lehtinen, M. S., and I. Häggström (1987), A new modulation principle for incoherent scatter measurements, *Radio Science*, 22(4), 625–634, doi:10.1029/RS022i004p00625.
- Lehtinen, M. S., and A. Huuskonen (1996), General incoherent scatter analysis and GUIDAP, *Journal of Atmospheric and Solar-Terrestrial Physics*, 58, 435–452, doi:10.1016/0021-9169(95)00047-X.

- Lockwood, M., B. J. I. Bromage, R. B. Horne, J.-P. St-Maurice, D. M. Willis, and S. W. H. Cowley (1987), Non-Maxwellian ion velocity distributions observed using EISCAT, *Geophysical Research Letters*, 14(2), 111–114, doi:10.1029/GL014i002p00111.
- Lynch, K. A., J. Semeter, M. Zettergren, P. Kintner, R. Arnoldy, E. A. MacDonald, E. Klatt, J. LaBelle, and M. Samara (2007), Auroral ion outflow: Low altitude energization, *Annales Geophysicae*, 25, 1959–1965.
- Lysak, R., M. Hudson, and M. Temerin (1980), Ion heating by strong electrostatic ion cyclotron turbulence, *Journal of Geophysical Research*, 85(A2), 678–686, doi:10.1029/JA085iA02p00678.
- Maggs, J. E. (1978), Electrostatic noise generated by the auroral electron beam, *Journal of Geophysical Research*, 83(A7), 3173–3188, doi:10.1029/JA083iA07p03173.
- Matthews, D. L., M. Pongratz, and K. Papadopoulos (1976), Nonlinear production of suprathermal tails in auroral electrons, *Journal of Geophysical Research*, 81(1), 123–129, doi:10.1029/JA081i001p00123.
- McAdams, K. L., R. E. Ergun, and J. LaBelle (2000), Hf chirps: Eigenmode trapping in density depletions, *Geophysical Research Letters*, 27(3), 321.
- McFadden et al. (1986), High frequency waves generated by auroral electrons, *Journal of Geophysical Research*, 9112, 079.
- Michell, R. G., K. A. Lynch, C. J. Heinselman, and H. C. Stenbaek-Nielsen (2008), PFISR nightside observations of naturally enhanced ion acoustic lines, and their relation to boundary auroral features, *Annales Geophysicae*, 26, 3623–3639.
- Michell, R. G., K. A. Lynch, C. J. Heinselman, and H. C. Stenbaek-Nielsen (2009), High time resolution PFISR and optical observations of naturally enhanced ion acoustic lines, *Annales Geophysicae*, 27, 1457–1467.
- Michell, R. G., and M. Samara (2010), High-resolution observations of naturally enhanced ion acoustic lines and accompanying auroral fine structures, *Journal of Geophysical Research*, 115, A03310, doi:10.1029/2009JA014661.
- Michell, R. G., Grydeland, T., and Samara, M.: Characteristics of Poker Flat Incoherent Scatter Radar (PFISR) naturally enhanced ion-acoustic lines (NEIALs) in relation to

auroral forms, *Annales Geophysicae*, 32, 1333-1347, doi:10.5194/angeo-32-1333-2014, 2014.

Mishin, E., and M. Banaszekiewicz (1998), On auroral ion conics and electron beams acceleration, *Geophysical Research Letters*, 25(23), 4309–4312, doi:10.1029/1998GL900165.

Mishin, E. V., and M. Förster (1995), “Alfvénic shocks” and low-altitude auroral acceleration, *Geophysical Research Letters*, 22(13), 1745–1748.

Mishin, E. V., and K. Schlegel (1994), On incoherent-scatter plasma lines in aurora, *Journal of Geophysical Research*, 99(A6), 11391–11399.

Muschietti, L., Electron beam formation and stability, *Solar Physics*, 130, 201–228, 1990.

Newman, D. L. , M. V. Goldman, R. E. Ergun, and M. H. Boehm, Langmuir turbulence in the auroral ionosphere 1. linear theory, *Journal of Geophysical Research*, 99, 6367 (1994a).

Newman, D. L. , M. V. Goldman, and R. E. Ergun, Langmuir turbulence in the auroral ionosphere 2. Nonlinear theory and simulations, *Journal of Geophysical Research*, 99, 6377 (1994b).

Nicholson, D. R., and M. V. Goldman (1978), Cascade and collapse of Langmuir waves in two dimensions, *Physics of Fluids*, 21, 1766, doi:10.1063/1.862093.

Nicholson, D. R., M. V. Goldman, P. Hoyng, and J. C. Weatherall, Nonlinear Langmuir waves during Type-III solar radio bursts, *Astrophysical Journal*, oeo36, 05, 1978.

Nilsson, H., S. Kirkwood, J. Lilensten, and M. Galand (1996), Enhanced incoherent scatter plasma lines, *Annales Geophysicae*, 14, 1462–1472, doi:10.1007/s00585-996-1462-z.

Palmadesso, P. J., T. P. Coffey, S. L. Ossakow, and K. Papadopoulos (1974), Topside ionosphere ion heating due to electrostatic ion cyclotron turbulence, *Geophysical Research Letters*, 1(3), 105–108, doi:10.1029/GL001i003p00105.

Papadopoulos, K., and T. Coffey (1974), Nonthermal features of the auroral plasma due to precipitating electrons, *Journal of Geophysical Research*, 79, 674–677, doi:10.1029/JA079i004p00674.

- Perkins, F. W., E. E. Salpeter, and K. O. Yngvesson, *Physical Review Letters*, 14, 579 (1965).
- Perry, G.W. et al. (submitted 2015), Spatiotemporally resolved electrodynamic properties of a sun-aligned arc over Resolute Bay, *Geophysical Research Letters*.
- Rietveld, M. T., P. N. Collis, and J.-P. St.-Maurice (1991), Naturally enhanced ion acoustic waves in the auroral ionosphere observed with the EISCAT 933-MHz radar, *Journal of Geophysical Research*, 96(A11), 19,291–19,305, doi:10.1029/91JA01188.
- Rietveld, M. T., P. N. Collis, A. P. van Eyken, and U. P. Løvhaug (1996), Coherent echoes during EISCAT UHF common programs, *Journal of Atmospheric and Solar-Terrestrial Physics*, 58, 161–174.
- Robinson, P. A., D. L. Newman, and M. V. Goldman, Three dimensional strong Langmuir turbulence and wave collapse, *Physical Review Letters*, 61, 702, 1988.
- Robinson, P. A., D. L. Newman, Quasiperiodic behavior in beam-driven strong Langmuir turbulence, *Physics of Fluids. B, Plasma Physics*, 1, 2319, 1989.
- Robinson, P. A., and D. L. Newman, Strong plasma turbulence in the Earth's electron foreshock, *Journal of Geophysical Research*, 96, 17733, 1991.
- Robinson, P. A., D. L. Newman, and A. M. Rubenchik (1992), Effects of long-wavelength dissipation on beam-driven Langmuir turbulence, *Physics of Fluids. B, Plasma Physics*, 4, 2509.
- Robinson, P. A. (1997), Nonlinear wave collapse and strong turbulence, *Reviews of Modern Physics*, 69, 507–573.
- Rosenbluth, M. N., and N. Rostoker (1962), Scattering of electromagnetic wave by a nonequilibrium plasma, *Physics of Fluids*, 5, 776-788.
- Rowland, H. L., J. G. Lyon, and K. Papadopoulos, Strong Langmuir Turbulence in One and Two Dimensions, *Physical Review Letters*, 46, 346 (1981).
- Russell, D., D. F. DuBois, and A. R. Harvey (1988), Nucleation in two dimensional Langmuir turbulence, *Physical Review Letters*, 60, 581–584, doi:10.1103/PhysRevLett.60.581.
- Salpeter, E. E., *Physical Review*, 120, 1528 (1960).

- Salpeter, E. E. (1961), Plasma density fluctuations in a magnetic field, *Physical Review* 122, 1663-1674.
- Samara, M., and J. LaBelle (2006), Structured waves near the plasma frequency observed in three auroral rocket flights, *Annales Geophysicae*, 24, 2911–2919, doi:10.5194/angeo-24-2911-2006.
- Schlatter, N. M., N. Ivchenko, T. Sergienko, B. Gustavsson, and B. U. E. Brändström (2013), Enhanced EISCAT UHF backscatter during high-energy auroral electron precipitation, *Annales Geophysicae*, 31, 1681–1687, doi:10.5194/angeo-31-1681-2013.
- Schlatter, N. M., N. Ivchenko, and I. Häggström (2014), On the relation of Langmuir turbulence radar signatures to auroral conditions, *Journal of Geophysical Research. Space Physics*, 119, doi:10.1002/2013JA019457.
- Sedgemore-Schulthess, F., and J.-P. St.-Maurice (2001), Naturally enhanced ion-acoustic spectra and their interpretation, *Surveys in Geophysics*, 22, 55–92, doi:10.1023/A:1010691026863.
- Semeter, J., C. Heinselman, G. G. Sivjee, H. U. Frey, and J. W. Bonnell (2005), Ionospheric response to wave-accelerated electrons at the poleward auroral boundary, *Journal of Geophysical Research*, 110, A11310, doi:10.1029/2005JA011226.
- Semeter, J., and E. M. Blixt (2006), Evidence for Alfvén wave dispersion identified in high-resolution auroral imagery, *Geophysical Research Letters*, 33, L13106, doi:10.1029/2006GL026274.
- Semeter, J., M. Zettergren, M. Diaz, and S. Mende (2008), Wave dispersion and the discrete aurora: New constraints derived from high-speed imagery, *Journal of Geophysical Research*, 113, A12208, doi:10.1029/2008JA013122.
- Sotnikov, V., et al. (1996), Generation of auroral radio waves by a gyrating electron beam, *Eos: Transactions of the American Geophysical Union*, 77(46), F544, Fall Meet. Suppl., Abstract SA31B-11.
- Strømme, A., V. Belyey, T. Grydeland, C. La Hoz, U. P. Løvhaug, and B. Isham (2005), Evidence of naturally occurring wave-wave interactions in the polar ionosphere and its relation to naturally enhanced ion acoustic lines, *Geophysical Research Letters*, 32, L05103, doi:10.1029/2004GL020239.

St-Maurice, J.-P., J. C. Foster, J. M. Holt, and C. del Pozo, First results on the observation of 440-MHz high-latitude coherent echoes from the E region with the Millstone Hill radar, *Journal of Geophysical Research*, 94, 6771-6798, 1989.

St.-Maurice, J.-P., W. Kofman, and D. James (1996), In situ generation of intense parallel electric fields in the lower ionosphere, *Journal of Geophysical Research*, 101(A1), 335–356, doi:10.1029/95JA02586.

Stubbe, P., H. Kohl, and M. T. Rietveld (1992), Langmuir turbulence and ionospheric modification, *Journal of Geophysical Research*, 97(A5), 6285–6297, doi:10.1029/91JA03047.

Sulzer, M. P. (1986), A radar technique for high range resolution incoherent scatter autocorrelation function measurements utilizing the full average power of klystron radars, *Radio Science*, 21(6), 1033–1040, doi:10.1029/RS021i006p01033.

Sulzer, M. P. (1993), A new type of alternating code for incoherent scatter measurements, *Radio Science*, 28(6), 995–1001, doi:10.1029/93RS01918.

Thejappa, G., M. L. Goldstein, R. J. MacDowall, K. Papadopoulos, and R. G. Stone (1999), Evidence for Langmuir envelope solitons in solar type III burst source regions, *Journal of Geophysical Research*, 104(A12), 28,279–28,293, doi:10.1029/1999JA900363.

Thejappa, G., R. J. MacDowall, M. Bergamo, and K. Papadopoulos (2012a), Evidence for the oscillating two stream instability and spatial collapse of Langmuir waves in a solar type III radio burst, *Astrophysical Journal*, 747, L18, doi:10.1088/2041-8205/753/1/L18.

Thejappa, G., R. J. MacDowall, and M. Bergamo (2012b), In situ detection of strong Langmuir turbulence processes in solar type III radio bursts, *Journal of Geophysical Research*, 117, A08111, doi:10.1029/2012JA017695.

Ungstrup, E., D. M. Klumpar, and W. J. Heikkila (1979), Heating of ions to superthermal energies in the topside ionosphere by electrostatic ion cyclotron waves, *Journal of Geophysical Research*, 84(A8), 4289–4296, doi:10.1029/JA084iA08p04289.

Wahlund, J.-E., F. R. E. Forme, H. J. Opgenoorth, M. A. L. Persson, E. V. Mishin, and A. S. Volotkin (1992), Scattering of electromagnetic waves from a plasma: Enhanced ion-acoustic fluctuations due to ion-ion two-stream instabilities, *Geophysical Research Letters*, 19(19), 1919–1922, doi:10.1029/92GL02101.

Weatherwax, A. T., J. LaBelle, and M. L. Trimpi (1994), A new type of auroral radio emission observed at medium frequencies (1350–3700 kHz) using ground-based receivers, *Geophysical Research Letters*, 21(24), 2753–2756, doi:10.1029/94GL02512.

Valladares, C. E., M. C. Kelley, and J. F. Vickrey (1988), Plasma line observations in the auroral oval, *Journal of Geophysical Research*, 93(A3), 1997–2003, doi:10.1029/JA093iA03p01997.

Vedenov, A. A., E. P. Velikhov, and R. Z. Sagdeev, *Nucl. Fusion, Suppl. Pt. 2*, 465 (1962); W. E. Drummond and D. Pines, *Nuclear Fusion, Suppl. Pt. 8*, 1049 (1962).

Zakharov, V. E. (1972), Collapse of Langmuir waves, *Soviet Physics, JETP*, 35(5), 908–914.

Zakharov, V. E., S. L. Musher and A. M. Rubenchik (1985), Hamiltonian approach to the description of non-linear plasma phenomena, *Physics Reports*, 129, 285.

Zettergren, M., J. Semeter, P.-L. Blelly, G. Sivjee, I. Azeem, S. Mende, H. Gleisner, M. Diaz, and O. Witasse (2008), Optical estimation of auroral ion upflow: 2. A case study, *Journal of Geophysical Research*, 113, A07308, doi:10.1029/2008JA013135.

CURRICULUM VITAE

Hassan Akbari

Boston University
Department of Electrical and Computer Engineering
8 Saint Mary's Street
Boston, MA 02215 USA

E-Mail: hakbari@bu.edu
Cell Phone: +1 617 519 5536

Education

Boston University, Boston, MA, USA (Sep. 2009 – May 2015)
Ph.D. Candidate in Electrical Engineering, GPA: 3.88

Tehran University, Tehran, Iran (Sep. 2005 - May 2009)
Bachelor of Science in Electrical and Computer Engineering

Research Experiences

Research Assistant
Space Physics Lab, Boston University, Boston, MA (May 2010 – present)

- **Remote sensing of ionospheric plasma using Incoherent Scatter Radars (ISRs)**
- **Ionospheric micro instabilities and processes**
In particular: (1) Non-Maxwellian distributions, (2) ion acoustic turbulence, and (3) Langmuir turbulence in the auroral ionosphere.
- **Plasma Simulations**
Zakharov Simulations of electron beam generated Langmuir turbulence.

Intern
Iran's Telecommunication Research Center (Summer 2009)

- Statistical study and simulation of electromagnetic wave propagation and scattering in complex urban areas.

Other Experiences

- Member of the founding group of the SINA Organization (www.SINAIran.org).
- Board member of the Iranian Student Organization at Boston University.

Honors & Awards

- National Science Foundation, \$2500 Student Award, February 2013.
- Top 0.05% of the Iran's Nationwide Matriculation Exam, **Ranked 226th among nearly 500,000 participants**, summer 2005.
- **Member of the National Organization for Development of Exceptional Talents (NODET)** in Iran, September 1999 - May 2006.

Publications

- Akbari, H., J. L. Semeter, M. A. Hirsch, P. Guio, and M. J. Nicolls (2015), Evidence for generation of unstable suprathermal electron population in the auroral F region, *Geophys. Res. Lett.*, 42, 185–192, doi:10.1002/2014GL062598.
- Akbari, H., and J. L. Semeter (2014), Aspect angle dependence of naturally enhanced ion acoustic lines, *J. Geophys. Res. Space Physics*, 119, 5909–5917, doi:10.1002/2014JA019835.
- Akbari et al., (2013), Localization of auroral Langmuir turbulence in thin layers, *J. Geophys. Res. Space Physics*, 118, doi:10.1002/jgra.50314.
- Akbari et al., (2012), Anomalous ISR echoes preceding auroral breakup: evidence for strong Langmuir turbulence, *Geophys. Res. Lett.*, 39, L03102, doi:10.1029/2011GL050288.

Submitted and Under Preparation Publications

- Akbari et al., (2015), Ionospheric electron beams and Langmuir turbulence.
- Goenka et al., (2015), Liquid crystal hyperspectral imager for simultaneous multispectral imaging in agronomy.
- Hirsch et al., (2015), Reconstruction of fine scale dynamics in the aurora.
- Akbari et al., Advances in incoherent scatter plasma lines: observations and applications.

Conference Talks and Posters

- Akbari, H. and J. L. Semeter, P. Guio, Ionospheric beam-plasma interactions: production of quasi-mode in the ion density, AGU Fall Meeting, San Francisco, CA, December 2013.

- Akbari, H. and J. L. Semeter, Ionospheric thin layer of non-linear interactions, joint CEDAR-GEM workshop, Boulder, CO, June 2013.
- Akbari, H. and J. L. Semeter, ISR observations of auroral Langmuir turbulence, URSI national radio science meeting, Boulder, CO, January 2013.
- Akbari, H. and J. L. Semeter, Naturally occurring strong Langmuir turbulence and auroral electromagnetic emissions in the ionosphere, annual summer CEDAR workshop, Santa Fe, NM, June 2012.
- Akbari, H. and J. L. Semeter, Non-thermal ISR scatters from the aurora, joint CEDAR-GEM workshop, Santa Fe, NM, June 2011.

Invited Talks

- Electron beams and Langmuir turbulence in high-latitude ionosphere, USNC-URSI National Radio Science Meeting, Boulder, CO, January 2014.
- Ionospheric beam-plasma interactions, Plasma Seminar at the Dartmouth College, Physics Department, October 2013.

Journals Refereed

- Have refereed 5 journals for Geophysical Research Letters; Journal of Geophysical Research-Space Physics; Radio Science; and Annales Geophysicae, since July 2012.

Professional Memberships

American Geophysical Union (AGU), IEEE

Teaching Experiences

- Graduate Teaching Fellow, Signals and Systems, Boston University, spring 2010.
- Graduate Teaching Fellow, Communication Systems, Boston University, fall 2009.
- Teaching Assistant, Electric Circuits II, Tehran University, fall 2008.
- Teaching Assistant, Electrical Measurement, Tehran University, spring 2008.

